DESIGN, CONSTRUCTION AND VALIDATION OF INTERNAL ORGAN PHANTOMS FOR BIOMECHANICAL TESTING

By

Karim Omri

Thesis submitted in partial fulfillment

of the requirements for the degree of

Master of Applied Science (M.A.Sc) in Natural Resources Engineering

School of Graduate Studies

Laurentian University

Sudbury, Ontario

THESIS DEFENCE COMMITTEE/COMITÉ DE SOUTENANCE DE THÈSE

Laurentian Université/Université Laurentienne
School of Graduate Studies/École des études supérieures

Title of Thesis Titre de la thèse	DESIGN, CONSTRUCTION AND VALIDATION OF INTERNAL ORGAN PHANTOMS FOR BIOMECHANICAL TESTING
Name of Candidate Nom du candidat	Omri, Karim
Degree Diplôme	Master of Applied Science
Department/Program Département/Programme	Natural Resources Engineering
Date of Defence Date de la soutenance	August 12, 2013

APPROVED/APPROUVÉ

Thesis Examiners/Examinateurs de thèse:

Dr. Brahim Chebbi
(Supervisor/Directeur de thèse)

Dr. Ramesh Subramanian
(Committee member/Membre du comité)

Dr. Junfeng Zhang
(Committee member/Membre du comité)

Dr. Ana-Maria Cretu
(External Examiner/Examinatrice externe)

Approved for the School of Graduate Studies
Approuvé pour l'École des études supérieures
Dr. David Lesbarrères
M. David Lesbarrères
Director, School of Graduate Studies
Directeur, École des études supérieures

ACCESSIBILITY CLAUSE AND PERMISSION TO USE

Abstract

This thesis includes the development, construction and testing of internal organ phantoms, with focus on the liver, for biomechanical testing. Phantoms have various biomedical applications such as surgical simulations, minimally invasive surgery, soft tissue characterization, diagnostic tools and instrumentation calibration. However, there is little work present in literature regarding phantoms and the work that is currently available does not account for the non-linear viscoelastic properties as well as the Glisson's capsule. In this work, three different phantoms are presented: a fluid-filled phantom, a perfused phantom and a hydrogel-based liver phantom. A testing apparatus is designed, built and used to measure the force-displacement data during the indentation of the phantom.

The first phantom that is designed and constructed follows the basis of a fluid-filled vessel. It is composed of a linear low-density polyethylene (LLDPE) bag filled with different fluids namely: water, a 1:1 water/glycerine mixture and glycerine. The phantoms are subjected to quasi-static loading as well as relaxation testing. The effect of density and viscosity, its size, and confined and unconfined boundary conditions are characterized.

The second phantom is designed to investigate the effects of hepatic macrocirculation on the biomechanical properties of the liver. The phantom is made of two-part silicone (Smooth-On, ECOFLEX 00-30), and contains a network of conduits to model the large

blood vessels in the liver. A perfusion system that captures the general features of the human hepatic circulation is used to help investigate the effects of the different flow parameters such as pressure and flow rate on the biomechanical characteristics of the liver. The perfusion system is designed to reproduce comparable pressures to the human portal vein and hepatic artery.

The third phantom is made of two parts, a hydrogel inner layer with a LLDPE outer layer. The idea behind this phantom is to represent the organ as accurately as possible by accounting for the capsule that surrounds the organ as well as the biphasic (solid and fluid) nature of the organ. A biphasic poroviscoelastic model is used to model the hydrogel while the LLDPE uses a non-linear hyperelastic and viscoelastic model. Modeling is done in ABAQUS to fit the experimental data obtained from quasi-static indentation and relaxation testing using a parametric study.

In conclusion, phantoms replicating the non-linear viscoelastic properties observed in organs are presented and characterized.

Main Thesis Contributions

- Development and characterization of a simple fluid-filled phantom to represent the mechanical properties of the liver
- Development and characterization of hydrogel-based liver phantom with representation of the biphasic nature of the organ and the Glisson's capsule.

- Development and characterization of perfused liver phantom with ability to be re-created with various vessel configurations.
- Development of testing set-up to characterize various phantoms.

Acknowledgements

First and foremost, I would like to thank my supervisor Dr. Brahim Chebbi for continuous support, motivation and encouragement. I am also grateful for the discussions we have had and the insight and solutions that would always come out of those during the course of this thesis.

I would also like to thank Benjamin Nguyen for finite element analysis (FEA) support and his in-depth discussions. My thanks are also extended to my colleagues Greg Laakanen, Andrew Lapointe, Jeff Pagnutti, Andrew Saikely and Anna Laurie Staszak for their valuable assistance and discussions.

To my parents, Abdel and Jeannine, I am grateful for the continuous support throughout this endeavor. To all my family, friends and colleagues who have supported me through the course of this work I am thankful for everything.

Lastly, to my late friend Cole Howard who has and continues to teach me lessons that could not be learned in any book. He always said, “If you believe in something hard enough and never give up, you’ll eventually get there“. I will never forget you.

Table of Contents

List of Figures

List of Tables

Nomenclature

Alphabetical Symbols

k_R	Bulk moduli normalized relaxation amplitude
J^{el}	Elastic volume ratio
I_1	First deviatoric strain invariant
f	Fluid
p	Fluid pressure
K_0	Initial bulk modulus
K^s	Intrinsic bulk modulus
$\bar{g}$	Magnitude of relaxation spectrum
N	Number of terms
n	Porosity of the medium
k	Relaxation force
g_R	Shear moduli normalized relaxation amplitude
G^S	Shear modulus
s	Solid
U	Strain energy
t	Time
dV	Total volume
dV_v	Volume of voids

Greek Symbols

η	Damper constant
μ	Dynamic viscosity
μ_0	Initial shear modulus

δ	Kronecker delta
λ, μ	Lame constant
ν	Poisson's ratio
τ	Relaxation time constant
ξ	Spring constant
ε	Strain
$\dot{\varepsilon}$	Strain rate
σ	Stress
ϕ	Volume fraction
ε	Weighing factor in section 3.9

Chapter 1 : Introduction

The medical field is in constant evolution, from advancements in surgery simulators [1], minimally invasive surgeries [2], biomedical experimental procedures [3] and medical instruments [4] which allow for unparalleled applications not available years ago. These advancements are due to, thanks in part, to a greater understanding of human physical biomechanical properties.

It is well established that human tissue and organs follow non-linear viscoelastic deformation properties and change from person to person due to several variables such as hydration level, age and daily habits. These changes result in poor repeatability of behavior during biomechanical testing. Studying biomechanical properties of soft tissue and organs is still an active area of research. Some of the aspects that still require investigation are as follows:

- Better understanding of soft tissue properties, especially of internal organs, which received less attention.
- Understanding the changes of the biomechanical properties under certain pathological conditions.
- Developing more accurate and computationally efficient models especially for real time applications such as surgical simulators and trainers. For example, many of the current models used in haptic surgical simulators are based on linear models, which result in simple computation algorithms but less accurate [5].

Experimental testing is still very important in understanding the behavior as well as validating new models and numerical simulations. *In-vivo* cases are always the most accurate for biomechanical testing, however it may not always be feasible due to cost, lack of control and poor repeatability. Phantoms, on the other hand, offer good repeatability, control on boundary conditions, and are cost efficient depending on the application and experimental flexibility. They also eliminate the need for organ preservation and disposal. Table 1-1 provides a good comparison between experimental methods currently available and phantoms.

Table 1-1: Comparison of the testing conditions between *in-vivo, ex-vivo* perfused*, ex-vivo* and phantoms adapted from [6].

Attribute	Experimental Method			
	In-vivo	***Ex-vivo* perfused**	***Ex-vivo***	***Phantom***
Mechanical Behavior	Accurate	Good Enough	Poor	Variable
Accessibility	Difficult	Moderate	Moderate	Easy
Boundary Conditions	Uncontrolled	Moderately Controlled	Moderately Controlled	Controlled
Noise	High	Medium	Medium	Minimal
Ethical Concerns	Live animals	Fewer animals	Fewer animals	No animals
Number of Experiments	Low	Moderate	Moderate	High

Organ phantoms are commonly used to simulate certain properties or behaviors under different conditions such as surgical operation, treatment procedures, collisions,

deformation and pathological conditions. Phantoms are usually tailored and specific to certain applications, and made to exhibit desired properties. Testing of radiation medical procedure requires a phantom having proper radiation properties [7] while a phantom to study ultrasound perfusion measurements must adhere to specific acoustic properties [8]. Consequently, in accordance with these notions, biomechanical testing requires a phantom that will exhibit proper mechanical responses [9]. The goal of this work is the design, construction and testing of various internal organ phantoms. However, the main organ of focus is the liver since there is little work done its biomechanical properties.

1.1.Liver Biological Properties

The liver is the organ responsible for the digestive process, bile synthesis, protein and lipid synthesis as well as detoxification and inactivation of certain substances. It is the largest internal organ in the body, constituting 2.5% of the total weight of an individual. The cardiac output to the liver corresponds to 25% of the total output for the body [10].

The average liver weighs roughly 1.5 kg in healthy adults [11]. While the shape is irregular, the average diameter of the average healthy human is 14.0 ± 1.7 cm. Males have a larger liver diameter (14.5cm ± 1.6 cm) compared to 13.5 ± 1.7 cm for females [12].

1.2.Hepatic Blood Flow

The livers hemodynamic system is composed of macrovessels and microvessels. The hepatic artery has a diameter of 4mm while the portal vein is larger with a diameter of

12mm [13]. The blood enters the liver through the hepatic artery (HA) and by the branching of vessels the portal vein (PV) at the macroscale and will reach the microscale. The interlobular veins are the result of bifurcations of the portal vein and they accompany a branch of the hepatic artery. The sinusoids are reached by the portal venules, which are the result of the bifurcations of the interlobular veins. The hepatic lobules are hexagonally shaped, and they are composed of a centribular vein surrounded by sinusoids. The lobule keeps it shape because of the vascular septa and the portal tracts. The portal tracts are made up of branches of the portal vein, the hepatic artery and a bile duct [14,15]. The sinusoids are capillaries that are only found in the liver which allow for the hepatic activities to be conducted such as exchange of nutrients, oxygen and metabolic activity [16]. The sinusoid space in a patient with fatty liver disease can be reduced by 50% due to an increase in the cell volume [17].

1.3.Motivation

There are several areas where the understanding of the liver's biomechanical properties is not comprehensive. Currently, very expensive phantoms are commercially available on the market for ultrasound training [18,19] as well as for surgery and tissue simulation [19]. Even with those phantoms, none of them are available for the liver. To the author's knowledge, there is no commercially available phantom for the liver, which captures the mechanical and physiological properties. This work will focus on developing phantoms, which will be characterized to replicate the non-linear viscoelastic properties of the organ. Applications would include areas such as soft-tissue characterization, medical and

surgery simulators, diagnostic tools, minimally invasive surgery, equipment calibration and hydrogel tissue scaffolding applications.

1.3.1 Soft-Tissue Characterization

An area of application for phantoms is the characterization of soft tissue because currently a large amount of experiments are needed to obtain the mechanical parameters. As seen in Table 1-1, there are drawbacks to the *in-vivo, ex-vivo* and *ex-vivo* perfused. Initial testing using those methods can serve as a baseline for the development of the phantom, which once developed and validated, can minimize the need for these tests.

1.3.2 Medical and Surgical Simulators

Surgical and medical simulators have evolved rapidly in the last 20 years [20]. A survey response from 139 General Surgery Program Directors believed that virtual reality environments and computer-based surgical simulators would demonstrate benefits if they were incorporated outside the operating room [21]. They can be used by students and new professionals to gain experience and even experienced surgeons as a warm-up technique.

There are over twenty different types of simulators (low and high fidelity) that can reproduce several methods and procedures [22]. Two examples of low fidelity models are bench tests and video box trainers. The bench tests, which are usually static models, do not provide direct feedback but are usually inexpensive and transportable. The video box trainers are widely used in laparoscopy due to the fact they use real surgical instruments

in a box to perform certain operations while having onscreen camera feedback. The video box trainer, while it has limited feedback, uses real instruments that are a benefit to the user [23].

Higher fidelity simulators include virtual reality simulators, procedural simulators and animal models. The virtual reality (VR) simulator is computer-based and allows the user to practice surgical procedures. The user uses interactive haptic instruments where the movements and operation can be tracked on a screen. The statistical analysis, onscreen visual experience and feedback on areas of improvements provide great aid to the user while the main downfall is the cost and lack of accurate tactile feedback [23]. The procedural simulators are a type of VR simulator, which provide the user with the experience of entire procedures. The last high fidelity model is live animals which are very similar to the human body since it is *in-vivo* practice, but like other simulators there are drawbacks which include low availability, high cost as well as moral and ethical concerns [23]. A high accuracy and validated phantom can be introduced as a substitute for *in-vivo* animal practice or be used as a realistic stand-alone simulator.

1.3.2.1. Virtual Reality Simulators

In the virtual reality (VR) simulator, a fully three-dimensional computer-generated environment can be created. In some simulators, a head-mounted display and haptic device are used for the user to immerse his senses into this world. The user can perform surgeries or procedures while seeing them and obtaining feedback on his haptic sensor [24]. VR surgical simulators can be classified into three different generations; the first

generation is anatomy-based, the second generation is physical-based and the third generation is physiology-based [25]. The first generation (anatomy-based) focuses on providing the operator with a virtual anatomical world, which they would be able to navigate through [24]. The physical-based generation finds its focus in the modeling of soft-tissue deformation and interaction. The physiology-based surgical simulators account for interaction between organs such as the development of tumors [26].

The two main components of those simulators are the mechanical deformable model and collision-detection algorithms [27]. The mechanical deformable model is composed of constitutive laws, equations of motion and boundary conditions. The haptic feedback is influenced by the mechanical deformable model that requires accurate characterization of the soft tissue, organ or system being represented. However, there is a trade off that must be made between the deformation accuracy of soft tissue and computation time, which is dependent on the application [25]. Surgery procedure training being the least accurate method needs to be in the 10^{-1}s range to allow the user to have an interactive experience compared to the range surgery planning which would be in the range of 30s to 1h. The increase in computation time is due to the large number of iterations required for surgery planning which requires accounting for many different scenarios over the course of the simulation. Finally, scientific analysis, which is the most accurate but consequentially burdensome simulation, is used to validate physical hypotheses on the properties of soft tissues [25,26].

Phantoms have applications in VR surgical simulator development aside from assisting in the characterization of soft tissue. The computational time of the simulator will be increased in proportion to accuracy of the models. Phantoms can be used to validate new ways to obtain relatively accurate representation and reduce the need of *in-vivo* and *ex-vivo* testing.

1.3.3 Diagnostic Tool

Diagnostic tools have always been used in medicine. A common example would be the thermometer or a stethoscope used to determine the state of the patient. When moving to internal organs such as the liver there are not as many tools currently available. The most common method of determining the state of the organ is through experience and education. There is progress being made in diagnostic using equipment for the articular cartilage [28] and the liver [29] to differentiate between healthy and the faulted case. The main problem to furthering the development of these technologies is that the experiments have to be done *in*-vivo to validate the repeatability of the diagnostic tools since most fault detection is based on statistical parameters. This problem brings forward the application of phantoms, which after the mimicking of the desired mechanical properties can increase the number of tests.

1.3.4 Minimally Invasive Surgery

Laparoscopy or minimally invasive surgery is a technique that it primarily used to perform surgeries on patients. In the past, it was used more a diagnostic method in comparison to its current use in completing whole surgeries. The procedure involves

small incisions in the patient to perform a certain operation or procedure. When a patient is undergoing a laparoscopy it is important for the surgeon to be very careful in order to minimize the damage to the healthy tissue.

There are several advantages with this method of operation, which include shorter recovery time for the patients and smaller scars for the patient. The primary disadvantage for laparoscopic procedures is that, while carrying out the procedure the surgeon performing the procedure only sees what is displayed on the projector. The limitation of laparoscopic procedures results in reduced visual feedback from certain tissues in the body. The surgeon would then be required to use tactile feedback, which is obtained from ample training. There are minimally invasive surgery simulators that will let the surgeon practice [30]. However, the properties of soft tissues and organs are not well reproduced. This issue becomes highly problematic when applying the techniques used during simulation on a patient. Stronger forces than required may be exerted [31]. Phantoms can be used to provide more reliable simulations.

1.3.5 Equipment Calibration and Validation

During the development of new equipment and methods for *in-vivo* testing, the developers will usually use a phantom for calibration and validation [32,33]. It is often seen that phantoms are made from a linear materials and do not encompass the mechanical properties of the organ it is testing [34]. This work provides cost effective testing and calibration protocols, which could replace phantoms that lack accuracy.

1.3.6 Hydrogel Applications

Hydrogels are used widely in the biomedical engineering field since they are similar in terms of mechanical properties and constitutive behavior. Due to this reason they are employed in the phantom, which will be presented in chapter 7. In tissue engineering, the use of hydrogels as scaffolds is often studied [35,36]. There are different methods of preparing these scaffolds called extracellular matrix that is essentially used to organize and grow cells three dimensionally.

1.4.Objective

In order to gain good understanding of the liver mechanical properties it is important to study the individual properties to characterize their effects on the system properly. The objective of this work is to develop various phantoms to obtain better understanding of the liver's mechanical properties. To achieve this objective, we propose to:

I. *To create viable cost-effective soft-tissue phantoms that can be easily be extended to the liver.* In order to create these phantoms a test bench is developed where materials with some known properties are subject to different loading types. Different types of phantoms will be made for different material properties. The phantoms presented must be made using inexpensive materials with easy accessibility. The purpose of this is to create a baseline for extrapolation to the liver's mechanical properties.

II. *To create a perfused phantom of the liver that will be viable for biomechanical testing.* The aim is to develop a liver phantom that will be able to be perfused to then apply some of the perfusion characteristics found in the liver.

III. *To create a liver phantom which will cover the bi-phasic nature of the liver and can be modeled as such.* To that end, we will focus on creating a liver phantom, which will account for both solid and fluid phase that are present in the human organs. For this purpose, the phantom will be characterized and modeled using bi-phasic poroviscoelastic theory.

1.5.Thesis Outline

Chapter 1 provides a brief overview of the liver biological properties, applications and motivation for this work

Chapter 2 describes an in-depth literature review of relevant work applicable to this thesis. This review includes biomechanical phantoms, liver biomechanical experiments and Glisson's capsule experiments.

Chapter 3 describes the theoretical background that is employed in this work such as the basic viscoelastic models, biphasic poroelastic model, biphasic poroviscoelastic model and hyperelastic model.

Chapter 4 provides the experimental apparatus, perfusion system and data acquisition that is used to perform tests on the phantoms. Preliminary studies including the method of and results for the determining mechanical properties LLDPE are also presented in this chapter.

Chapter 5 describes manufacturing of fluid-filled phantoms as well as the results of experiments conducted on them.

Chapter 6 provides the manufacturing techniques and results for a perfused liver phantom.

Chapter 7 describes a hydrogel-based liver phantom with consideration for the Glisson's capsule.

Chapter 8 discusses the conclusions for this work as well as future research recommendations.

Chapter 2 : Literature Review

This chapter provides a literature review of the state of the art for each of the different fields that will be introduced in the thesis. Since this work is multidisciplinary, to meet the objectives outlined it is imperative to have a background on topics that will be covered in the course of the research. The state of the art in research on liver biomechanical experiments, Glisson's capsule experiments, and several types of phantoms as well as hydrogel experiments and characterization will be reviewed.

2.1.Liver Biomechanical Experiments

A study by Nava et al. [3] focused on the characterization of the mechanical properties of the human liver. Tests were performed using an aspiration system during open surgery. A comparison between two different models, QLV and Rubin Bodner (RB), was made. According to this study, RB model yielded better results during repeated loading cycles. It was also shown that a non-linear time dependent constitutive equation finite element simulation for the whole organ is not feasible for the real time requirement. The authors reported that the average linear elastic modulus to be roughly 20 kPa with 8kPa and 48kPa on the higher and lower end, respectively.

A novel testing method using *ex-vivo* perfused porcine liver was done by Kerdok et al. [37]. Four different testing conditions including *in-vivo*, *ex-vivo* perfused, *ex-vivo* post perfused and *in vitro* were performed to quantify the viscoelastic properties due to the effects of perfusion. Two devices were used; a TeMPeST to apply a sinusoidal indentation force with varying frequencies between 0.1Hz and 200Hz, and a creep

indenter capable of measuring up to 50% deformation which was used to characterize the deformation over 300s. It was observed from the empirical model that non-perfused porcine livers exhibited stiffer and more viscous properties in comparison to *in-vivo* measurements. A close approximation to the *in-vivo* case is seen in the *ex-vivo* perfused condition. Therefore, we can conclude that perfusion has an impact on the viscoelastic properties of the liver.

Schwartz et al. [38] developed a linear elastic tensor-mass method for soft tissue to reduce the computation time associated with a non-linear viscoelastic mechanical forces and deformation. Experiments were conducted on a deer liver in order to validate the model for axial loading conditions. The model developed showed that in conjunction with real-time applications there was an effect due to strain rate. Perforation testing using a biopsy needle of the deer liver was also done and compared to the model. The parameters obtained for the model were 2500 Pa for Young's modulus and 600 Pa s for coefficient of viscosity. The model assumed 0.4 for Poisson's ratio since there was no way of obtaining that coefficient from the uniaxial experiment. It was seen that the model was accurate for the axial loading of the needle. However, it was not the case for the perforation testing.

Raghunathan et al. [39] applied a poroviscoelastic model to unconfined liver compression. Stress relaxation experiments were done on seventeen ex-vivo porcine livers. Non-linear least square fitting was applied to the experimental data to obtain the

model liver parameters. These parameters were inputted into finite element analysis software ABAQUS^{TM} where a parametric study was then performed to obtain the remaining parameters.

2.2.Glisson's Capsule Experiments

The Glisson's capsule is a protective tissue layer that surrounds the liver. Organs like the kidney and spleen also have a capsule, and its main roles are to keep the shape of the organ and protect it from impact and trauma. An investigation undertaken by Umale et al. [40] studied the mechanical properties of a porcine liver capsule. The results showed that the elastic modulus in small strain is 8.22 ± 3.42 MPa, and in large strain is 48.15 ± 4.5 MPa. A non-linear hyper-elastic constitutive law was applied and successfully fitted to the data. The authors suggested that the Glisson's capsule mechanical properties could potentially yield simulation of laceration and hematoma.

2.3.Flow Phantoms

A flow phantom was developed by Fredriksson et al. [41] to establish a method of separating into several flow velocity components of the Doppler power spectrum. The phantom was composed of piece of Delrin® surrounded by polythene micro-tubes where transparent silicone filled the gaps between the tubes. On the topside of the phantom a second piece of Delrin® was added with aim to increase the isotropic properties of light prior to its contact with the flow, which was driven by a syringe pump. Blood with a hematocrit of 0.45, which had been heparinized and diluted in physiological saline of 0.9% NaCl and microspheres were also used. Testing of the phantom was done using a

laser Doppler flowmetry system. The velocity component in both fluids was measured in both high and low concentration case. The authors suggested that this method could be extended as a clinical tool to differentiate capillary blood flow after furthering their studies.

Ramnarine et al. [42] developed a wall-less flow phantom, which was optimized to prevent leakage of the blood mimicking fluid using a novel method for ultrasound applications. This wall-less phantom was built using an agar-based tissue mimicking material with a composition of 82.97% water, 11.21% glycerol, 0.46 % benzalkoniumchloride, 0.53% 400 grain SiC powder, 0.94% 3μm Al_2O_3 powder and 3% Struers agar. This mixture was poured into a mold for the different stenosis cases from 0% to 75% diameter reduction. The inlets and outlets of the stenosis replicas were attached to tubes to complete the closed-loop operation of the phantom. Blood-mimicking fluid was pumped through the phantom using a gear pump to produce steady and pulsatile flows with a maximum rate of 2.8 liters/min. The study revealed over the course of 4 days of continuous use, no leaks or tear were found in the phantoms or stenosis replicas.

In the work done by Debbaut et al. [16], the hepatic microcirculation was obtained using physical model of the vascular tree. A vascular corrosion casting was done using a fluid injected into the hepatic artery and portal vein of the human livers. The fluid contained 100 parts of Batson's #17 monomer solution, 15 parts of Batson's catalyst, 1 part of Batson's promoter and 20 parts of monomeric methyl methacrylate. It was ensured that

the fluid covered all the microvessels by seeing the polymer appear from the hepatic vein. The liver was then introduced to potassium hydroxide to yield the vascular replica. This casting method inspired the phantom manufacturing techniques explained in Chapter 6. A high-resolution micro-CT scan of a small volume of the sample from the liver casting was used to obtain three-dimensional geometry. The CFD simulation of the flow of the reconstructed sinusoid used those results. It was found that the permeability coefficient in the parallel flow direction to the central hepatic vein is twice the one coefficient in the radial and circumferential directions. Another conclusion is that the flow simulation parallel to the central vein is smaller than the radial and circumferential directions.

2.4.Fluid-Filled Phantoms

Gosline et al. [43] worked on developing a novel technique for modeling fluid-filled structures enclosed by a linear elastic media. To obtain real-time haptic rendering, a finite element simulation was used. Several human tissues can be considered fluid-filled objects such as glands and cysts. The fluid in the model was modeled using hydrostatic pressure. A proportional feedback system was developed to numerically investigate the pressure change in the elastic system. The relationship between the volume and pressure of the fluid-filled object must be maintained since the fluid is treated as incompressible. In order to validate the model, the authors created an elastic tissue phantom filled with an incompressible fluid pocket. The results measured with ultrasound imaging and surface markers showed good agreement for values of strain up to 15%. This is likely due to the limitations of linear finite element methods.

The work done by De & Srinivasan [44] dealt with developing a novel method of soft tissues modeling for applications to surgical simulations. The model was made using 3D fluid-filled thin-walled structures. It was seen to be computationally efficient and also to a certain degree accurately model the non-linear force-displacement response in comparison to *in-vivo* data on soft tissues. The authors argued this model has the ability to be extended to viscoelastic and inhomogeneous materials and 3D geometry so long as computational time did not increase drastically.

2.5.Biomechanical Phantoms

In this section, soft tissue phantoms and liver phantoms will be reviewed. It should be mentioned that there is a lot of similarities between the mechanical properties of the liver and other internal organs.

2.5.1 Soft Tissue Phantom

Turgay et al. [45] developed a new elastography method, which images the soft tissues mechanical properties. Vibrations of different frequencies were applied to a tissue and the displacements were measured using ultrasound imaging. This procedure was performed on a phantoms composed of different types of hydrogels such as agar, and gelatin and combination of both with different compositions while keeping the size the same. Two homogenous phantoms were made with values of 16kPa and 25kPa for Young's modulus. The third phantom was composed of three layers. The outer layers were made

of gelatin while the middle layer was made of agar, cellulose and glycerol, which was harder in comparison. It was concluded that the phantom study validated the procedure.

A study done by Boonvisut et al. [34] developed a method to estimate the soft tissue mechanical properties while being robotically manipulated. Phantoms made of Ecoflex 00:30 and silicone thinner were constructed. Different ratios of the two-part silicone (Part A and Part B) and the thinner were used and compared. Young's modulus and Poisson's ratio were determined to be 27.04kPa and 0.4287, respectively, in the 1:1:0 ratio (Part A: Part B: Thinner) phantom. In the case of the 1:1:2 phantom, the Young's modulus was 6.493 kPa and the Poisson's ratio was 0.42359. The phantoms were subjected to different manipulation parameters such as "tangent pull", "in-plane pull", "tangent pull", "side pull" and "twist and pull" while having the gripper attached to the phantom and the data was acquired using force feedback as well as a steer camera. Inverse finite element analysis was then used to determine the material parameters. They used a neo-Hookean hyperelastic model to get the material properties from different deformation conditions. It was reported in this work that in some cases the neo-Hookean models did not fit the experimental data very well when dealing with highly nonlinear materials. A quasi-static behavior was assumed in the simulation because the inertial and viscous effects were negligible.

Han et al. [32] presented a novel indentation system to obtain biomechanical properties of soft tissue in the *in-vivo* case. This system was tested using different phantoms. A single-

layer phantom was used to validate the linear elastic properties. The phantom were made using gelatin (G-2500, Sigma-Aldrich Co., LTD., Dorset England). The gelatin was hydrated with deionized water and then heated. It was then poured into a mold, immersed in an ice-water bath and allowed to set. To increase the scattering and adsorption properties, talcum powder was added to these phantoms. Different single layer phantoms were made and each had different geometries and gelatin concentration. Two phantoms with a rectangular geometry (width: 120mm, length: 190mm, height: 42mm) and gelatin concentration of 5% and 10% were made. Another two phantoms of a cylindrical geometry (diameter: 95mm, height: 50mm) with 5% and 10% gelatin were also constructed. Another phantom was made of three-layer phantom (width: 120mm, length: 190mm, height: 33.5mm) made of 6%, 4% and 2% gelatin to model the non-homogeneity of soft tissue.

2.5.2 Liver Phantoms

A phantom made from polyvinyl alcohol hydrogel and water was manufactured and studied by Jiang et al. [46] with aim to study the soft tissue deformation during minimally invasive surgery with needle intervention. The phantoms were made with 3g PVA, 17g de-ionized water, 80g dimethyl-sulfoxide. They were subjected to freeze-thaw cycles going from room temperature to -20^{o}C and back to room temperature per cycle. The authors attempted to establish a relationship between the numbers of freeze-thaw cycles applied to the phantoms to *ex-vivo* porcine liver tissue under uniaxial tension testing. Needle insertion testing was also done to the phantom. The freeze-thaw cycles had an impact on the stress-strain relationship and morphological properties of the gel. It was

concluded that with the variation of those cycles it was possible to achieve similar mechanical and morphological properties to the porcine liver.

A truth cube was developed Kerdok et al. [47] to obtain a physical stand for validation of real-time soft tissue deformation. This cube was made of silicone rubber with embedded Teflon® spheres. The truth cube was subjected to uniaxial compression as well as spherical indentation testing. CT scan images of the rubber were taken for those tests. A finite element model was developed for the same experimental situations and compared to the testing results. The main goal of this work was to provide a model validation and a physical standard for soft tissue deformation model validation.

Liu et al. [33] developed a force-sensitive wheeled probe in order to obtain a mechanical image by rolling on the surface of an object. This was used for identification of the internal components and the determination of the mechanical properties of the soft tissue. Experiments were both conducted on a phantom and *ex-vivo* on a porcine liver. The phantom was made of RTV 6166 (General Electric) and contained six different shaped (rectangular and triangular) nodules were made in it. The results obtained from the phantom showed that the square nodules would hide the response of the triangular nodules. It was also concluded that the rolling mechanical image would yield location and a rough estimate of the shape and size of the nodule within the phantom.

2.6.Hydrogel Experiment and Characterization

Kalyanam et al. [48] compared different loading conditions of phantoms such as confined and unconfined compression. Three different hydrogels were made with different water concentration of 92%, 94% and 96% using 250 bloom-strength, Type-B gelatin. A biphasic poroviscoelastic model was applied to the data obtained from the experiments. The modeling was done using FEA with ABAQUS and a parametric study was conducted to obtain the permeability, the Young's modulus and the Poisson's ratio.

A study done by Toohey et al [49] studied the quasi-static indentation and relaxation spectrum of hydrogels. Water concentrations of 92%, 94% and 96% were used in this study. A parametric study was conducted to fit the biphasic poroviscoelastic to the obtained experimental data.

Kwon & Subhash [36] observed the effect of strain rate of 250 bloom ballistic gelatin. The hydrogel geometry was cylindrical with a diameter of 14mm for both quasi-static (height: 14mm) and dynamic testing (height: 2mm). Quasi-static testing was performed on different hydrogel samples at rates of $1.3 \times 10^{-3}\ s^{-1}$, $5.3 \times 10^{-3}\ s^{-1}$ and $10.7 \times 10^{-3}\ s^{-1}$. The authors described that the hydrogels under quasi-static indentation had similar stress-strain curves for varying strain rates. In terms of dynamic testing, higher loading rates were also tested and it was found that the compressive strength increased from 3kPa at a strain rate of $\sim 0.0013\ s^{-1}$ to 6 mPa at $\sim 3200\ s^{-1}$.

Chapter 3 : Theoretical Background

This chapter covers the theory required to analyze the data obtained during phantom testing. Viscoelastic materials exhibit both viscous and elastic properties. Soft tissues are considered viscoelastic due to their biphasic nature [39]. The basic viscoelastic models, namely Maxwell, Kelvin-Voigt and Standard Linear Solid (Zener) model that are used to estimate approximately the behavior of viscoelastic materials are introduced. Further models are presented such as the quasilinear viscoelastic model , the biphasic poroelastic model and the biphasic poroviscoelastic model to understand the complex behavior of soft tissues and organs. Hyperelastic theory will also be covered due to its ability to fit non-linear models. Finally, the theory of water and glycerine mixtures is introduced since these mixtures are used in the phantoms developed in Chapter 5.

3.1.Viscoelasticity

Viscoelasticity is a property attributed to materials, which display both viscous and elastic properties. There are three main features to viscoelasticity: creep, hysteresis and relaxation. Creep is observed when a material is subjected to a certain stress, which is held constant. The material will then keep deforming over time. Hysteresis is displayed during quasi-static loading and unloading of a material. Both curves will be slightly different.

3.1.1 Relaxation Spectrum

The relaxation spectrum is observed when a material is subjected to a strain, which is held constant over a period of time. With passage of time, the stresses in the material will become smaller as described by Equation 1.

$$k(t) = \sum_{n=0}^{N} \alpha_n e^{-t\upsilon_n} \quad (1)$$

where k(t) is the relaxation force, α_n is the amplitude, t is time and υ_n is the characteristic frequency.

3.2.Maxwell Model

The Maxwell model is made up of a spring and damper in series as seen in Figure 3.1. The stress-strain relationship for the spring component and the damper are described Equations 2 and 3, respectively.

$$\sigma_1 = \xi \cdot \varepsilon_1 \quad (2)$$

$$\sigma_2 = \eta \cdot \dot{\varepsilon}_2 \quad (3)$$

where σ_1 is the stress in the spring, $\varepsilon_1$is the strain in the spring, σ_2 is the stress in the damper, $\dot{\varepsilon}_2$ is the strain rate for the damper, η is the damper constant and ξ is the spring constant.

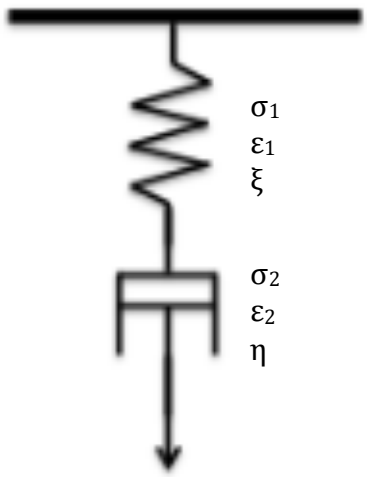

Figure 3.1: Maxwell Model Diagram: Spring and Damper in Series

Free body diagram analysis yields that the stress in the spring and damper are equal assuming a constant area. Also, by noting that the total strain is the sum of the strain in the spring and the strain in the damper and by combining Equations 2 and 3, it is possible to obtain Equation 4, which is the governing equation for the Maxwell model.

$$\varepsilon = \frac{1}{\xi} \cdot \dot{\sigma} + \frac{1}{\eta} \cdot \sigma \tag{4}$$

Applying a constant stress will induce creep, and the creep modulus as a function of time can be seen in Equation 5.

$$E(t) = \frac{\sigma_0}{\varepsilon(t)} = \frac{\xi\eta}{\eta + \xi t} \tag{5}$$

The drawback from the Maxwell model is that it does not capture creep data very well.

3.3.Kelvin-Voigt Model

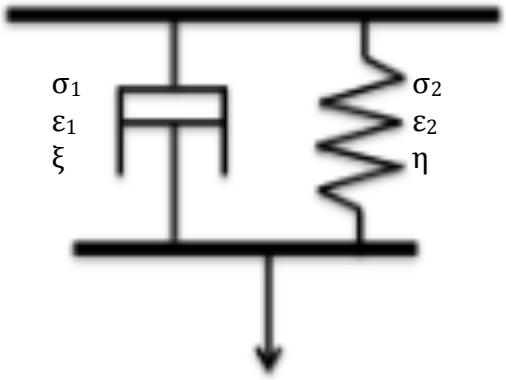

Figure 3.2: Kelvin Model Diagram: Spring and Damper in Parallel

The Kelvin-Voigt model is made of a damper and spring in parallel as seen in Figure 3.2. The stress-strain relations are the same as the Maxwell model. However, the total stress is the sum of the stress in the spring and the stress in the damper. Equation 6 is the governing equation in the Kelvin-Voigt model.

$$\sigma = \eta \cdot \dot{\varepsilon} + \xi \cdot \varepsilon \tag{6}$$

The creep modulus, E (t), is described by Equation 7. This relation is obtained while holding the stress constant and solving for the total strain.

$$E(t) = \frac{\sigma_0}{\varepsilon(t)} = \xi \left[1 - e^{-\frac{t}{T_R}}\right]^{-1} \tag{7}$$

Analysis and comparison to experimental data shows the Kelvin-Voigt model yields a valid approximation for the creep, but does not perform well in predicting relaxation.

3.4.Zener or Standard Linear Solid Model

The Zener model consists of elements in series and parallel as seen in Figure 3.3. The stress-strain relations are expressed by Equations 8, 9 and 10.

$$\sigma_1 = \xi_1 \cdot \varepsilon_1 \tag{8}$$

$$\sigma_2 = \xi_2 \cdot \varepsilon_2 \tag{9}$$

$$\sigma_3 = \eta_3 \cdot \dot{\varepsilon}_3 \tag{10}$$

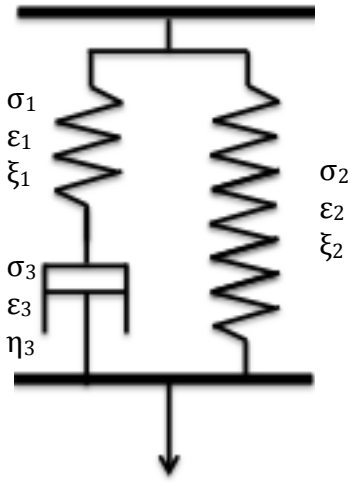

Figure 3.3: Standard Linear Solid Model Diagram

The governing equation of this model is given by Equation 11.

$$\dot{\varepsilon} = \frac{\dot{\sigma} - \xi_2 \dot{\varepsilon}}{\xi_1} + \frac{\sigma - \xi_2 \varepsilon}{\eta_3} \tag{11}$$

When applying constant stress the strain rate for creep, the relation can be seen in Equation 12.

$$\varepsilon(t) = \frac{\sigma_o}{\xi_2} - \frac{\sigma_o \xi_1}{\xi_2(\xi_1 + \xi_2)} e^{\frac{-\xi_1 \xi_2 t}{\eta_3(\xi_1 \xi_2)}} \tag{12}$$

3.5.Quasilinear Viscoelastic Model (QLV)

The QLV is one of the most well-known and used models in terms of soft tissue characterization. It captures the time-dependent viscoelastic behavior of the material over large deformation. The governing equation for the QLV is given by Equation 13.

$$T(t) = \int_{-\infty}^{t} G(t - \tau) \dot{T}^{(e)}(\tau) d\tau \tag{13}$$

where $G(t)$ represents the reduced relaxation function, $\dot{T}^{(e)}(\tau)$ is the rate of change of the elastic response over time. Equation 14 is obtained from Equation 13 to introduce the reduced creep function, J(t).

$$T^{(e)}[\lambda(t)] = \int_{-\infty}^{t} J(t - \tau) \dot{T}(\tau) d\tau \tag{14}$$

3.6.Biphasic Poroelastic model

The biphasic poroelastic (BPE) model has been used for the modeling of cartilage and hydrogels [50]. When dealing with cartilage, the model will be influenced mostly by the hydraulic permeability and the modulus of elasticity of the solid matrix [51].

The governing properties of the biphasic poroelastic model are pore pressure and void ratio. It can be seen that each of these parameters will vary with time and position. Superscripts *s* and *f* represent the phase, either solid or fluid. Equation 15 represents the porosity of the medium as a function of the ratio of the volume of voids and the total volume.

$$n(x,t) = \frac{dV_v(x,t)}{dV(x,t)} = \frac{\phi^f(x,t)}{\phi^f(x,t)+\phi^s(x,t)} = \phi^f(x,t) \tag{15}$$

where *n(x,t)* is the porosity of the medium, $dV_v(x,t)$ is the volume of voids, $dV(x,t)$ is the total volume and ϕ^α is the volume fraction of phase α which can be either solid($\alpha = s$) or fluid ($\alpha = f$). It can be seen that the sum of the volume fractions for solid and liquid is equal to 1. This assumes that fluid completely fills the voids in the medium.

The stress of the medium is a function of the stresses of the fluid phase and that of the solid matrix as shown in Equation 16.

$$\sigma_{ij}(x,t) = \sigma_{ij}^s(x,t) + \sigma_{ij}^f(x,t) = \tilde{\sigma}_{ij}^s(x,t) - p(x,t)\delta_{ij} \tag{16}$$

where $\sigma_{ij}(x,t)$ is the total stress, $\sigma_{ij}^{s}(x,t)$ is the stress in the solid matrix, $\sigma_{ij}^{f}(x,t)$ is the stress in the fluid phase, $\tilde{\sigma}_{ij}^{s}(x,t)$ is the effective solid stress, δ_{ij} is the Kronecker delta and $p(x,t)$ is the fluid pressure.

The effective solid stress can be expressed, in Equation 17, as a function of the total solid stress and the fluid pressure.

$$\sigma_{ij}^{s}(x,t) = \tilde{\sigma}_{ij}^{s}(x,t) - \phi^{s}(x,t)p(x,t)\delta_{ij} \tag{17}$$

Equation 18 shows that the stress in the fluid phase is a function of the volume fraction of the fluid phase and the fluid pressure.

$$\sigma_{ij}^{f}(x,t) = -\phi^{f}(x,t)p(x,t)\delta_{ij} \tag{18}$$

The effective solid stress is obtained after applying λ^{s} and μ^{s}, which are Lame's constants of the solid matrix.

$$\tilde{\sigma}_{ij}^{s}(x,t) = \lambda^{s} tr(\epsilon_{ij}^{s}(x,t))\delta_{ij} + 2\mu^{s}\epsilon_{ij}^{s}(x,t) \tag{19}$$

where $\epsilon_{ij}^{s}(x,t)$ is the strain tensor of the solid matrix and $tr(\epsilon_{ij}^{s}(x,t))$ is the trace of the strain tensor of the solid matrix [48,52,53].

3.7.Biphasic Poroviscoelastic Model

The biphasic poroviscoelastic model follows the same basic principles as the biphasic poroelastic model but solid matrix's intrinsic flow-independent viscoelastic characteristic is taken into consideration. The relation is given by Equation 20.

$$\tilde{\sigma}_{ij}^{s}(x,t) = K^{s}\int_{-\infty}^{t} dt' k_R(t-t')\frac{\partial\, tr\left(\epsilon_{ij}^{s}\right)}{\partial t'}(x,t') + 2G^{S}\int_{-\infty}^{t} dt' g_R(t-t')\frac{\partial\left(\epsilon_{ij}'^{s}\right)}{\partial t'}(x,t') \quad (20)$$

where K^{s} represent the intrinsic bulk modulus, G^{S} is the shear modulus, $k_R(t)$ is the bulk moduli normalized relaxation amplitude, $g_R(t)$ is the shear moduli normalized relaxation amplitude and $\epsilon_{ij}'^{s}$ is the deviatoric strain tensor of the solid matrix. The intrinsic bulk modulus, the shear modulus and the deviatoric stress tensor are described by Equations 21, 22 and 23, respectively.

$$K^{s} = (3\lambda^{s} + 2\mu^{s})/3 \quad (21)$$

$$G^{s} = \mu^{s} \quad (22)$$

$$\epsilon_{ij}'^{s} = \epsilon_{ij}^{s}(x,t) - \frac{1}{3}tr(\epsilon_{ij}^{s}(x,t)) \quad (23)$$

Equation 24 shows a discrete solution introduced by Suh and Bai [54] to the relaxation spectrum, which was introduced in the previous section.

$$g_R(t) = 1 + \bar{g} \sum_{i=1}^{N} e^{-t/\tau_i} \tag{24}$$

where $\bar{g}$ is the magnitude of the spectrum, N is the number of terms in the series and τ_i is the relaxation time constant [48].

Due to difficulty in obtaining the flow-independent relaxation of the hydrostatic component, different models presented by Suh and DiSilvestro [52] are available to account for this. The first model consists of having a constant bulk modulus, $k_R(t)$, of 1 and the relaxing shear modulus being determined by viscoelastic law. The second model consists of assuming that the bulk modulus and shear modulus have equal values, i.e., $k_R(t) = g_R(t)$.

3.8.Hyperelastic Models

An ideally elastic material where the stress-strain energy comes from a strain energy density function is known as a hyperelastic material. It is used when linear models are not suitable to correctly model the behavior of a material. Non-linearity in stress-strain relationships can be expressed using this model. There are several different categories of hyperelastic materials, namely, phenomenological, mechanistic and combinations of the two.

3.8.1 Neo-Hookean Model

There are several different kinds of hyperelastic models to describe the behavior of rubbers, polymers and soft tissues when subjected to high strains. One of the simpler models is the Neo-Hookean model. The strain energy potential for this model is given by Equation 25.

$$U = C_{10}(\overline{I_1} - 3) + \frac{1}{D_1}(J^{el} - 1)^2 \tag{25}$$

where U is the strain energy, C_{10} and D_1 are related to the initial shear modulus Equation 26 and 27, respectively, J^{el} is the elastic volume ratio and $\overline{I_1}$ is the first deviatoric strain invariant given by Equation 28.

$$\mu_0 = 2C_{10} \tag{26}$$

$$K_0 = \frac{2}{D_1} = \frac{3(1-2\nu)}{\mu_0(1+\nu)} \tag{27}$$

$$\overline{I_1} = \bar{\lambda}_1^2 + \bar{\lambda}_2^2 + \bar{\lambda}_3^2 \tag{28}$$

where μ_0 is the initial shear modulus, K_0 is the initial bulk modulus and ν is the Poisson ratio.

3.9.Water-Glycerine Mixture Theory

The water-glycerine mixture theory is taken from the work done by Cheng [55]. They adapted their relations from other work in literature and removed the need for tables (linear interpolation), which allows for more accurate results since linear interpolation is

no longer necessary. Equation 29 gives the dynamic viscosity of a glycerol and water mixture.

$$\mu = \mu_w^{\alpha} \mu_g^{1-\alpha} \tag{29}$$

where μ denotes the dynamic viscosity, subscripts *w* and *g* represent water and glycerine, respectively, and α is the weighting factor or concentration.

The dynamic viscosity of water is known to have an inverse proportional relation with the temperature. Equation 30 describes this relation:

$$\mu_w = \mu_{w100}^{\varepsilon} \mu_{w0}^{1-\varepsilon} \tag{30}$$

where μ_{w100} and μ_{w0} are the dynamic viscosity at 100°C and 0°C, respectively, and ε is the weighting factor given by Equation 31.

$$\varepsilon = \frac{\ln\left(\frac{\mu_w}{\mu_{w0}}\right)}{\ln\left(\frac{\mu_{w100}}{\mu_{w0}}\right)} \tag{31}$$

By substitution of the values of μ_{w100} and μ_{w0} and with a few manipulations to Equations 30 and 31, it is possible to express the dynamic viscosity of water as shown in Equation 32.

$$\mu_w = 1.790 \exp\left(\frac{(-1230-T)T}{36100+360T}\right) \tag{32}$$

where the units of μ_w are expressed in cP and the range of T is 0-100^{o}C.

The dynamic viscosity of glycerol is obtained in a similar fashion:

$$\mu_g = 12100 \exp\left(\frac{(-1233+T)T}{9900+70T}\right) \tag{33}$$

Chapter 4 : Experimental Apparatus, Perfusion System, Data Acquisition and Preliminary Studies

This chapter outlines the experimental apparatus and data acquisition system employed for quasi-static indentation and relaxation experiments described in subsequent chapters. The preliminary studies presented in this chapter will cover a parametric study to obtain the material properties of linear low-density polyethylene (LLDPE).

4.1.Experimental Apparatus

The experimental apparatus designed and built for force-displacement testing is presented in Figure 4.1. This system consists of a load cell (Interface, MBP-50) attached to a linear stage (Zaber Technologies, T-LSR) mounted vertically. On the end of the load cell a mounting system is used for holding different indenters. Two indenter are available: the first one is a blunt 9mm in diameter while the other is a spherical 2mm in diameter to simulate a point load. Software to control the depth and velocity of the linear stage was written in NI Labview.

4.1.1 Load Cell Calibration

The load cell employed in the system was calibrated using known masses. The sensor provides a linear trend within the operation range (0-10N). Calibration value of 5.745 (N/Volt) was determined and applied to the measured signal.

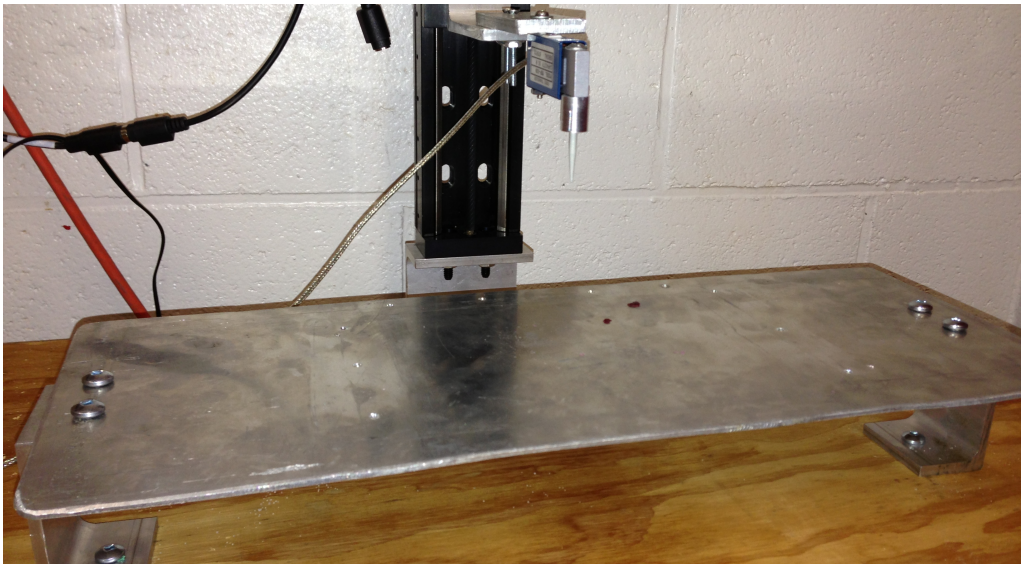

Figure 4.1: Experimental apparatus used for indentation of the phantoms

4.2.Perfusion System

A closed loop flow system was designed, built and used to perfuse the liver phantom described in Chapter 6, which tends to reproduce the general features of the human hepatic macrocirculation. This system, shown in Figure 4.2, is similar to the one used by Kerdok [37] to perfuse *ex-vivo* porcine livers. In this design, each of the inlets is pressurized to the average pressure in the human liver. This is accomplished by using two containers at different heights with respect to the phantom. The fluid is collected and pumped back to the containers after having passed through the phantom. A 12-Volt DC centrifugal pump with a flow rate up to 2 liters/minute is driven by a mini DC motor *SGMADA RF 370C 12560*. A *Roboteq SDC2150* controller operates the motor to simulate the blood circulation. Two different modes are possible with this system: non-

pulsatile (mono-phasic) and pulsatile (bi-phasic). The pulsatile mode is accomplished by controlling the rate at which the motor is turned on and off.

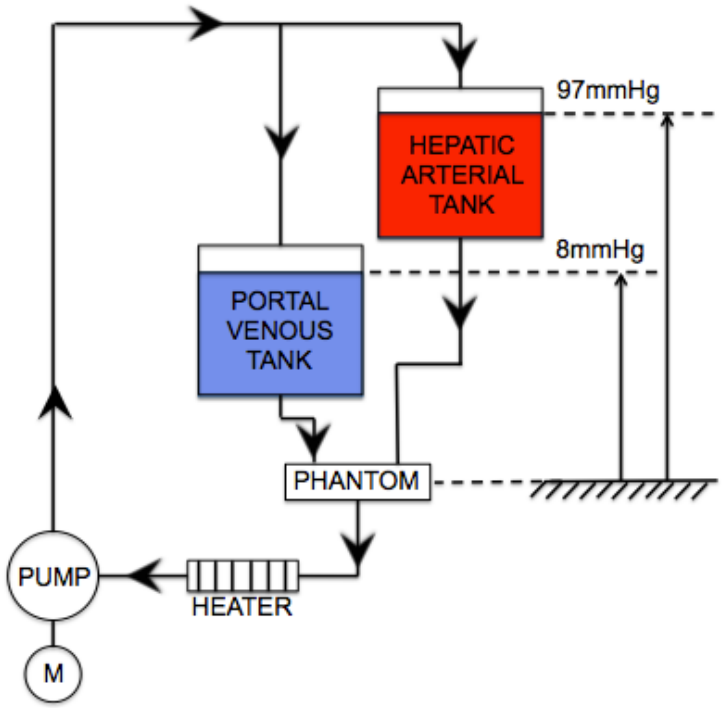

Figure 4.2: Perfusion system diagram

4.3.Data Acquisition

An Omega-DAQ Board-3000 is used for data acquisition and programmed using NI Labview. The signal from the load cell is amplified using a strain gauge amplifier. A Graphic User Interface was developed and used for each of the experiments (Figure 4.3). It includes all the required controls such as perfusion rate, indentation depth and speed to name a few. An in-depth explanation of each component is presented below.

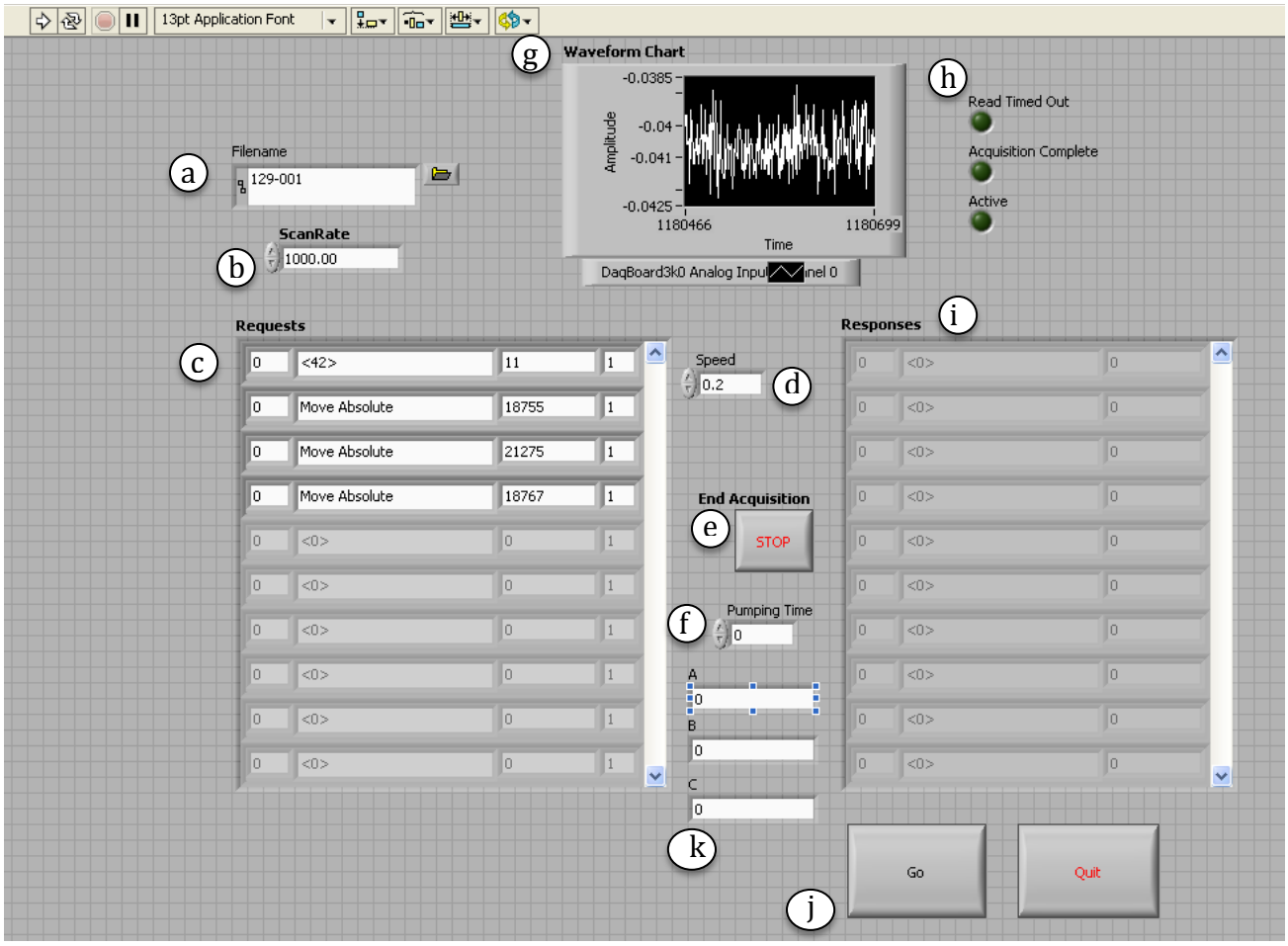

Figure 4.3: Graphic-User Interface of Experimental Apparatus

(a) Filename and directory for the data to be saved to

(b) Sampling rate adjustment

(c) Linear actuator controls

(d) Speed of indentation adjustment

(e) Ending acquisition control

(f) Perfusion control and pulsatile rate

(g) Auto-update waveform of the load cell signal

(h) Acquisition status feedback

(i) Linear actuator status feedback

(j) Send data to actuator to start and stop indentation cycle

(k) Rate of perfusion control where A,B and C each correspond to a different digit(i.e. A=1,B=0 and C=0 would result in perfusion equivalent to 100% of the maximum possible rate)

4.4.Preliminary Studies: Linear Low Density Polyethylene Modeling

In Chapters 5 and 7, LLDPE is used in the phantoms presented to model the Glisson's capsule of the liver. This section explains the testing protocol followed to conduct a parametric study to obtain the mechanical properties of this polymer.

4.4.1 Materials and Methods

The properties of the LLDPE are unknown and therefore determined using the experimental apparatus presented earlier in this chapter. A sheet of LLDPE with a thickness of 0.2mm is clamped between two plates with a 2.5" hole through them as shown in Figure 4.4 to establish boundary conditions. The LLDPE is then subjected to quasi-static loading and relaxation testing in order to determine the material properties.

Relaxation testing is performed by loading the LLDPE layer at a rate of 2mm/s to a depth of 5mm, and the force-deformation is monitored for duration of 200 seconds. Quasi-

static testing is also performed on the LLDPE where loading and unloading to a depth of 5mm is done at the same rate of 2mm/s. For these experiments the 9mm blunt indenter is used.

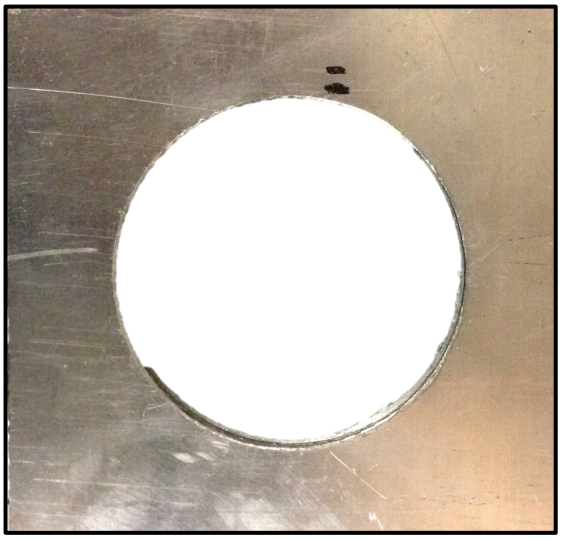

Figure 4.4: Aluminum jig used to determine the material properties of the LLDPE

4.4.2 Finite Element Analysis Modeling

The material properties of the LLDPE are determined using a parametric study. This is done using FEA modeling in ABAQUS. The simulation is made such that the boundary and physical conditions are the same as the experiment. Fixed in all degrees of freedom boundary condition is applied on the edges where the jig would be clamping the sample. A coarse and fine mesh was used in the simulation. However, there was little difference between computation times so the fine mesh, figure 4.5, was used to obtain more accurate results.

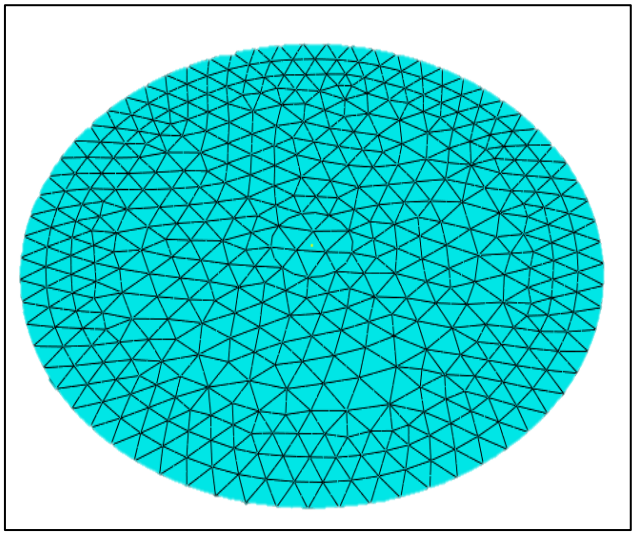

Figure 4.5: FEA Model of LLDPE Experimental Test

4.4.3 Model Fitting

The LLDPE is modeled as a Neo-Hookean hyperelastic and viscoelastic material. The viscoelastic parameters are found by fitting a three-term Prony series to Equation 24 and included in the FEA simulation (Figure 4.5). A value of 920 kg/m^3 for density of the LLDPE is used [56]. The hyperelastic material properties are determined via a parametric study from ABAQUS

4.4.4 Results

The LLDPE parametric study is fitted using the Neo-Hookean model. The parameters found are C_{10} = 3MPa and D_1 = 1 x 10^{-7} when fitting quasi-static experimental data (Figure 4.6). The relaxation testing results are presented in Figure 4.7, and yield g_1 = 0.1025, g_2 = 0.0519, g_3 = 0.0617, τ_1 = 2.768s, τ_2 = 25.0123s and τ_3 = 281.0787s for the viscoelastic parameters.

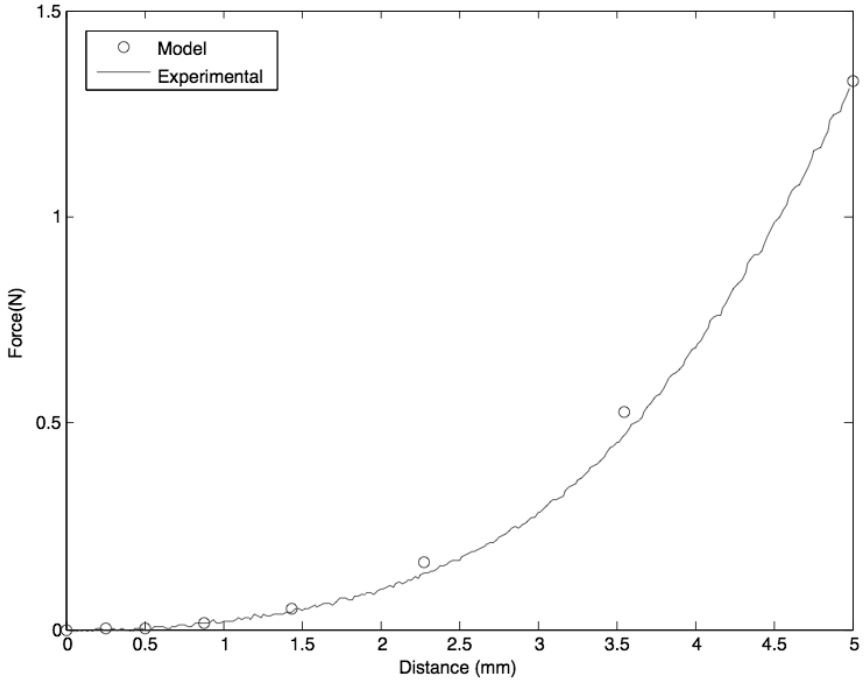

Figure 4.6: Quasi-static loading of LLDPE fitted with FEA simulation

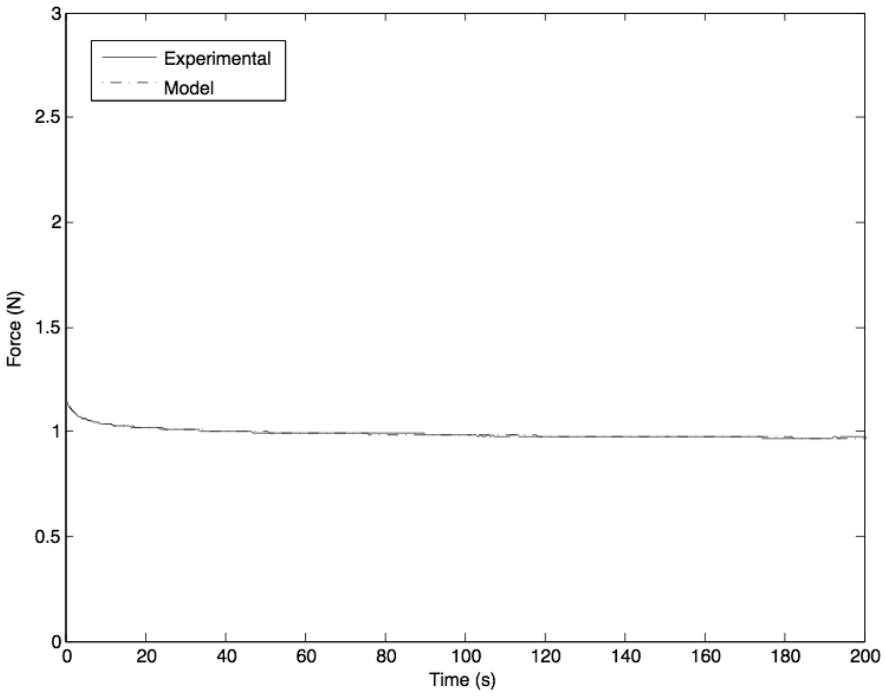

Figure 4.7: Relaxation Testing of LLDPE Fitted

4.4.5 Discussion

A parametric study was done to fit the quasi-static indentation of the LLDPE using a hyperelastic, viscoelastic model. The neo-Hookean model requires two different parameters, C_{10} and D_1, which were varied until a reasonable fit was achieved. The fitting parameters obtained using the parametric study yielded results with average relative error of 7.9% when compared to the experimental data. However, a model with more parameters such as a second-order reduced polynomial hyperelastic model would further capture the behavior of the LLDPE but that option was disregarded due to the difficulty and computation time.

Chapter 5 : Fluid-Filled Phantoms

In this chapter a fluid-filled phantom is developed. Currently, most phantoms are composed of single component materials [33,34], which do not take into consideration the fluid phase of soft tissues. Several hydrogel phantoms have been created [45,46] to account for the fluid phase, and they are relatively cheap to manufacture. The downfall of these is the time required to create them. In this phantom, composed of a LLDPE vessel that will represent the Glisson's capsule and a fluid phase to represent the bulk of the organ. This design will be not only be cost effective but also time efficient. The objective is to create simple phantoms that mimic the general biomechanical properties of internal organs and soft tissue, and could be used to develop computationally efficient analytical or numerical models that can be used in surgical simulators and trainers. These phantoms could also be used in calibration of soft tissue indentation sensors. The phantoms can be used to investigate the effects of many parameters such as the density and viscosity of the fluid, the size of the phantom and its boundary conditions. In addition, many internal organs such as the stomach and the gall bladder may be modeled as fluid-filled bags [44].

5.1.Materials and Methods

Three phantoms composed of a LLDPE bag filled with three different fluids: water, 1:1 glycerine/water mixture and glycerine. A volume of 500mL of fluid was poured in the LLDPE bag, the air bubbles were removed and the fluid was allowed to reach room temperature prior to testing due to potential viscosity changes.

The density and viscosity of each fluid used in the construction of phantoms is presented in Table 5-1. The effects of the size of the phantom were done by testing three different bags filled each filled with a different volume of fluid; 400mL, 500mL and 600mL. Comparing force-displacement results of the phantoms in both confined and unconfined conditions will be used to study the effect of boundary conditions. The confined case consists of having tape restricting the movement of the edges during indentation while the unconfined case is non-restricted.

Table 5-1 : Dynamic Viscosity, Density and Ratio of Fluids Used in the Phantoms

	Properties		
Fluid	**Dynamic Viscosity (Ns/m^2)**	**Ratio (Fluid: Water)**	**Density (Kg/m^3)**
Water	0.00098069	1:1	997.80
1:1 Water/Glycerine Mixture	0.0080587	8.2174:1	1146.1
Glycerine	1.2901	1315.505:1	1263.3

5.1.1 Quasi-Static Indentation Testing

Quasi-static indentation testing was performed using the experimental apparatus described in Chapter 4. The results will yield a force-displacement relation, which will be used to determine the effects of density and viscosity of the phantom, its size as well as the boundary conditions. The indentation was done for loading and unloading to a depth of 5mm at rates of 0.2mm/s, 1mm/s and 2mm/s.

5.1.2 Relaxation Testing

Relaxation testing was performed using the experimental apparatus outlined in Chapter 4 with aim to characterize the viscoelastic behavior of the phantoms. The test consists of loading the phantom at a rate of 2mm/s to a depth of 5mm where the force-deformation is monitored for duration of 200 seconds.

5.2.Results

5.2.1 Quasi-Static Indentation Testing

Quasi-static experiment results conducted on the unconfined phantom using the blunt 9mm indenter (Figures 5.1 - 5.3) and the spherical 2mm indenter (Figures 5.4 - 5.6) are presented for each of the three different loading rates. In Figures 5.7 - 5.9 and 5.10 - 5.12, the data is presented in terms of the different fluids for the 9mm indenter and 2mm indenter, respectively. In each of the following figures presenting the quasi-static indentation data, loading and unloading can be seen. The loading in all cases is the higher of the two curves and the unloading in the lower one.

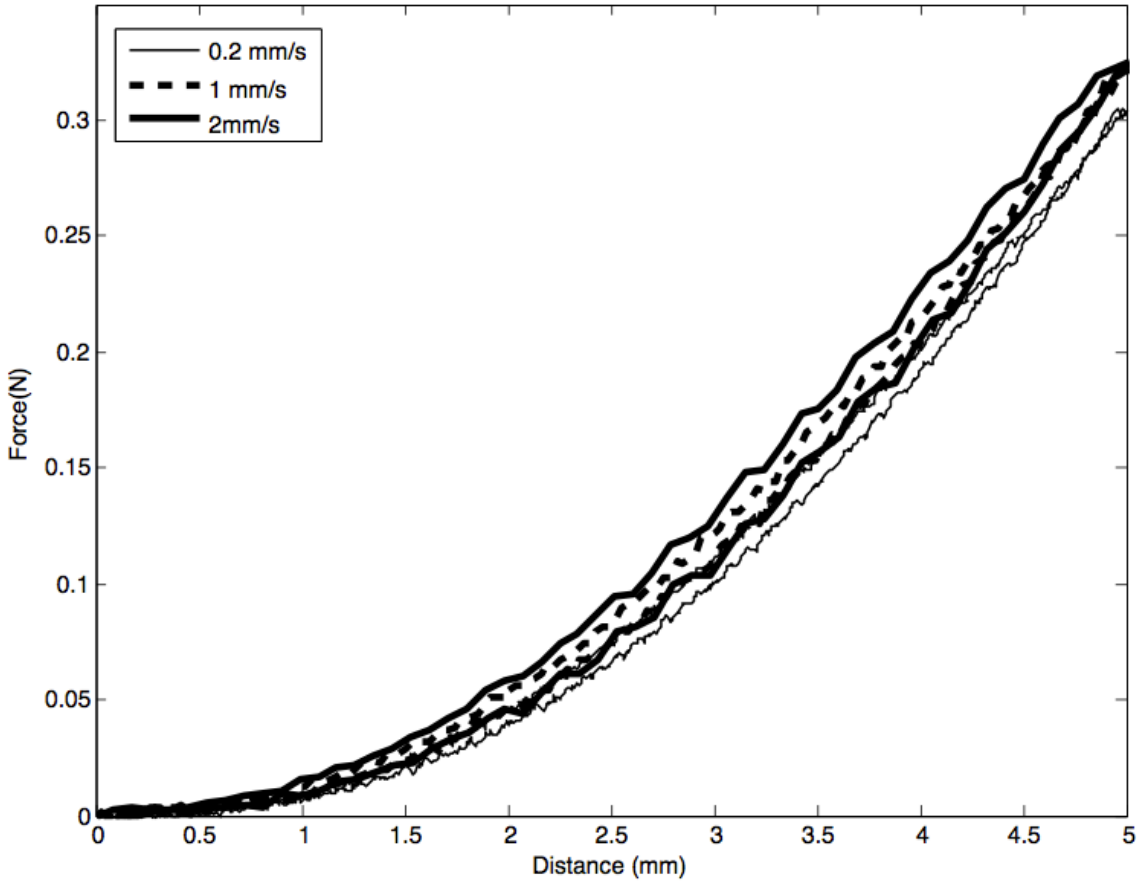

Figure 5.1: Unconfined Quasi-Static Indentation using 9mm Indenter (Loading and Unloading) of Water

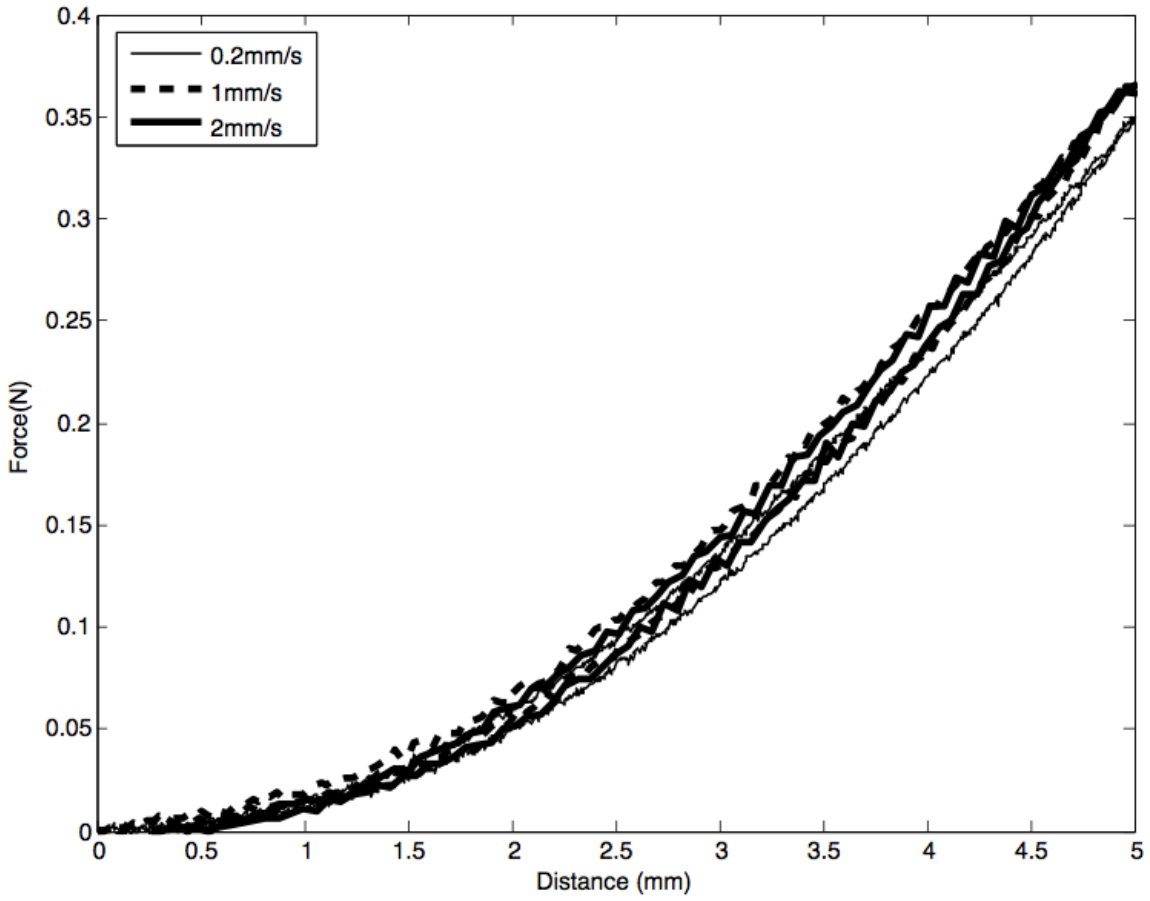

Figure 5.2: Unconfined Quasi-Static indentation using 9mm Indenter(Loading and Unloading) of 1:1 Water/Glycerine Mixture

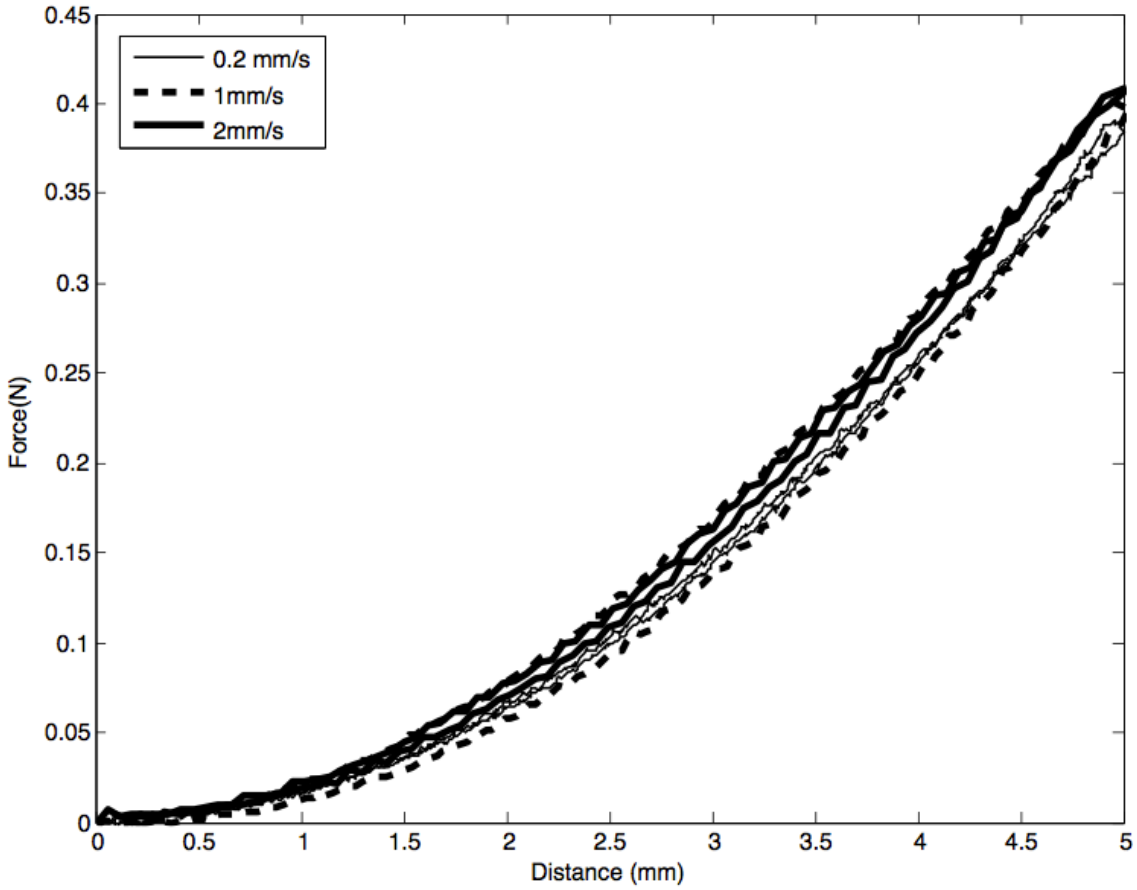

Figure 5.3: Unconfined Quasi-Static Indentation using 9mm Indenter (Loading and Unloading) of Glycerine

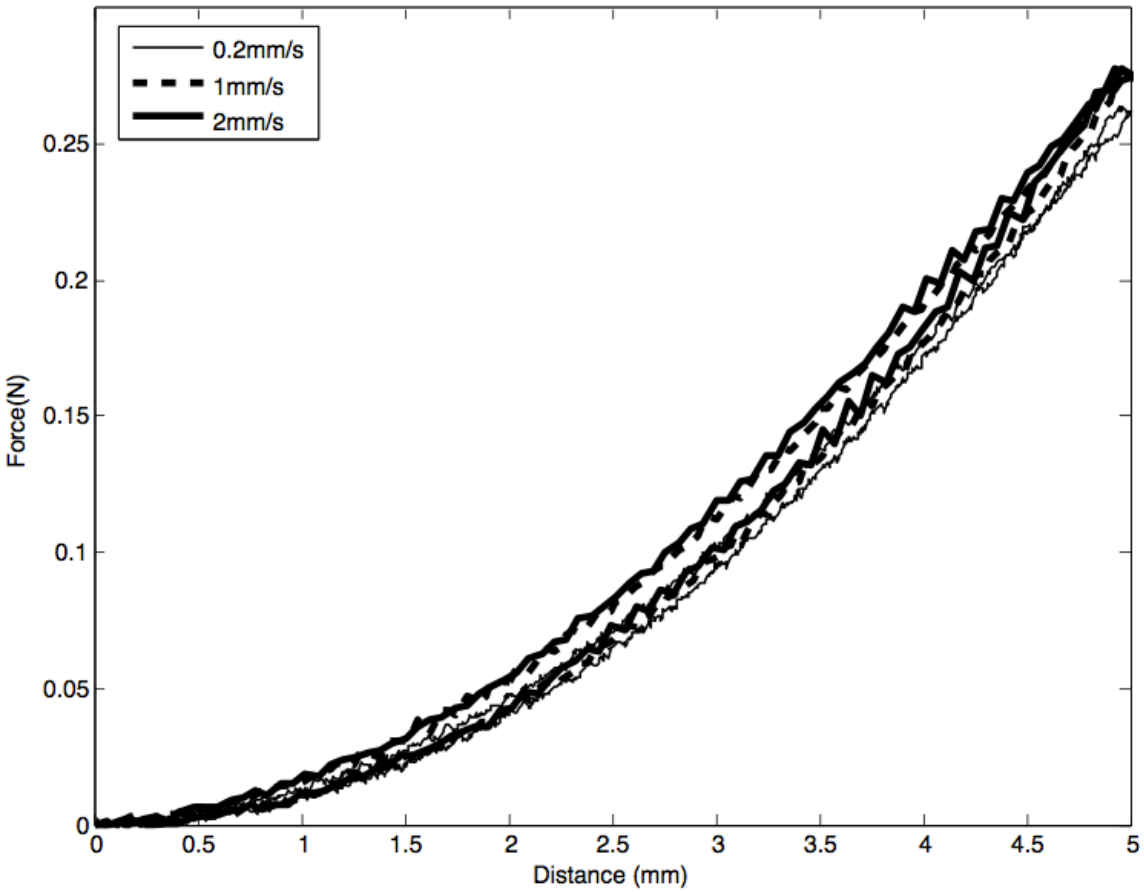

Figure 5.4: Unconfined Quasi-Static Indentation using 2mm Indenter (Loading and Unloading) of Water

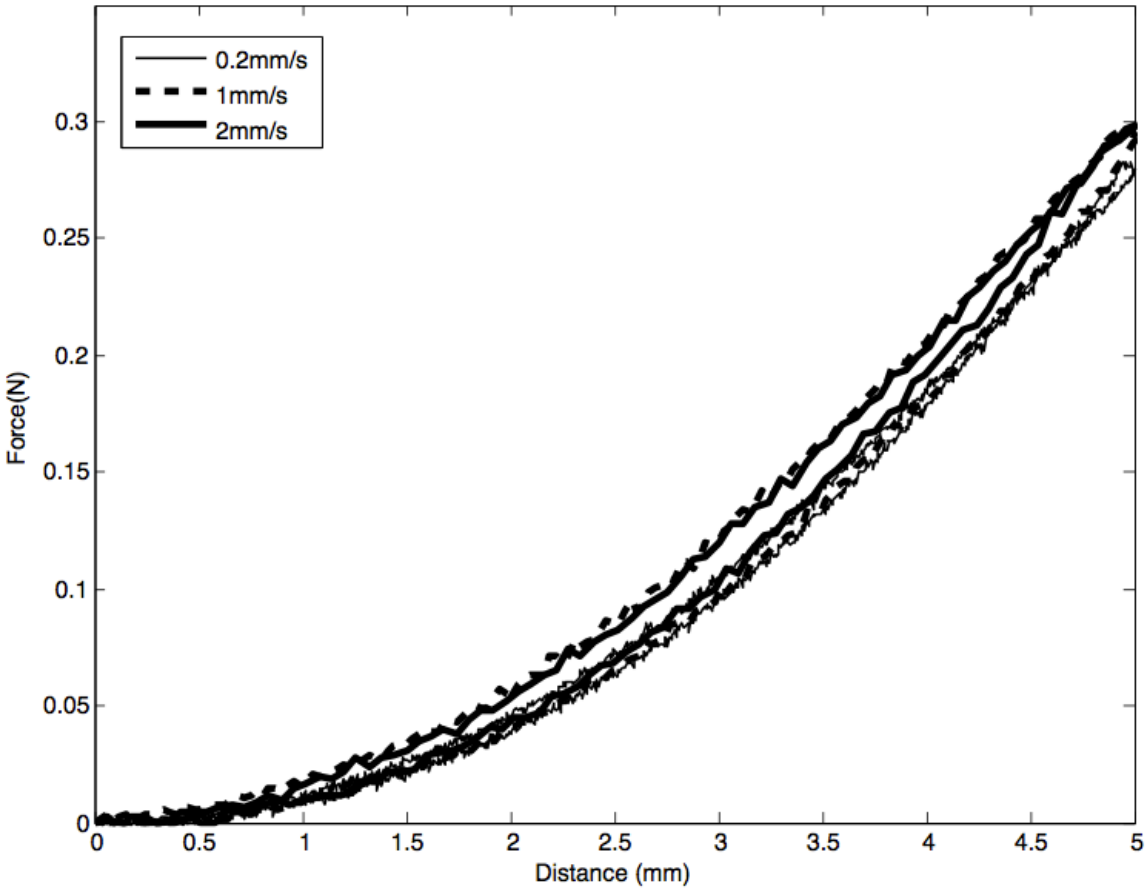

Figure 5.5: Unconfined Quasi-Static Indentation using 2mm Indenter (Loading and Unloading) of 1:1 Water/Glycerine Mixture

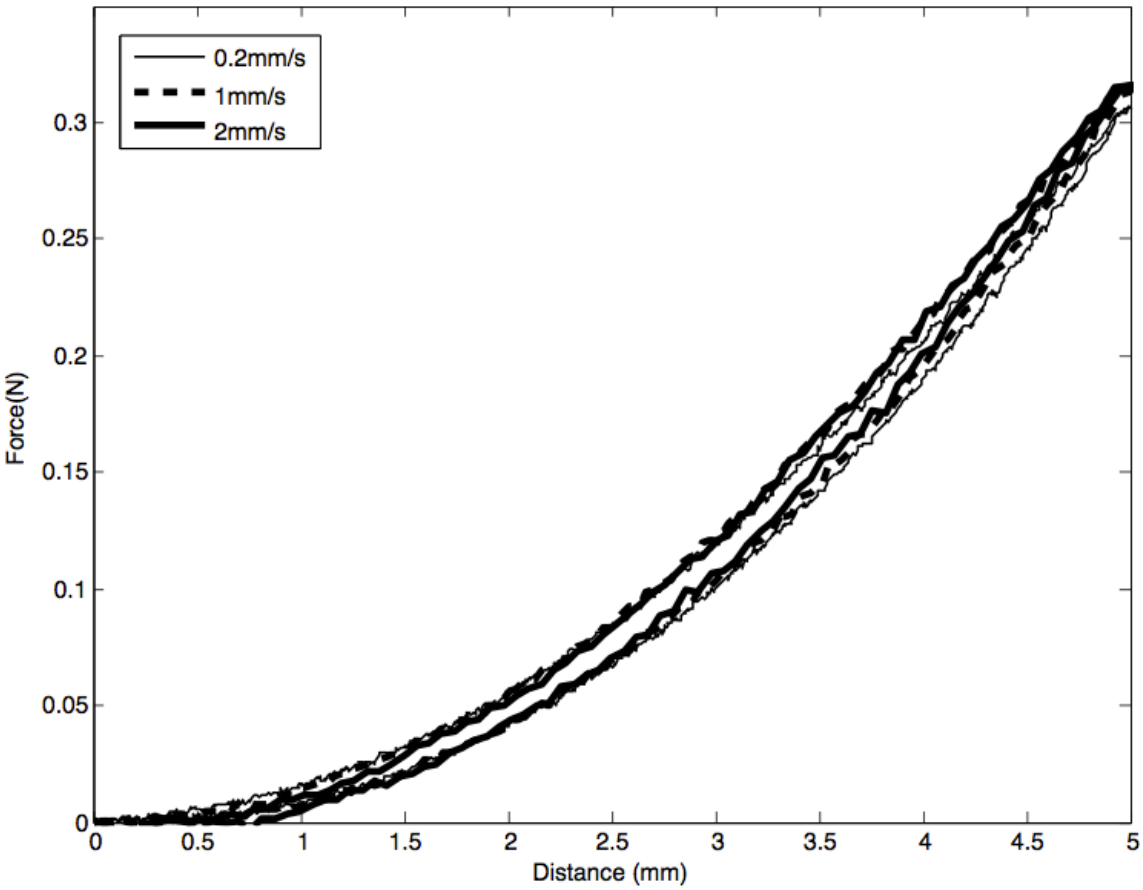

Figure 5.6: Unconfined Quasi-Static Indentation using 2mm Indenter (Loading and Unloading) of Glycerine

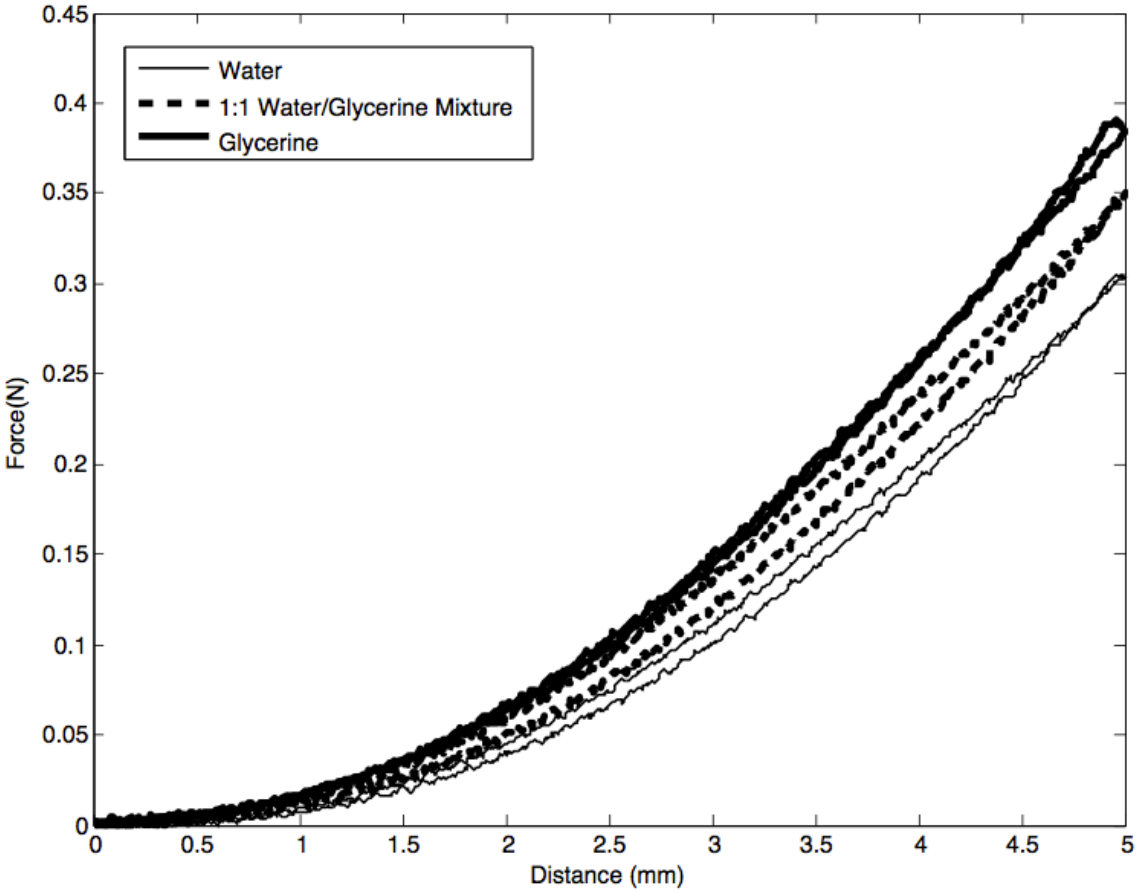

Figure 5.7: Unconfined Quasi-Static Indentation using 9mm Indenter (Loading and Unloading) at a rate of 0.2 mm/s

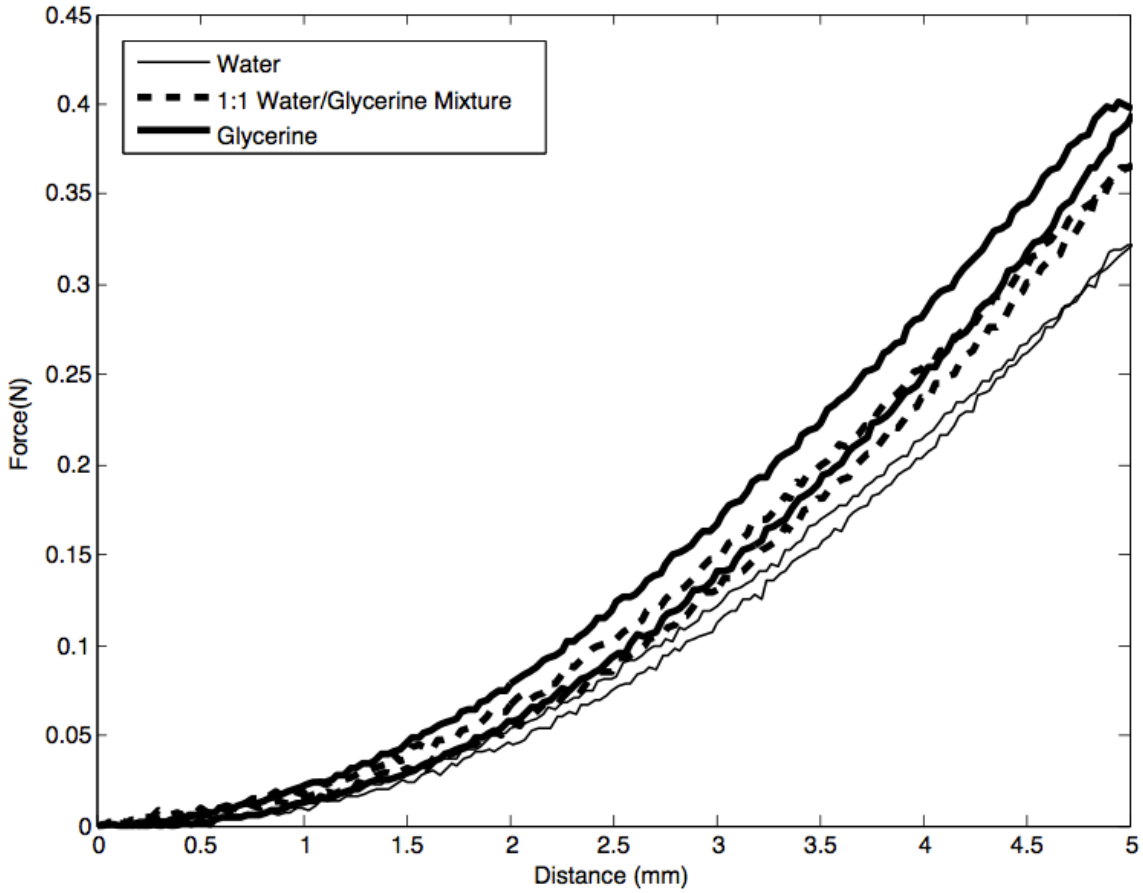

Figure 5.8: Unconfined Quasi-Static Indentation using 9mm Indenter (Loading and Unloading) at a rate of 1mm/s

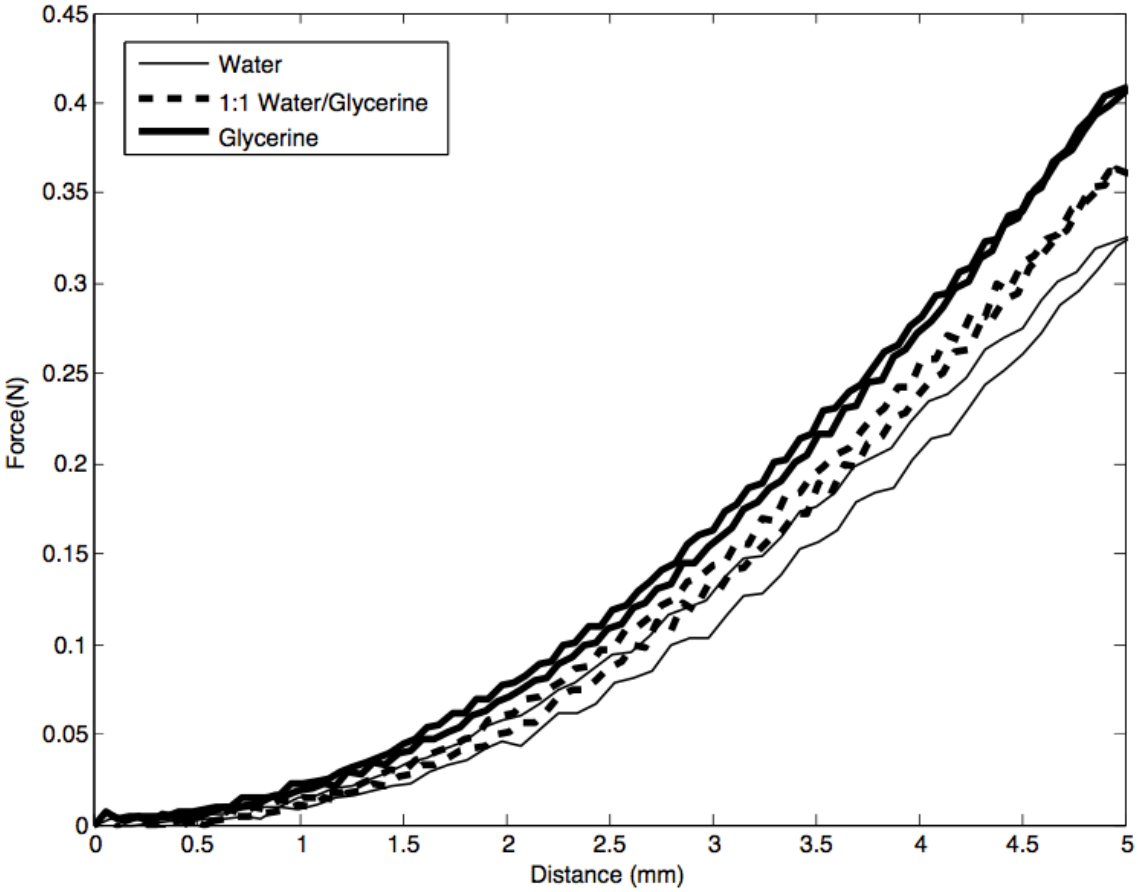

Figure 5.9: Unconfined Quasi-Static Indentation using 9mm Indenter (Loading and Unloading) at a rate of 2mm/s

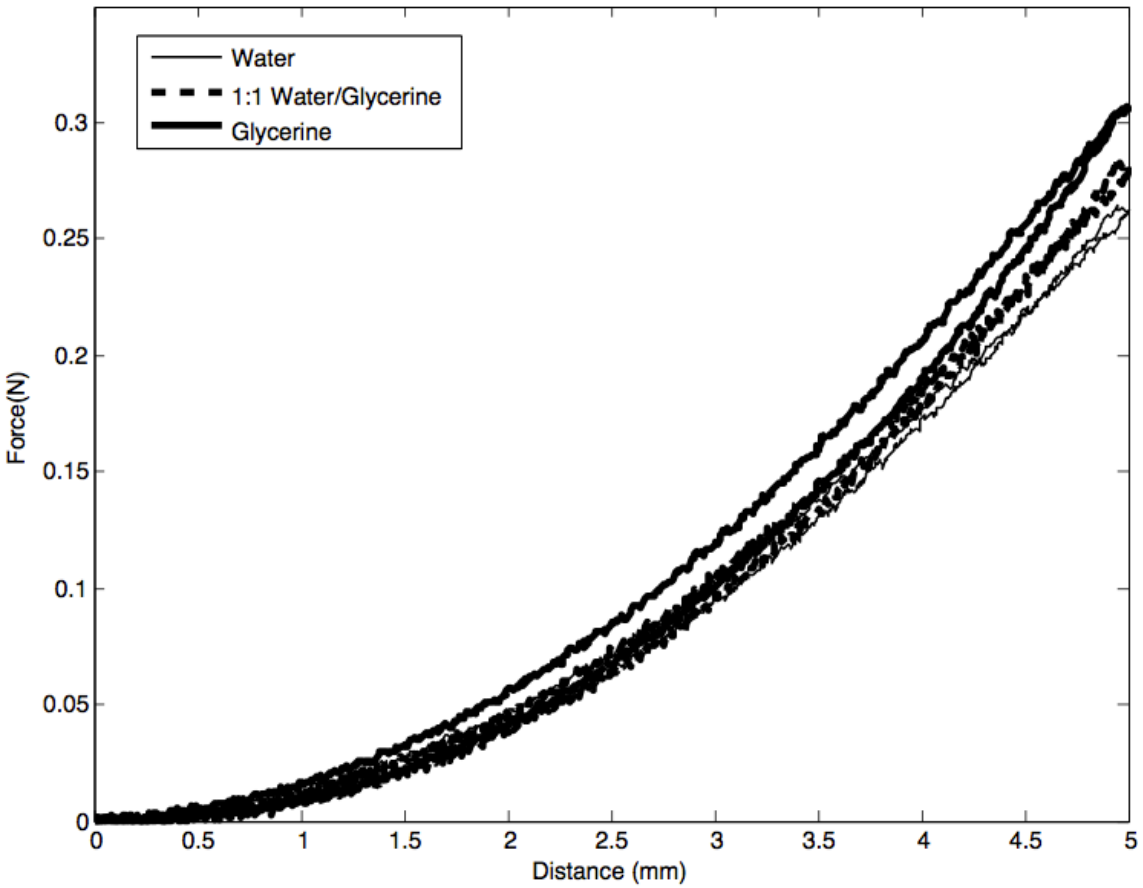

Figure 5.10: Unconfined Quasi-Static Indentation using a 2mm Indenter (Loading and Unloading) at a rate of 0.2mm/s

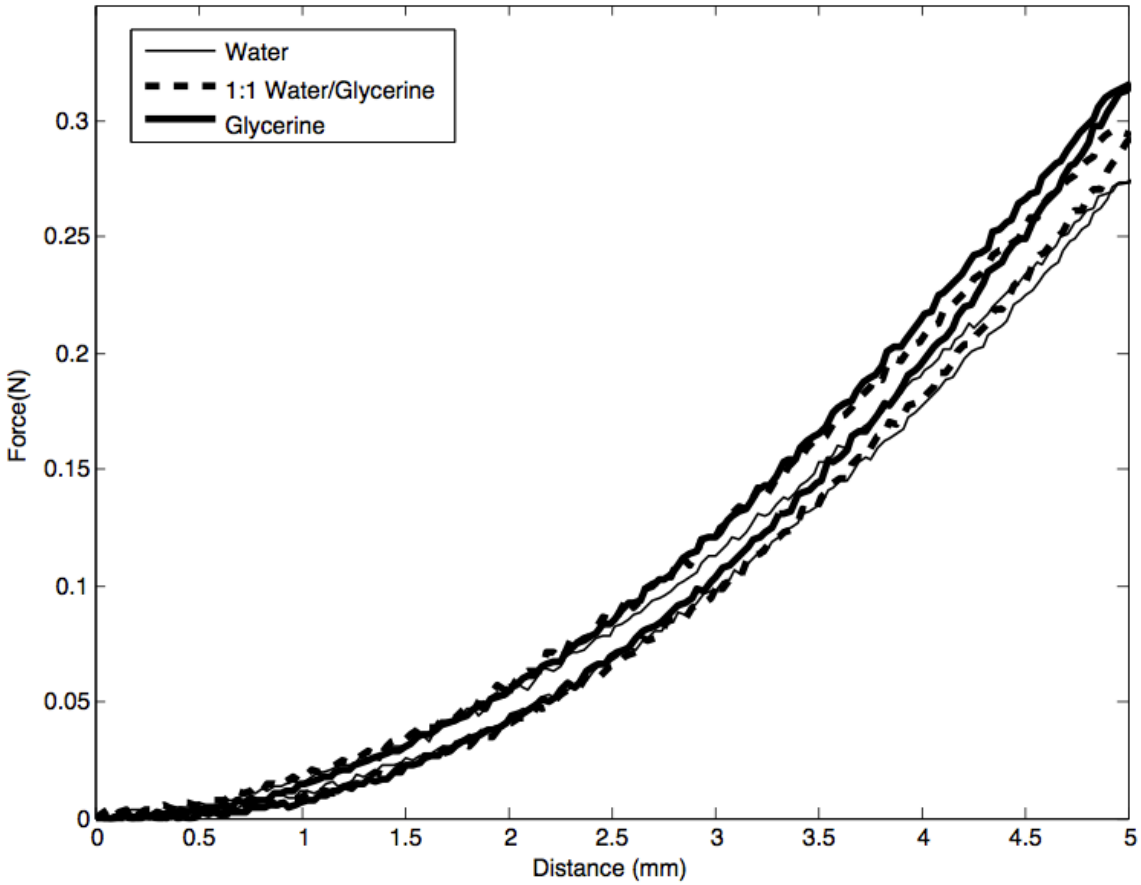

Figure 5.11: Unconfined Quasi-Static Indentation using a 2mm Indenter (Loading and Unloading) at a rate of 1mm/s

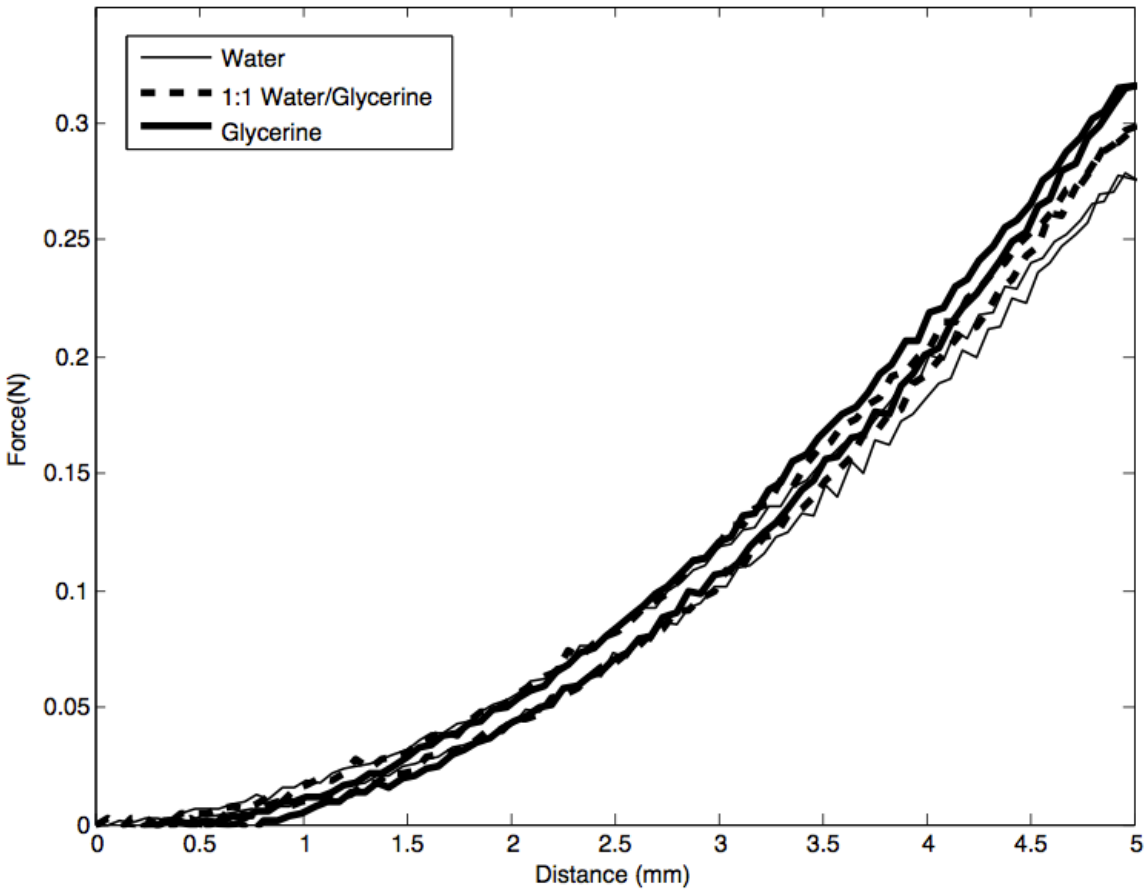

Figure 5.12: Unconfined Quasi-Static Indentation using a 2mm Indenter (Loading and Unloading) at a rate of 2mm/s

The results of quasi-static indentation experiment on the confined phantom using the blunt 9mm indenter (Figures 5.13 - 5.15) and the spherical 2mm indenter (Figures 5.19 - 5.21) are presented for each of the three different loading rates. In Figures 5.16 - 5.18 and 5.22 - 5.24, the data is presented in terms of the different fluids for the 9mm indenter and 2mm indenter, respectively.

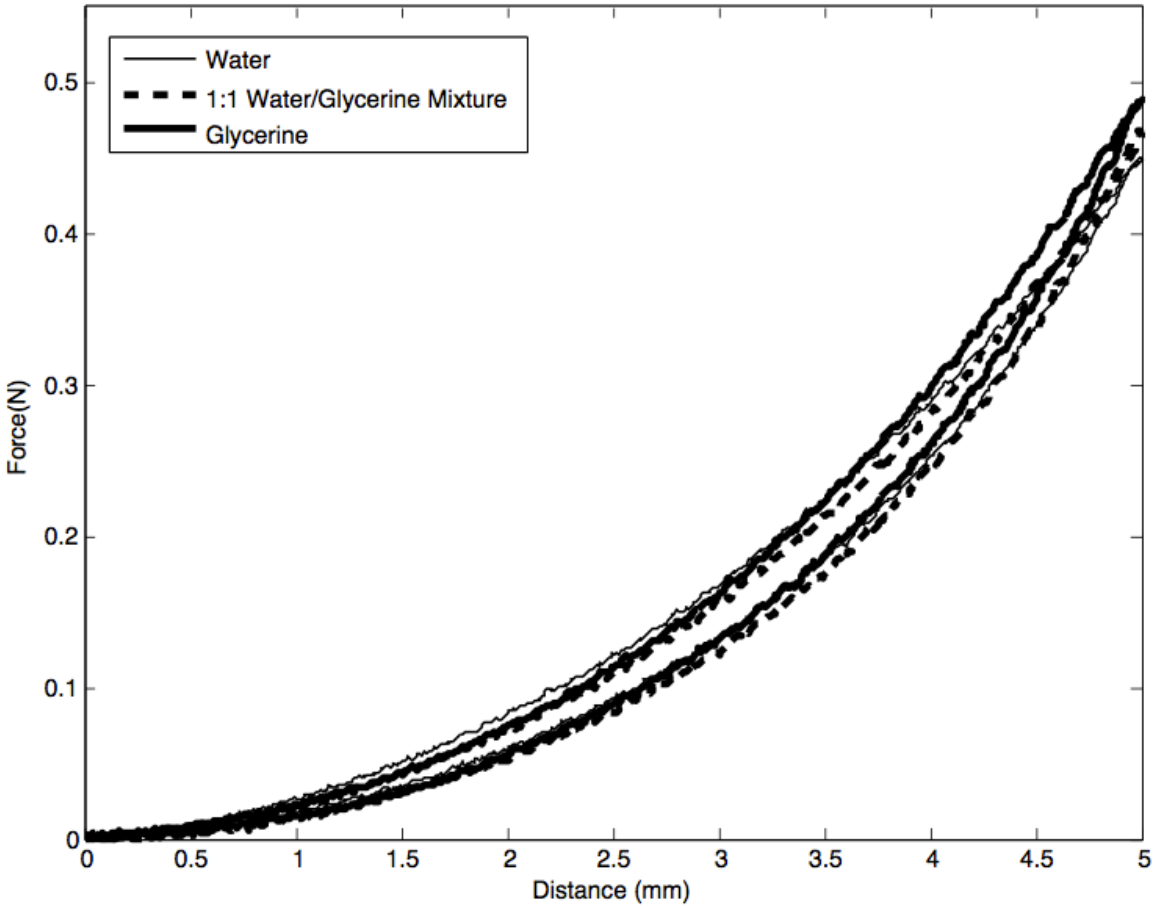

Figure 5.13: Confined Quasi-Static Indentation (Loading and Unloading) using 9mm Indenter at a rate of 0.2mm/s

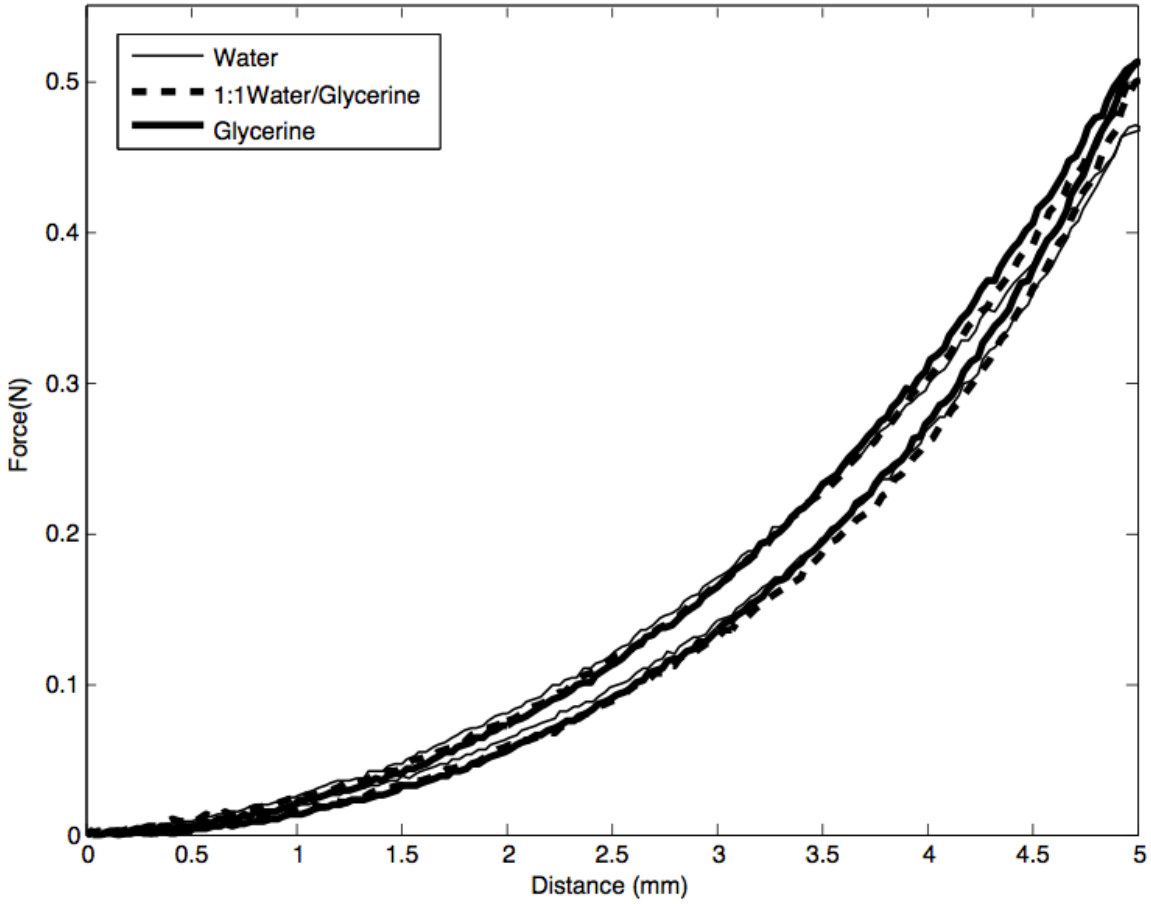

Figure 5.14: Confined Quasi-Static Indentation (Loading and Unloading) using 9mm Indenter at a rate of 1mm/s

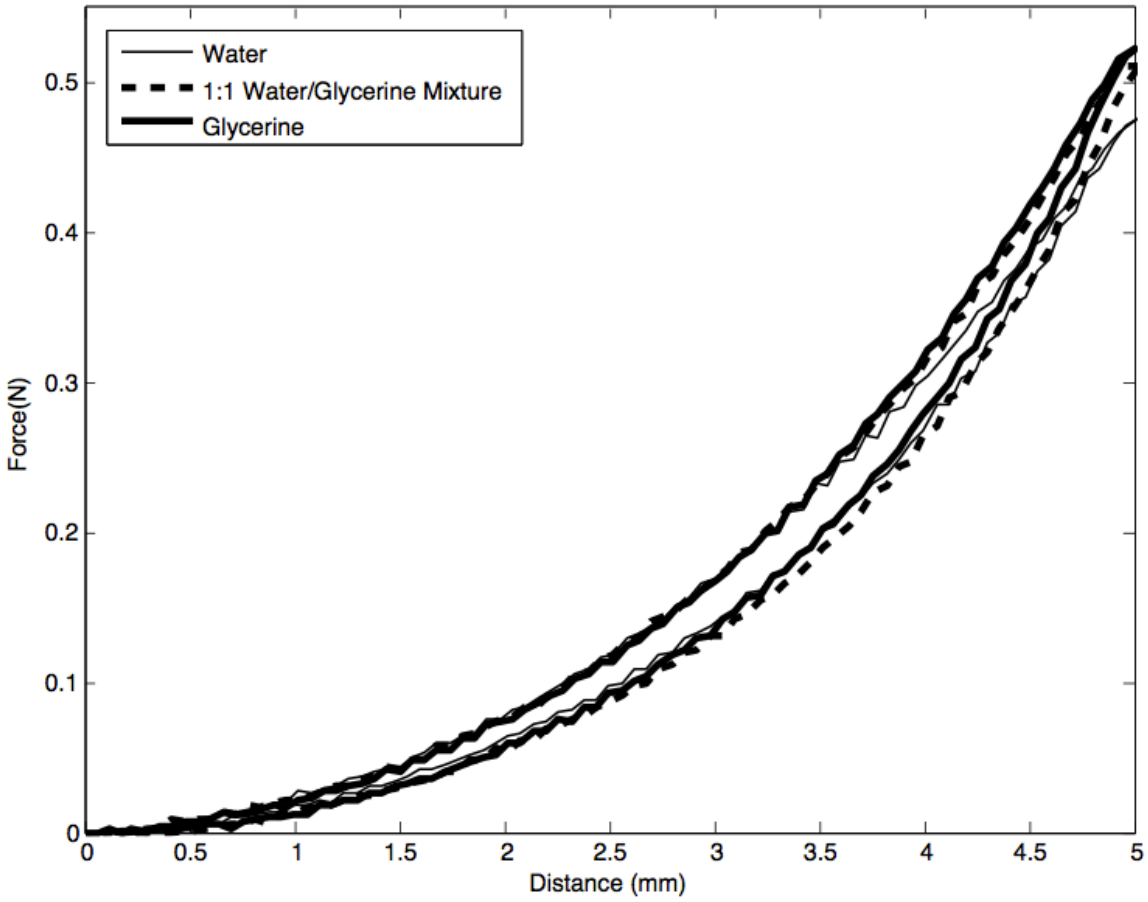

Figure 5.15: Confined Quasi-Static Indentation (Loading and Unloading) using 9mm Indenter at a rate of 2mm/s

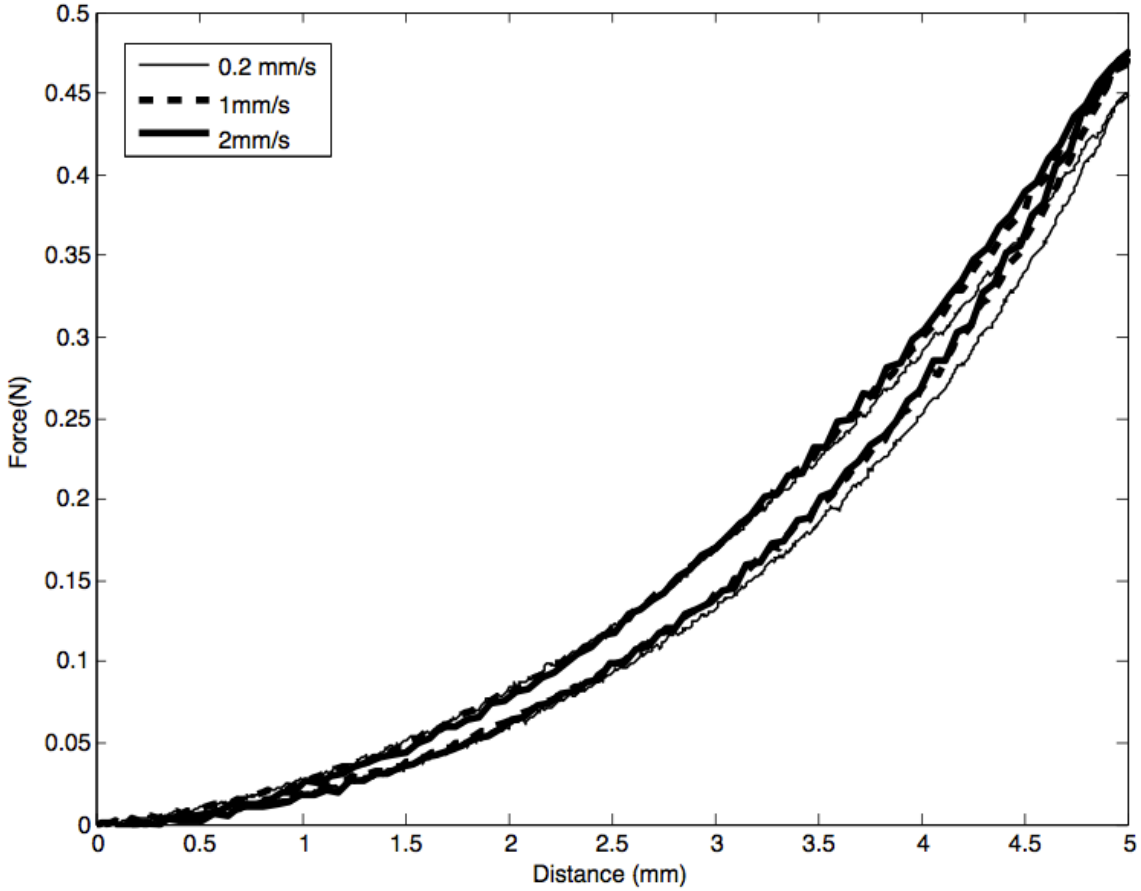

Figure 5.16: Confined Quasi-Static Indentation (Loading and Unloading) using 9mm Indenter of Water

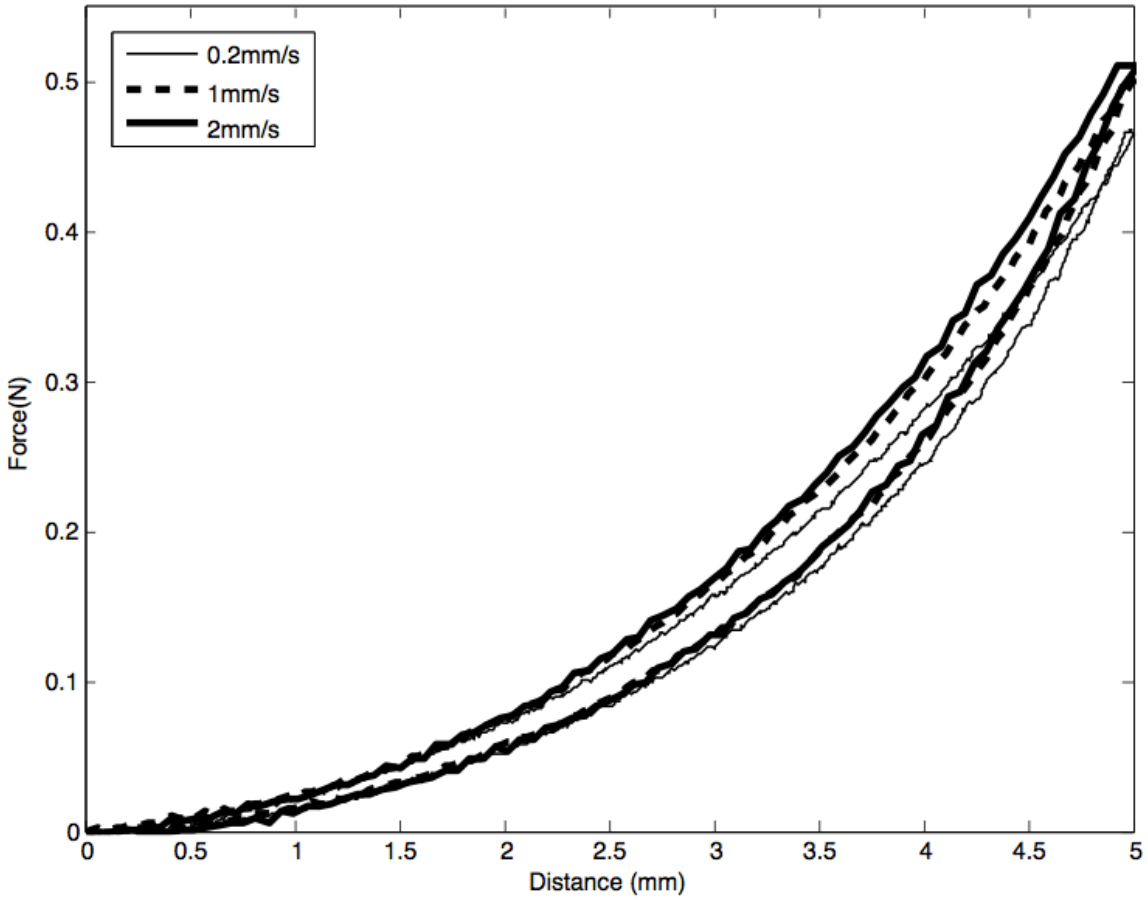

Figure 5.17: Confined Quasi-Static Indentation (Loading and Unloading) using 9mm Indenter of 1:1 Water/Glycerine Mixture

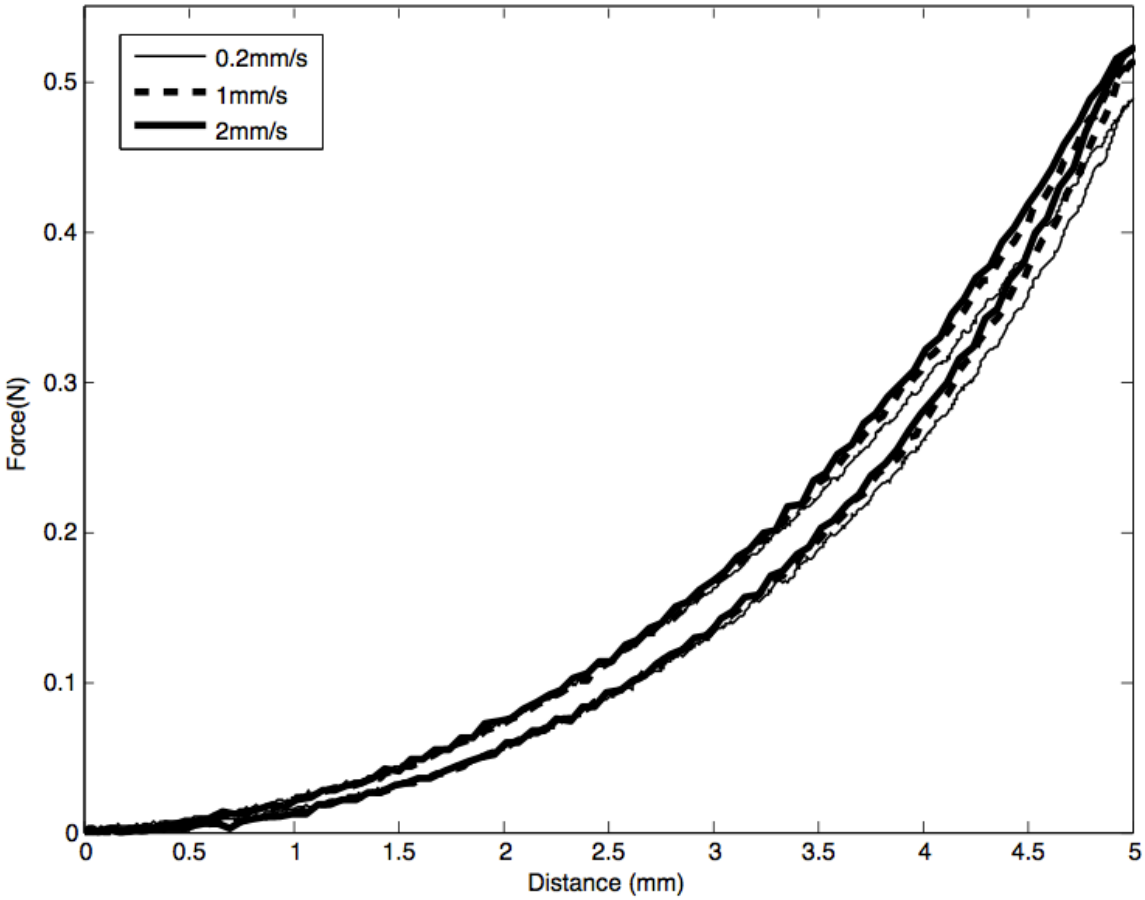

Figure 5.18: Confined Quasi-Static Indentation (Loading and Unloading) using 9mm Indenter of Glycerine

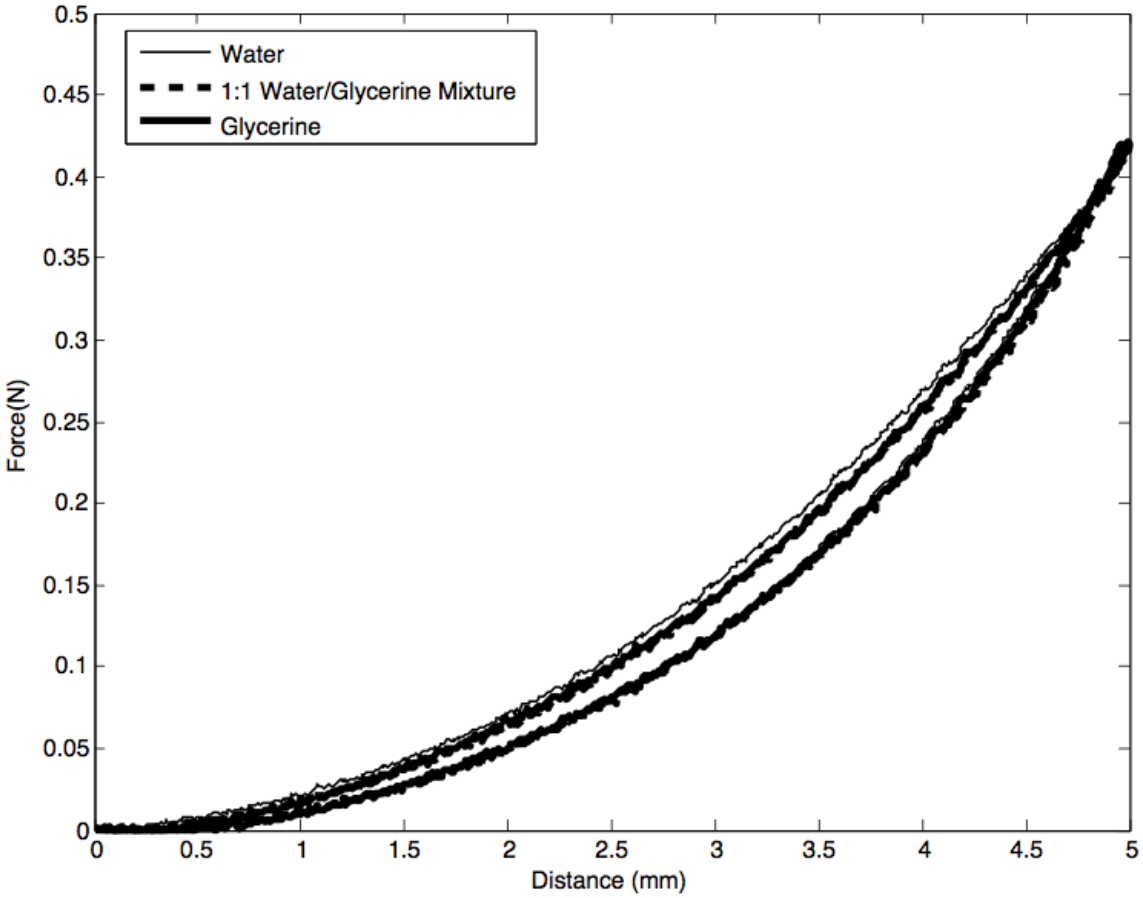

Figure 5.19: Confined Quasi-Static Indentation (Loading and Unloading using 2mm Indenter at a rate of 0.2mm/s

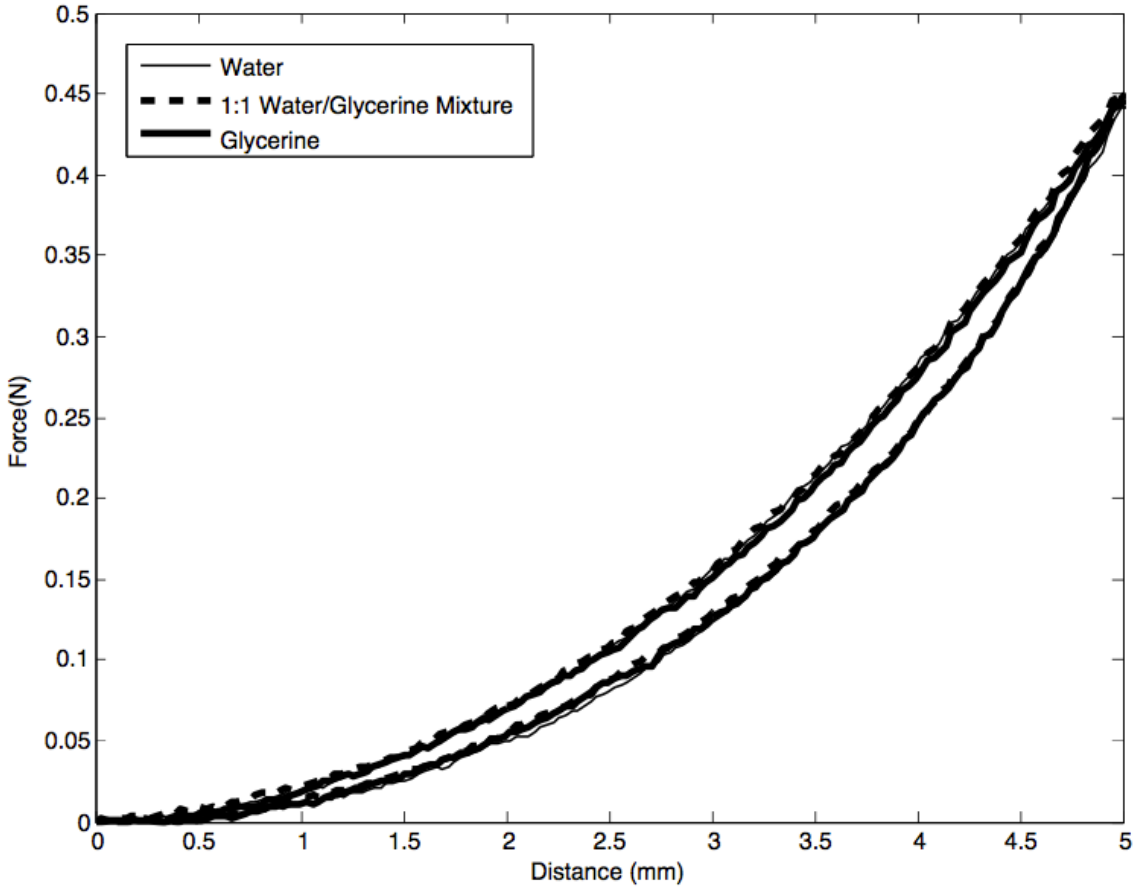

Figure 5.20: Confined Quasi-Static Indentation (Loading and Unloading using 2mm Indenter at a rate of 1mm/s

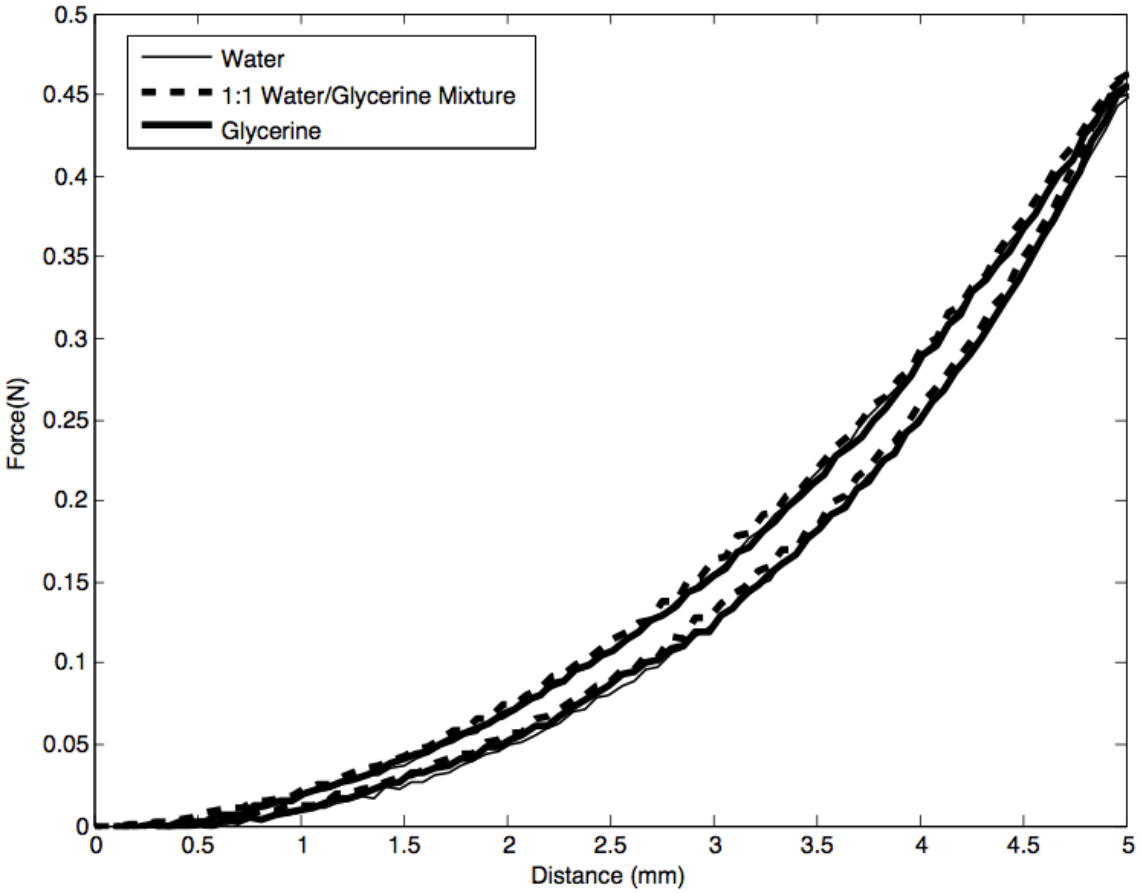

Figure 5.21: Confined Quasi-Static Indentation (Loading and Unloading using 2mm Indenter at a rate of 2mm/s

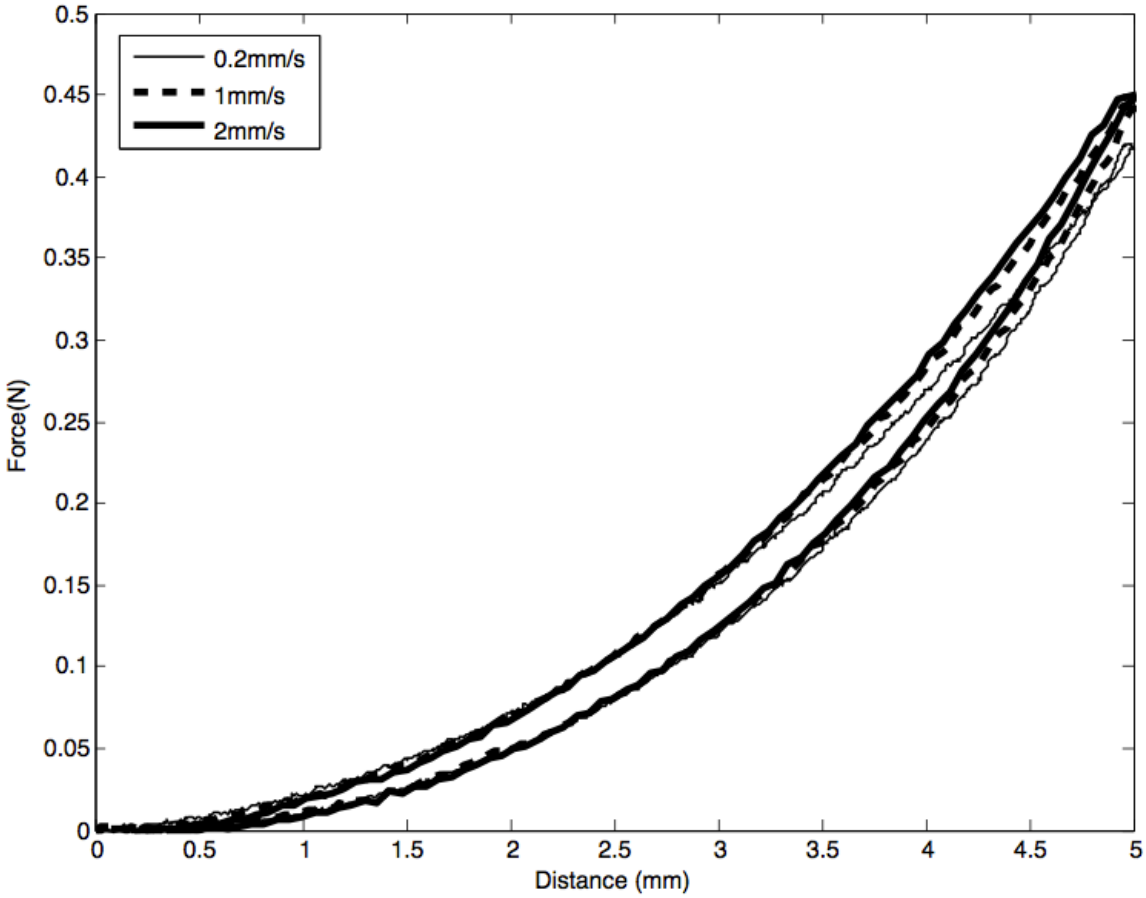

Figure 5.22: Confined Quasi-Static Indentation (Loading and Unloading using 2mm Indenter of Water

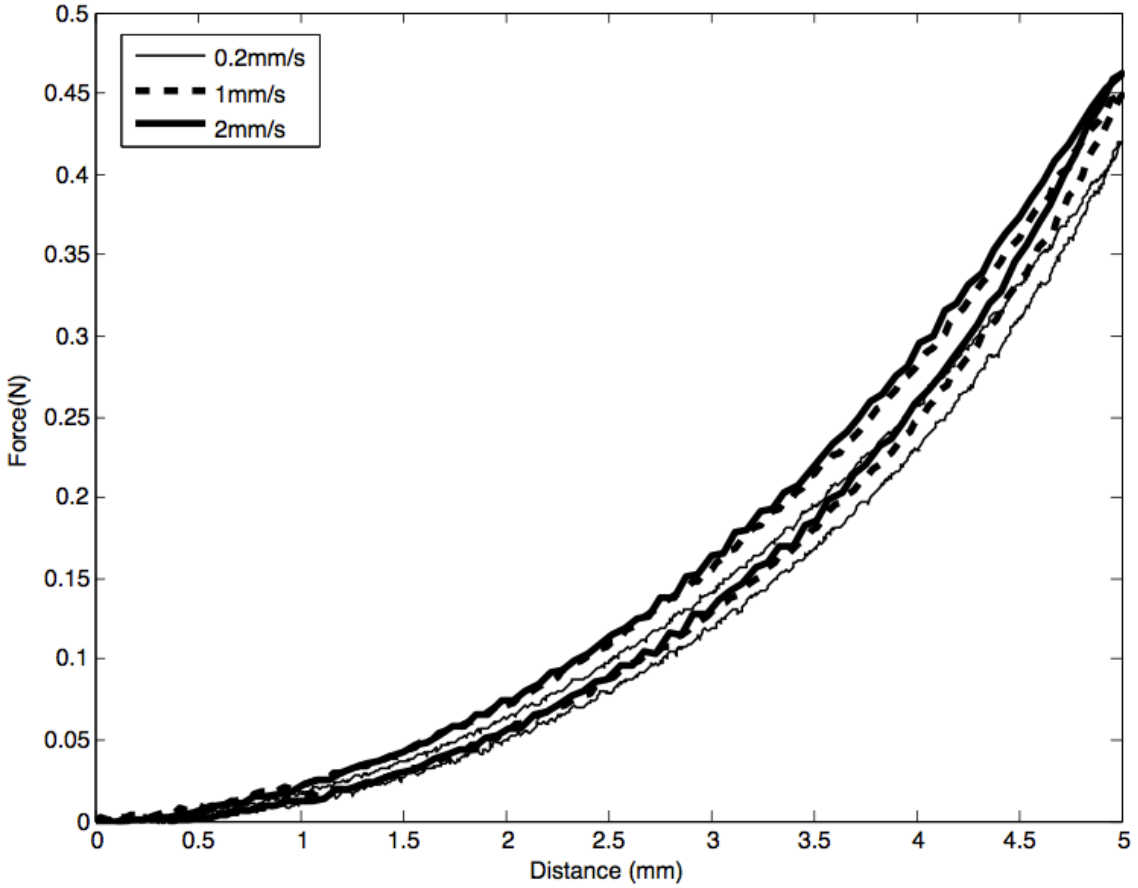

Figure 5.23: Confined Quasi-Static Indentation (Loading and Unloading using 2mm Indenter of 1:1 Water/Glycerine Mixture

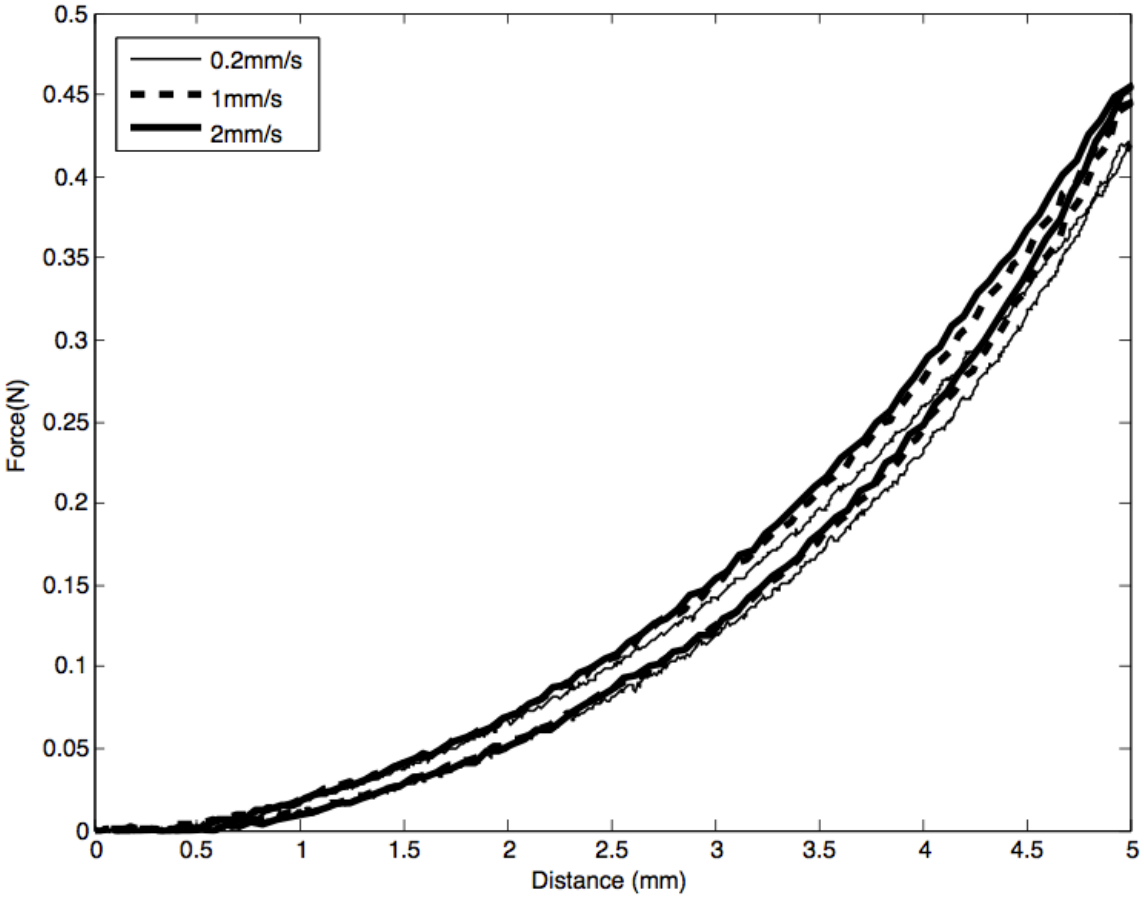

Figure 5.24: Confined Quasi-Static Indentation (Loading and Unloading using 2mm Indenter of Glycerine

5.2.1.1. Effect of Size of Phantom

The results from quasi-static indentation of three water-filled phantoms under unconfined boundary conditions each with different water volume is shown in Figure 5.25 while the confined condition is shown in Figure 5.26.

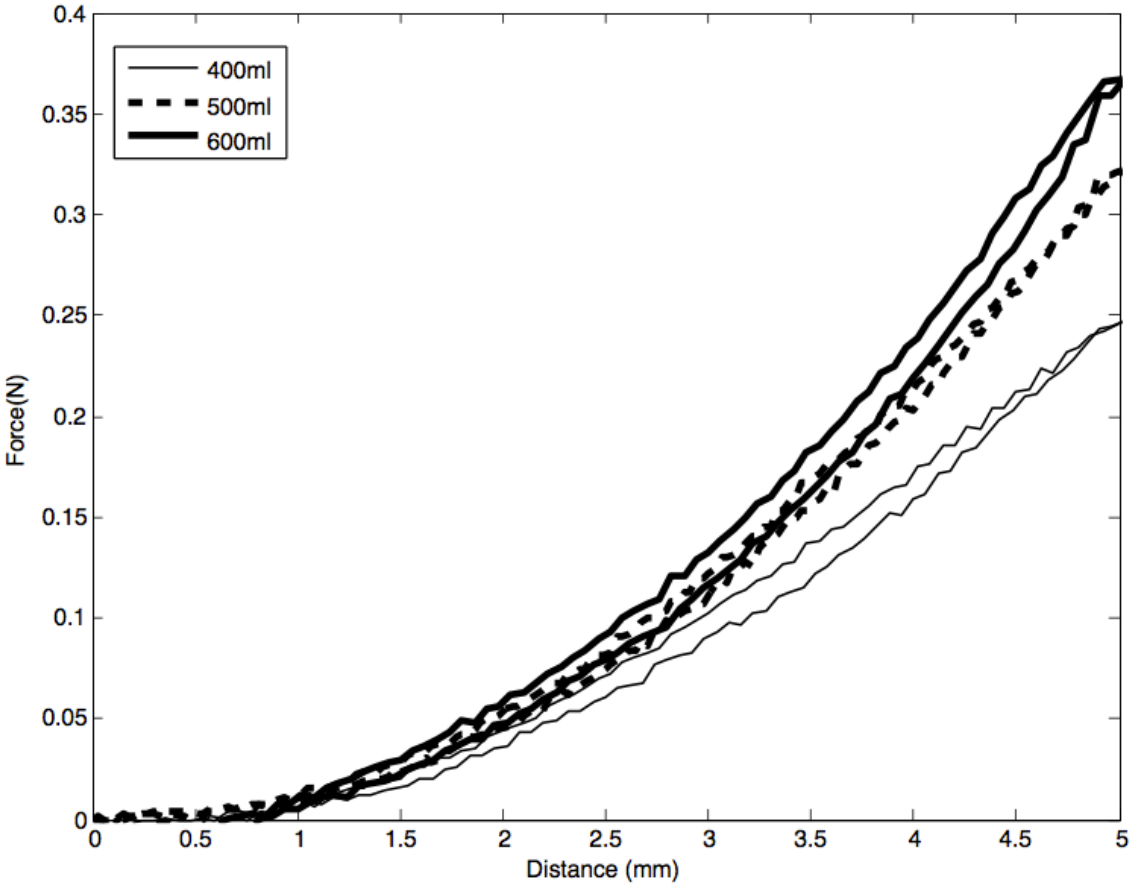

Figure 5.25: Unconfined Quasi-Static Indentation using 9mm Indenter of Phantoms with Three Different Volumes at a rate of 2mm/s

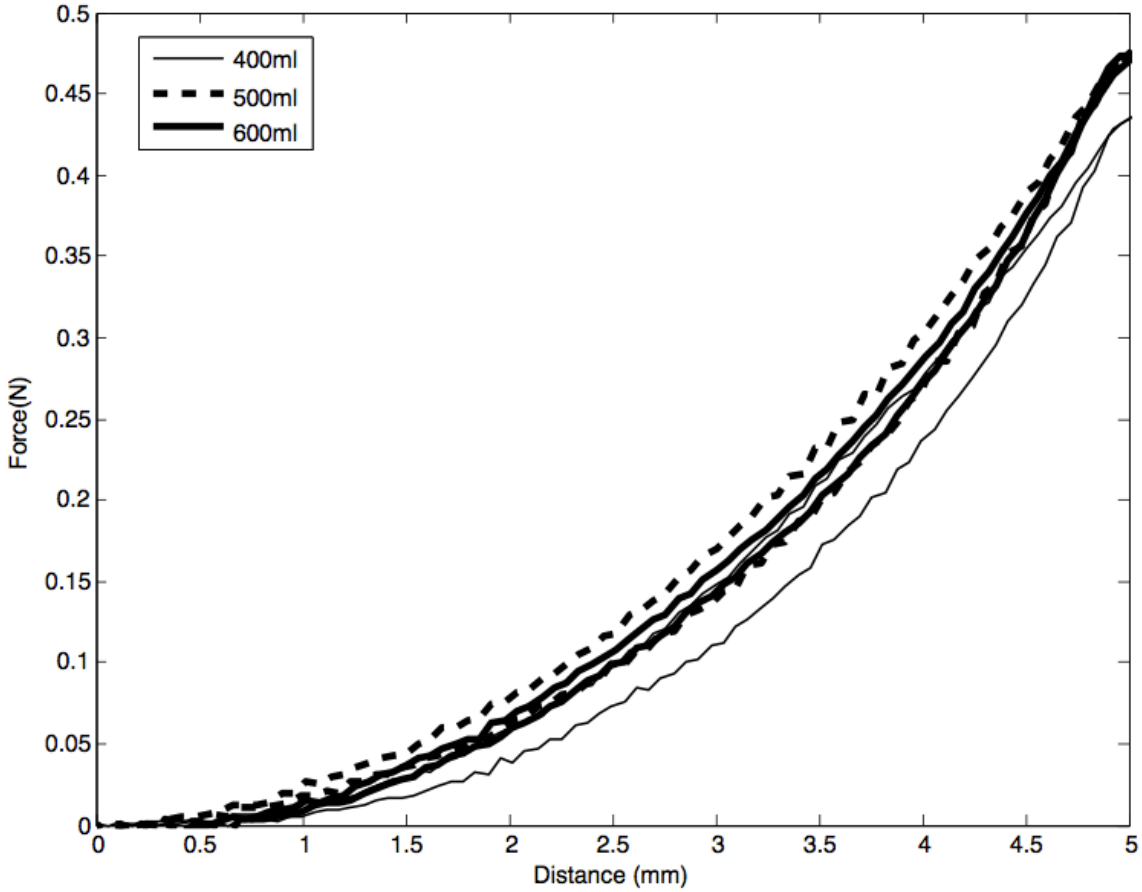

Figure 5.26: Confined Quasi-Static (Loading and Unloading) using 9mm Indenter of Phantoms with Three different Volumes at a rate of 2mm/s.

5.2.2 Relaxation Testing

Table 5-2: Viscoelastic Parameters of the Unconfined Fluid-Filled Phantoms

Fluid	Relaxation Parameters					
	g_1	g_2	g_3	τ_1 (s)	τ_2 (s)	τ_3 (s)
Water	0.0197	0.0189	0.0625	4.3029	36.1497	590.5834
1:1 Water/Glycerine Mixture	0.0199	0.0213	0.0279	2.8404	24.1671	190.6318
Glycerine	0.0182	0.0179	0.0241	4.2807	40.6645	376.8521

The relaxation testing results were fitted using Equation 24 and presented in Figure 5.27. The coefficients obtained from fitting the experimental data are displayed in Table 5-1. The relaxation spectrum is similar to the results reported by Raghunathan et al. [39] for porcine liver and Nava et al. [3] for human liver.

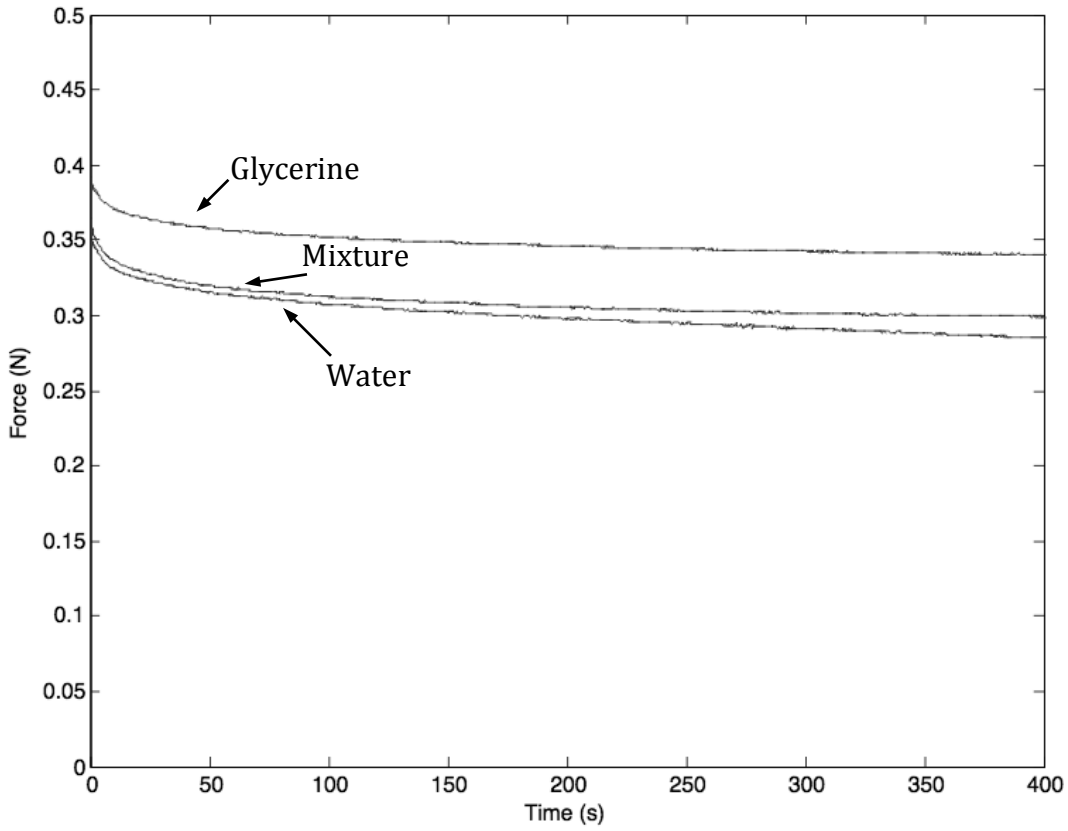

Figure 5.27: Relaxation Data of Fluid-Filled Phantoms Using 9mm Indenter Without Boundary Conditions

5.3.Discussion

The quasi-static indentation experiments were conducted using both the 9mm indenter and the 2mm indenter. The trend in the data shows no significant difference between the

different indenters. The 9mm indenter exhibited higher force output than the 2mm one, which is expected due to the surface areas of each of the indenters.

The effects of density and viscosity can be seen in Figures 5.1 - 5.12 and 5.13 - 5.24 for the unconfined and confined boundary conditions, respectively. In the unconfined case, there is a proportional relation between the force-displacement output and the density of the fluid. However, those same relations are minimized in the confined boundary conditions experiments where the edges of the phantom are restricted from movement. This is due to the rise of the edges of the phantom during indentation seen in Figure 5.28. A force is then required to raise those edges above the platform. It is observed that, since the difference between different densities is minimized in the confined case, with an increase in density, a higher force is required to raise the edges.

(a) (b)

Figure 5.28: Indentation of Fluid-Filled Phantoms: (a) at rest and (b) fully loaded

The rate at which fluid moves through the phantom can be related to its dynamic viscosity. The equation to determine dynamic viscosity of water, glycerine and the 1:1

water/glycerine mixture presented in Chapter 3 yields the values shown in Table 5-1. From the data in Figures 5.1 - 5.24, it can be seen that the influence of viscosity on the force-displacement output of the phantoms is minimal.

The experiment done to study the effect of the volume of fluid showed a proportional relation between the volume of fluid and the force-displacement output in the unconfined case (Figure 5.25). This is due to the rise of the bag since the bag are filled with different amounts of fluid that would have to be raised during the indentation which is confirmed in Figure 5.26.

5.4.Summary

To summarize, a method for the construction and testing of fluid-filled phantom is presented in this chapter. These phantoms are quite simple to make and can be seen to have non-linear viscoelastic trend, which is similar to that seen in the liver. The experimental tests were performed several times and there was no significant difference between each trial. The effects of density and viscosity, volume and boundary conditions were studied. The work showed that density and the volume of fluid in the phantom has a proportional effect on the force-displacement output during unconfined testing contrary to viscosity, which showed no significant effect. In confined testing, the effects of density and volume of fluid is minimized and viscosity still did not show any contribution. It is concluded that in confined testing the force-displacement output can be controlled using density of the fluid and the volume in the phantom in comparison to when confined conditions are applied.

Chapter 6 : Perfused Liver Phantom

The liver is known to have biphasic structure due to its solid and liquid phase. Kerdok et al. [37] showed that experiments performed on a perfused *ex-vivo* liver yielded significantly more realistic results than a non-perfused *ex-vivo* liver and also the perfusion allowed to approximate very closely the *in-vivo* case. This chapter aims to replicate the phenomenon showed by Kerdok et al. in a phantom. The phantom will be perfused simulating the hepatic macrocirculation. Different flow properties and pressures will be applied to characterize and validate this phantom for circulation as well as biomechanical testing.

6.1.Material and Method

A *Dimension 1200es* 3D printer was used to engrave the pattern shown in Figure 6.1, which is a rough representation of the liver macrocirculation [16] shown in Figure 6.2. It shows the two blood flow intakes, namely, through the portal vein and the hepatic artery, and the outflow through the hepatic vein. This pattern, printed in plastic, was then used to make a similar one from wax, by making a silicone mold and then pouring hot wax in it. The most widely used silicones in soft tissue phantoms are the RTV 6166 [9] and the ECOFLEX 00-30 [34]. The wax structure was then placed in a mold in which the silicone (*Smooth-On*, ECOFLEX 00-30) was poured and cured. The wax was then flushed out with hot water leaving a model of the vascular network as shown in Figure 6.3.

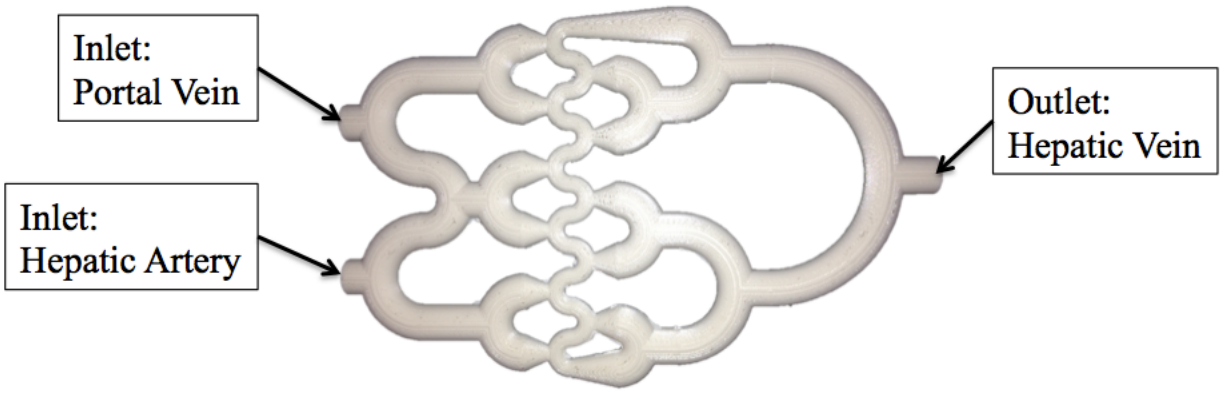

Figure 6.1: Pattern representing liver macrocirculation.

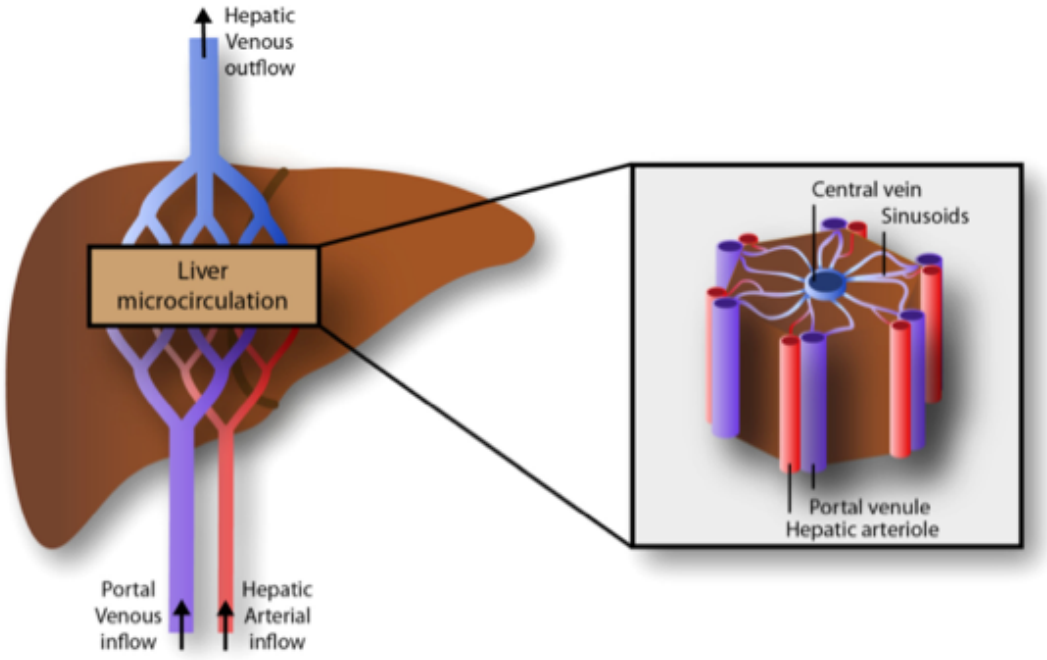

Figure 6.2: Hepatic circulation diagram taken from [16]

The phantom is perfused with a closed loop flow system explained in Chapter 4, which tends to reproduce the general features of the human hepatic macrocirculation. Each of

the inlets is pressurized to the average pressure observed in the human liver. This is done by having two containers at different heights respective to pressure filled with fluid. The fluid is collected and pumped back to the containers after having passed through the phantom. A 12-Volt DC centrifugal pump with a flow rate up to 2 liters/minute is driven by a mini DC motor *SGMADA RF 370C 12560*. A *Roboteq SDC2150* controller operates the motor to simulate the blood circulation.

The Reynolds number is estimated in both the largest and smallest vessels in the model. The largest diameter is at the inlet and has a value of 12mm while the smallest one is only 6mm and located in the middle section with corresponding Reynolds numbers of 3800 and 7600, respectively. This calculation is based on the maximum flow rate of 2 liters/minute and the kinematic viscosity of water at room temperature (21^{o}C). The Reynolds number can be controlled when changing the flow rate and the temperature. For example, the Reynolds numbers would be 2710 and 5420 in the largest and smallest vessel, respectively, when using a flow rate of 1.5 liter/minute and room temperature. The portal vein's Reynolds number found in literature [57] is between 1200 and 2600, and those values can be obtained with further variation of the flow rate.

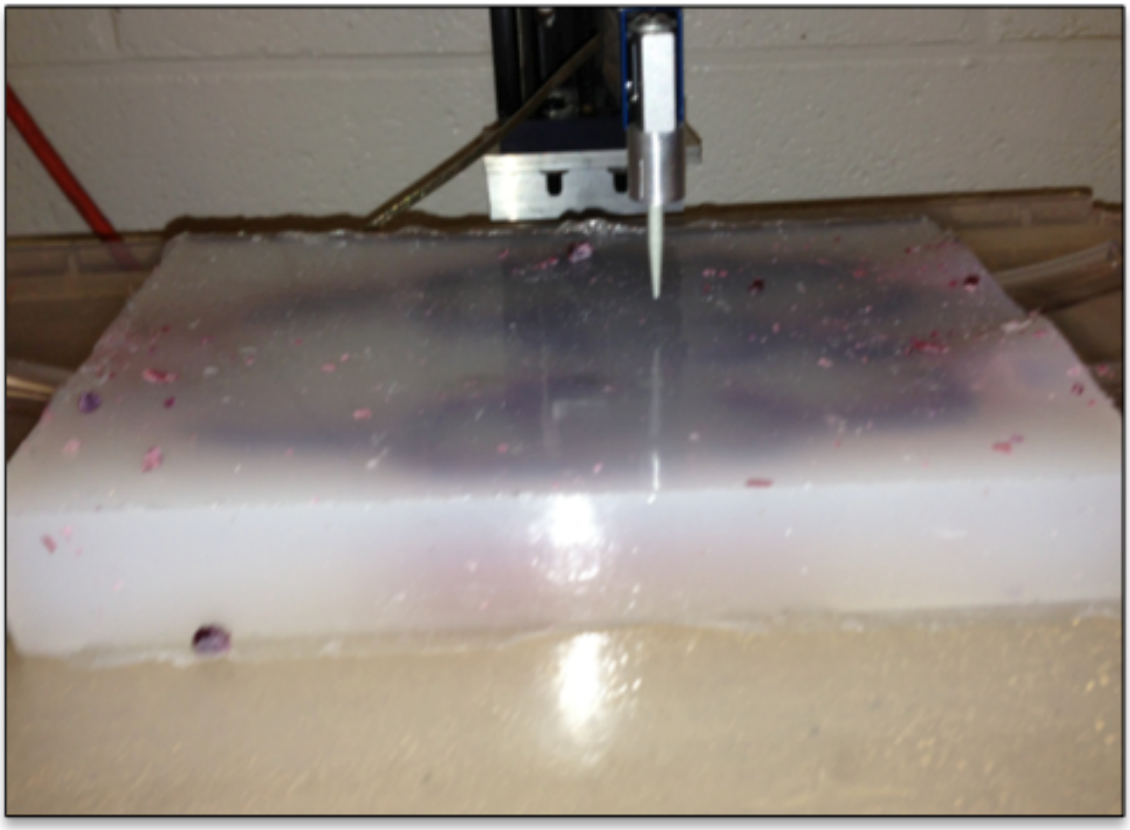

Figure 6.3: Perfused Liver phantom

6.2.Experimental Method

The phantom constructed will undergo testing to understand the effect of perfusion and pressure on the force-displacement output when subjected to quasi-static loading. The experimental apparatus and perfusion system explained in Chapter 4 will be used for these experiments.

6.2.1 Effects of Perfusion

To test the effects of perfusion the phantoms are subjected to quasi-static indentations of a depth of 5mm. The quasi-static loading is done at rates of 0.2 mm/s, 1 mm/s and 2

mm/s. To study the effects of perfusion, the perfused and non-perfused case will be compared.

6.2.2 Effects of Pressure

The study of the effects of pressure is done by monitoring the force-displacement output of the phantom under quasi-static indentation for the pressurized and non-pressurized conditions. Another test that will be performed will consist of monitoring the force feedback after indenting the phantom to a depth of 5mm. The pressure tank at the lower height will then be raised manually to the same height as the higher one (Figure 4.2), which will make the pressure in both inlets 97 mmHg. During these tests the phantom will not be perfused.

6.3.Results

6.3.1 Effects of Perfusion

The quasi-static indentation of the middle section of the phantom was performed. The results are presented for the perfused case in Figure 6.4 for different loading rates. Figure 6.6 compares quasi-static indentation of the phantom under perfused and unperfused conditions at a rate of 0.2 mm/s. The loading and unloading differences of the perfused liver phantom also at a rate of 0.2 mm/s can be seen in Figure 6.7.

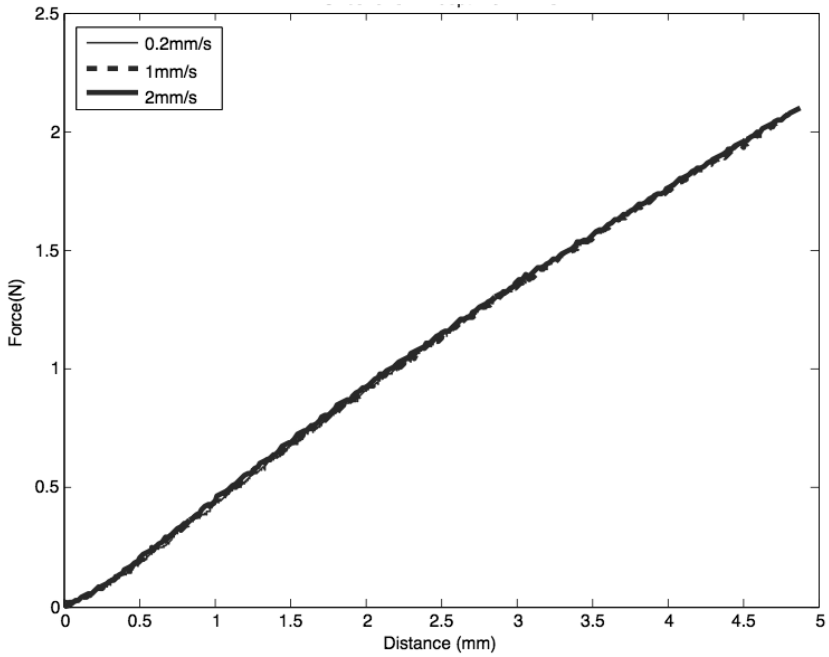

Figure 6.4: Quasi-Static Indentation (Loading) of Perfused Pressurized Liver Phantom

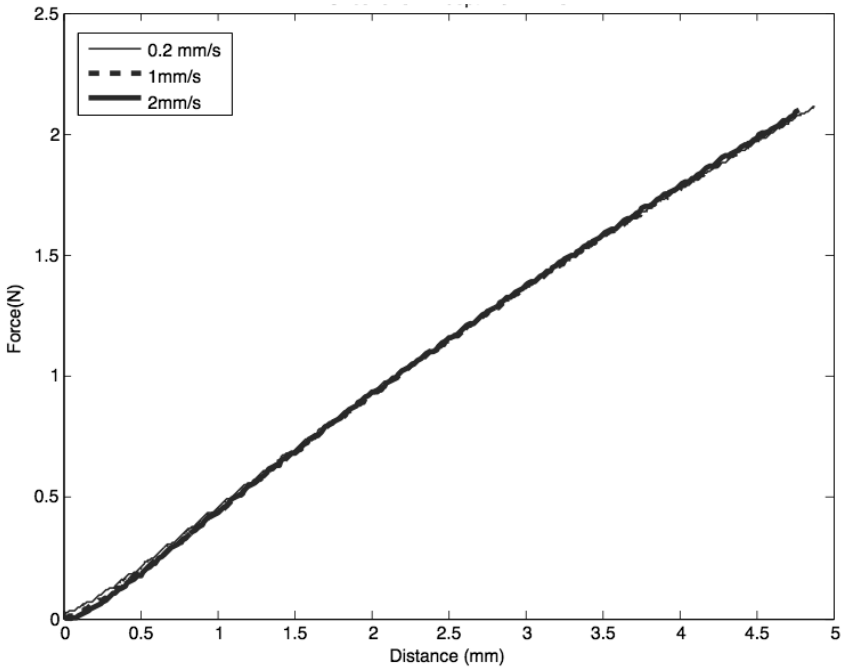

Figure 6.5: Quasi-Static Indentation (Loading) of Unperfused Pressurized Liver Phantom

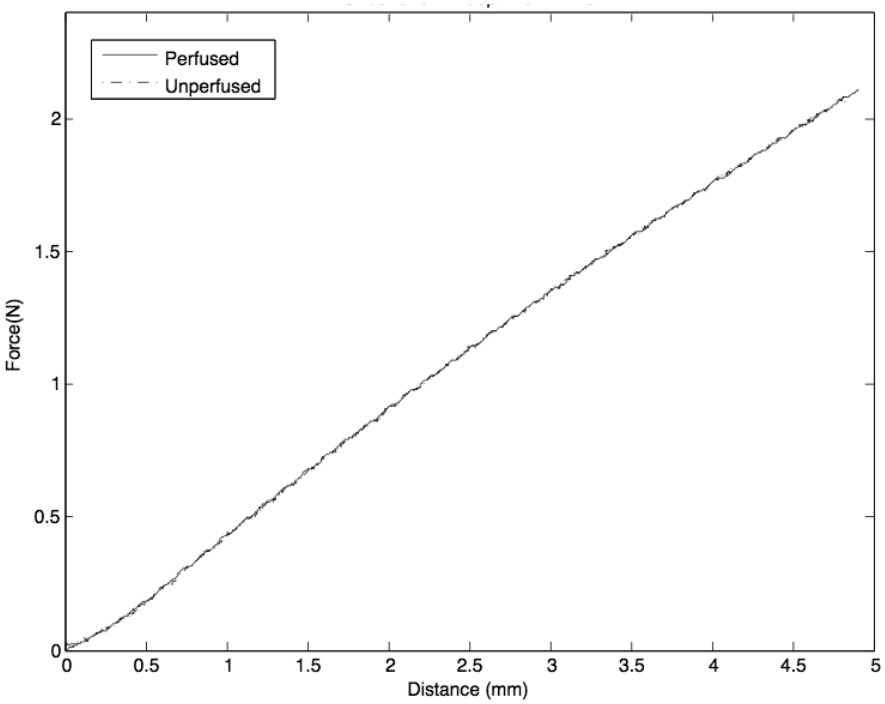

Figure 6.6: Comparison between Quasi-Static Indentation (Loading) at 2mm/s in Perfused and Non-Perfused Conditions.

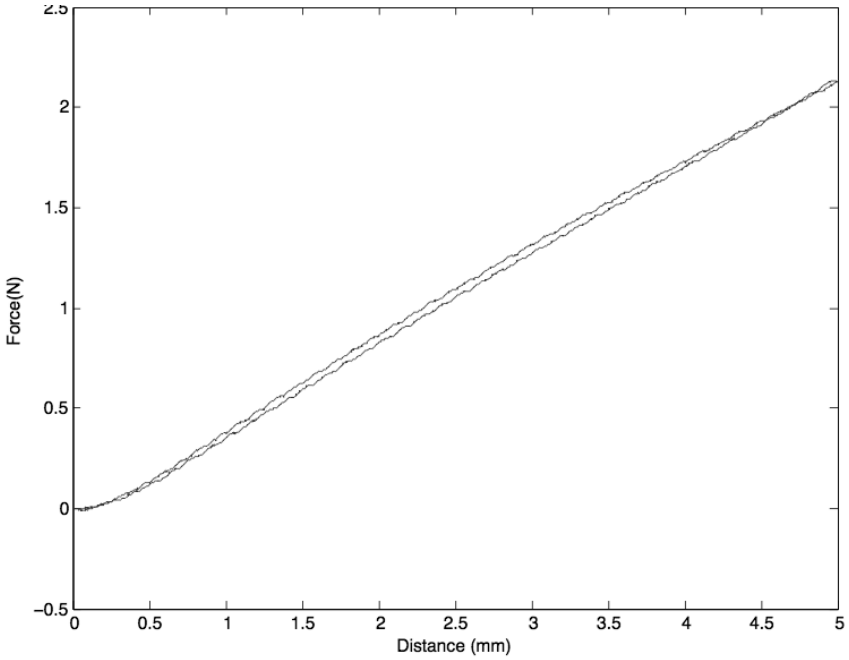

Figure 6.7: Quasi-Static Perfused Indentation (Loading and Unloading) of Liver Phantom at a rate of 0.2mm/s

6.3.2 Effects of Pressure

The force-displacement result for the quasi-static indentation of the phantom under pressurized conditions is shown in Figure 6.5 while Figure 6.8 presents the unpressurized condition.

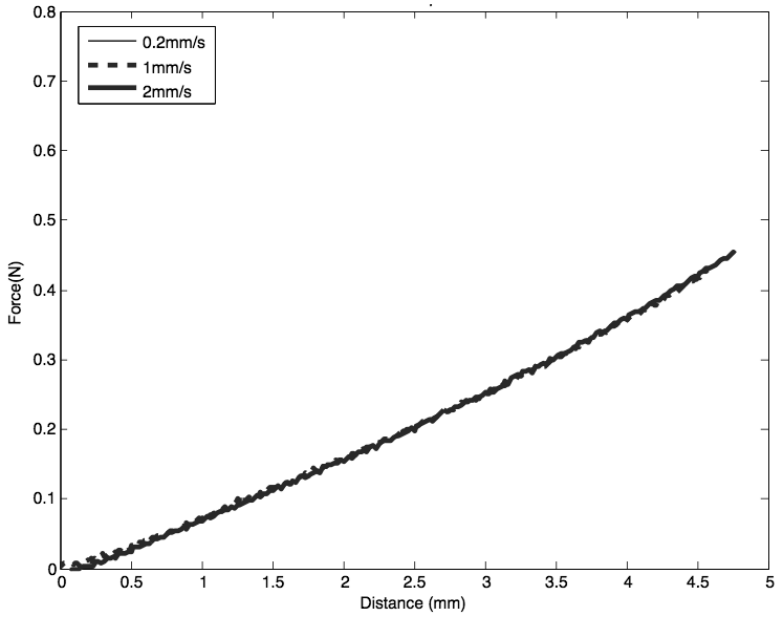

Figure 6.8: Quasi-Static Indentation (Loading) of Unperfused Liver Phantom with No-Pressure

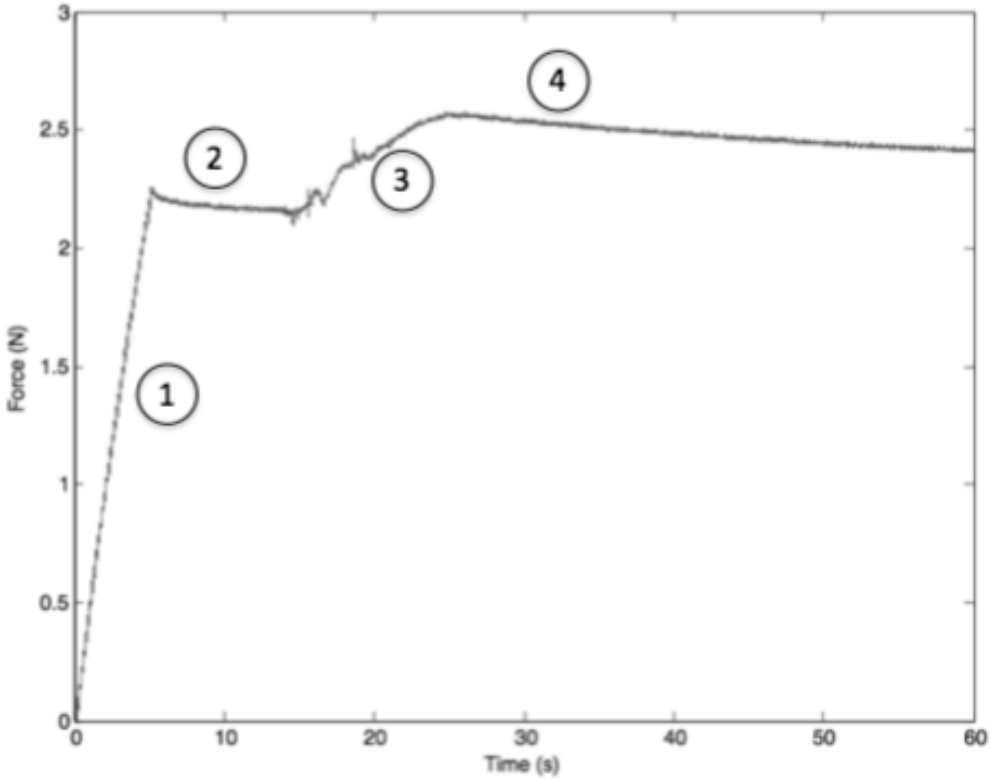

Figure 6.9: Pressure Variation After Loading Perfused Liver Phantom at a Rate of 1mm/s

The effects of pressure can be seen in Figure 6.9 where each number corresponds to a different phase in the loading and pressure variation to outline the effect of pressure. Loading the phantom at a rate of 1 mm/s to a depth of 5 mm is done in phase (1). During phase (2), the phantom is able to relax and creep can be observed. Pressure is initially set as outlined in the perfusion system shown in Figure 4.2. In phase (3), the tank with pressure of 8 mmHg is raised to the same height as the one with 97 mmHg. Finally, in phase (4) the phantom is allowed to relax with both tanks at that same pressure.

6.4.Discussion

The phantom was subjected to different experiments to characterize the effects of perfusion and pressure. Perfusion from Figure 6.6 does not show a quantifiable effect on the output of the phantom. The effect of pressure is made clear from Figure 6.9 where it is inferred that pressure has an effect on the force required to deform the phantom. It can be concluded that pressure was main contributor to the change in force-displacement output in the phantom. The work done by Kerdok et al. [37] showed that the use of their perfusion system had an effect on the properties of the liver. In organ likes the brain, experiments were conducted between *in-vivo* and *ex-vivo* testing and no significant difference was found [58]. Kerdok et al. [37] suggest that it can be due to the volume fraction of fluid in relation to the total volume. Similar conclusions can be drawn and explained due to the livers biphasic nature composed of solid and liquid phase. The phantom only covered the macrovessels of the liver since it was not possible to manufacture the microvessels meaning the volume fraction of fluid in the phantom compared to the liver is very small.

No significant difference between loading rates is observed in Figure 6.4. It was also seen that there is a slight hysteresis in the loading and unloading condition of the phantom (Figure 6.7). This could be due to the experimental set-up and slight deflection while loading the phantom, which is made relatively stiff due to the material properties of the ECOFLEX 00-30. The rate of loading and unloading during the quasi-static indentation does not show any noticeable difference.

6.5.Summary

In this chapter, a silicone-based flow phantom where fluid can flow through was created. The phantom is attached to the perfusion system outlined in Chapter 4 and subjected to quasi-static loading conditions. The experimental tests were reproduced several times and proved to be highly repeatable. It is seen in this phantom that perfusion did not have a quantifiable effect on the force required to deform the phantom. This is likely due to volume fraction of fluid because the microvessels of the liver are not modeled in this phantom. Varying the inlet pressure in the perfusion system is the main influence to this specific phantom.

Chapter 7 : Hydrogel-Based Liver Phantom

In this Chapter, a novel phantom with applications to the liver and other internal organs is developed and tested. The effect of the Glisson's Capsule will be considered by implementing an outer layer to the phantom. Literature shows that most phantoms currently existing or those have been developed for equipment calibration is mono-phasic with either single or multi-layers.

While the phantom presented in Chapter 6 captures the general features of hepatic macrocirculation, it does not incorporate the microcirculation [39] suggested using the bi-phasic poroviscoelastic model to the liver based it on porosity associated closely with its microcirculation. This further motivates the need for a phantom to account for the biphasic nature of the human liver.

This phantom will hopefully provide further realism to the currently existing phantoms. To that end, focus will be put on designing and testing a liver phantom to mimic its mechanical behavior.

7.1.Material and Methods

Hydrogel phantoms are composed of two phases consisting of linear low-density polyethylene (LLDPE) and hydrogel. The hydrogel is a gelatin (Knox) and three different water-to-gelatin ratios are employed. The manufacturing method is adapted from Kalyanam et al. [48]. The ratios of 4%, 6% and 8% gelatin to the 96%, 94% and 92% of water are measured by weight, respectively. The gelatin is hydrated and then refrigerated

at 4^{o}C in order to bloom. After 2 hours, the mixture is removed, stirred and put in a hot water bath. This procedure is done to minimize air bubbles from entering the hydrogel. The temperature was controlled to ensure it would not exceed 60^{o}C. The final step in creating the phantom is to pour the mixture in a linear low-density polyethylene bag. The phantom is left to set for 24 hours before testing.

The dimensions of the phantom are not well defined since the LLDPE bag is composed of two squares pieces attached together. The height and width of the phantom depend on the volume of hydrogel being inserted as well as the size of the LLDPE bag. Each phantom is filled with 500 ml of hydrogel in liquid form, which will yield a phantom height of 0.027 m, and the width of the square sheet is 0.0145 m.

The phantoms with the three different water concentrations are also subjected to relaxation testing. The phantom is loaded at a rate of 2 mm/s to a depth of 4.5 mm. The relaxation of the phantom is monitored by the testing system described in Chapter 4, for duration of 200 seconds. The relaxation testing is also applied to hydrogel only without the LLDPE layer.

Quasi-static testing is performed on the phantoms with the three different gelatin concentrations. Loading and unloading of the phantoms is done at the same rate. The rates of indentation used are 0.2 mm/s, 1 mm/s and 2 mm/s. The phantoms are loaded to indentation depths of 4.5 mm.

7.2.Finite Element Analysis and Modeling

The material properties of the hydrogel as well as the phantom need to be determined. A parametric study employing FEA was conducted to determine these properties. The FEA modeling is done in ABAQUS where the model will have the same boundary conditions as the experimental test.

The geometry of the phantom is not well defined since the hydrogel is in liquid form while poured into the LLDPE bag. However, the size of the bags was chosen large enough compared with the size of the indenter and the total deflection in order to approach infinite plane approximation. This assumption will be checked in the finite element model. In addition two different model geometries, cylindrical and rectangular were analyzed using the finite element method (Figure 7.1). The height and width of the phantom is 0.027 m and 0.145 m, respectively. The same material properties are applied to both models and the average will be used to determine the elastic modulus of the hydrogels.

The model is created in ABAQUS with an outer layer simulating the LLDPE as the Glisson's capsule substitute and an inner layer representing the hydrogel. The hydrogel inner layer is modeled using BPVE model including viscoelasticity, pore pressure, permeability and elastic components for the material properties. The LLDPE outer layer is modeled as a thin film surrounding the hydrogel.

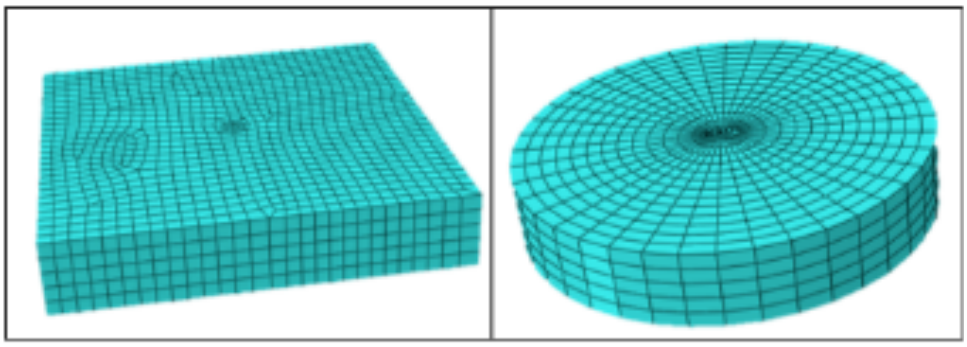

Figure 7.1: FEA models with different geometries: Rectangular (left) and Cylindrical (right)

7.3.Model Fitting

The biphasic poroviscoelastic model for the hydrogel consisted of three different components that needed to be input into ABAQUS: rate independent elastic response, rate dependent response and permeability. The rate independent elastic response is obtained from a parametric study yielding Poisson's ratio as well as the elastic modulus. The rate dependent response is obtained from fitting the relaxation data by minimizing a sum of squares difference to Equation 24 using a three-term Prony series to discretize the relaxation spectrum. The permeability coefficients and the void ratio are taken from literature [48].

7.4.Infinite Plane Assumption

The problem of geometry had been raised which brought forth the idea of the infinite plane assumption. It is assumed that the size of the indenter is very small in comparison to the size of the entire phantom. This means that the width and length would not have a major effect on the force-displacement output of the phantom. In addition, it is assumed that the curvature of the surface is small enough to assume it is a plane.

In order test this hypothesis further FEA testing is done. In this test, phantoms of rectangular geometries are subjected to quasi-static indentation (loading) and the force-displacement data is observed. These tests are performed in the FEA simulation using an indentation rate of 1 mm/s and the mechanical properties associated with the 92% water concentration phantom while all other variables and material properties are kept constant. Six different tests are compared and the third model is the same as presented above with a width and length of 14.5 mm. The first, second, fourth and fifth models have a width and length of 60 mm. 30 mm, 7 mm and 5 mm respectively.

7.5.Results

7.5.1 Relaxation Testing

The parameters used for the viscoelastic components of the hydrogel phase only are obtained by fitting the relaxation spectrum. The parameters obtained for the hydrogel water content are $g_1 = 0.0722$, $g_2 = 0.0784$, $g_3 = 0.313$, $\tau_1 = 5.2044$s, $\tau_2 = 104.4793$s and $\tau_3 = 6083.8$s. The density of the material is assumed to be similar to that of water while Poisson's ratio is 0.47. The permeability constants used are $k = 3.0 \times 10^{-11}$ m^4/Ns and the void ratio is $e_0 = 0.9$.

Table 7-1: Viscoelastic properties of different phantoms

	Relaxation Parameters					
Water Content	g_1	g_2	g_3	τ_1	τ_2	τ_3
92%	0.0659	0.1840	0.2113	0.0072	21.1128	256.1546
94%	0.0548	0.0531	0.0844	4.8330	40.7010	390.0156
96%	0.0455	0.0469	0.1491	4.579	55.6667	5450.007

The phantoms were also fitted using Equation 24, and Table 7-1 to outline the relaxation data. Figure 7.2 presents the data obtained from replicating the relaxation testing experiment in the FEA simulation and compares it to the experimentally obtained results.

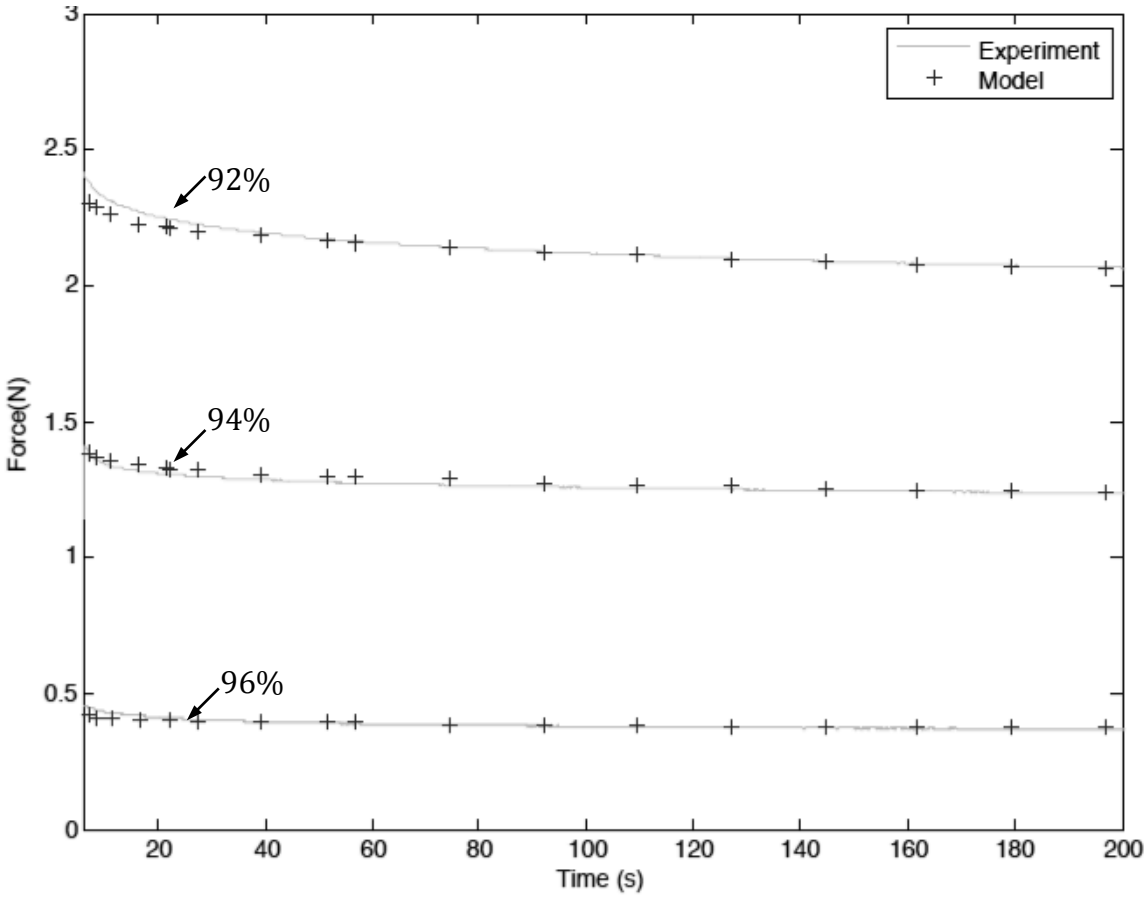

Figure 7.2: Phantom relaxation data fitted using FEA

7.5.2 Quasi-Static Indentation Testing

The Young's modulus of each phantom is obtained using the parametric study and shown in Table 7-2 by fitting the data obtained from quasi-static indentation shown in Figure 7.3. To account for the inability to model the shape of the phantom, two different geometries were studied and it was found that they had slightly different Young's modulus. The viscoelastic components are the same for both geometries. The average Young's modulus between the two models is also calculated and presented (Table 7-2).

Table 7-2: Comparison of the Young's modulus obtained in different FEA model geometries

Water Content (%)	E (Pa) Cylindrical Geometry	E (Pa) Rectangular Geometry	E (Pa) Average
92	5000	4950	4975
94	1820	1640	1730
96	270	240	255

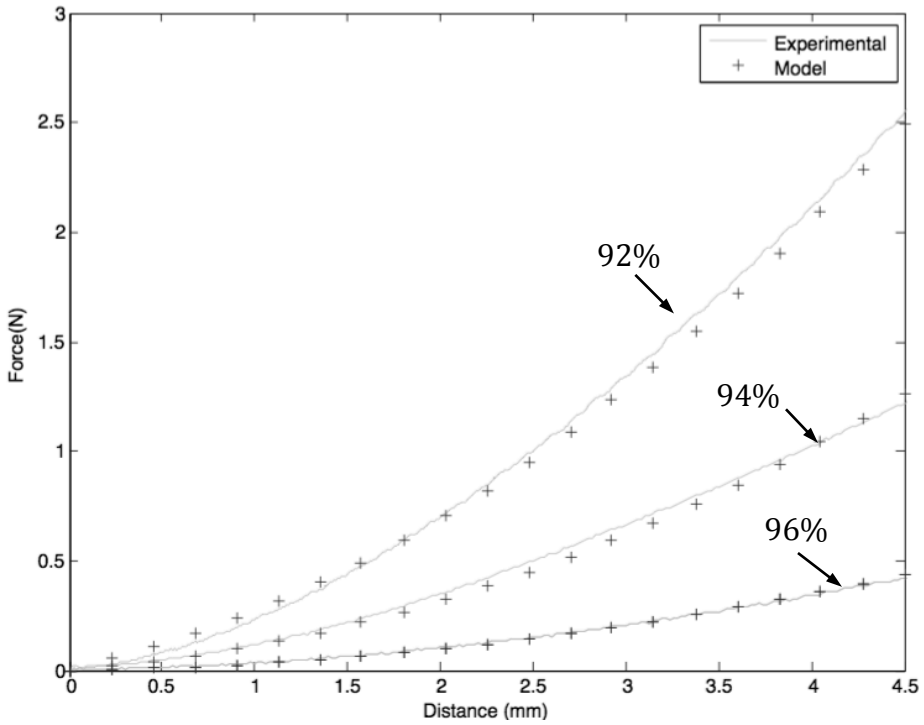

Figure 7.3: Quasi-Static Indentation of the Phantom fitted using FEA

7.5.3 Infinite Plane Assumption Testing

The simulations are performed for five different models to validate the infinite plane assumption for the geometry of the model, and the results are presented in Figure 7.4.

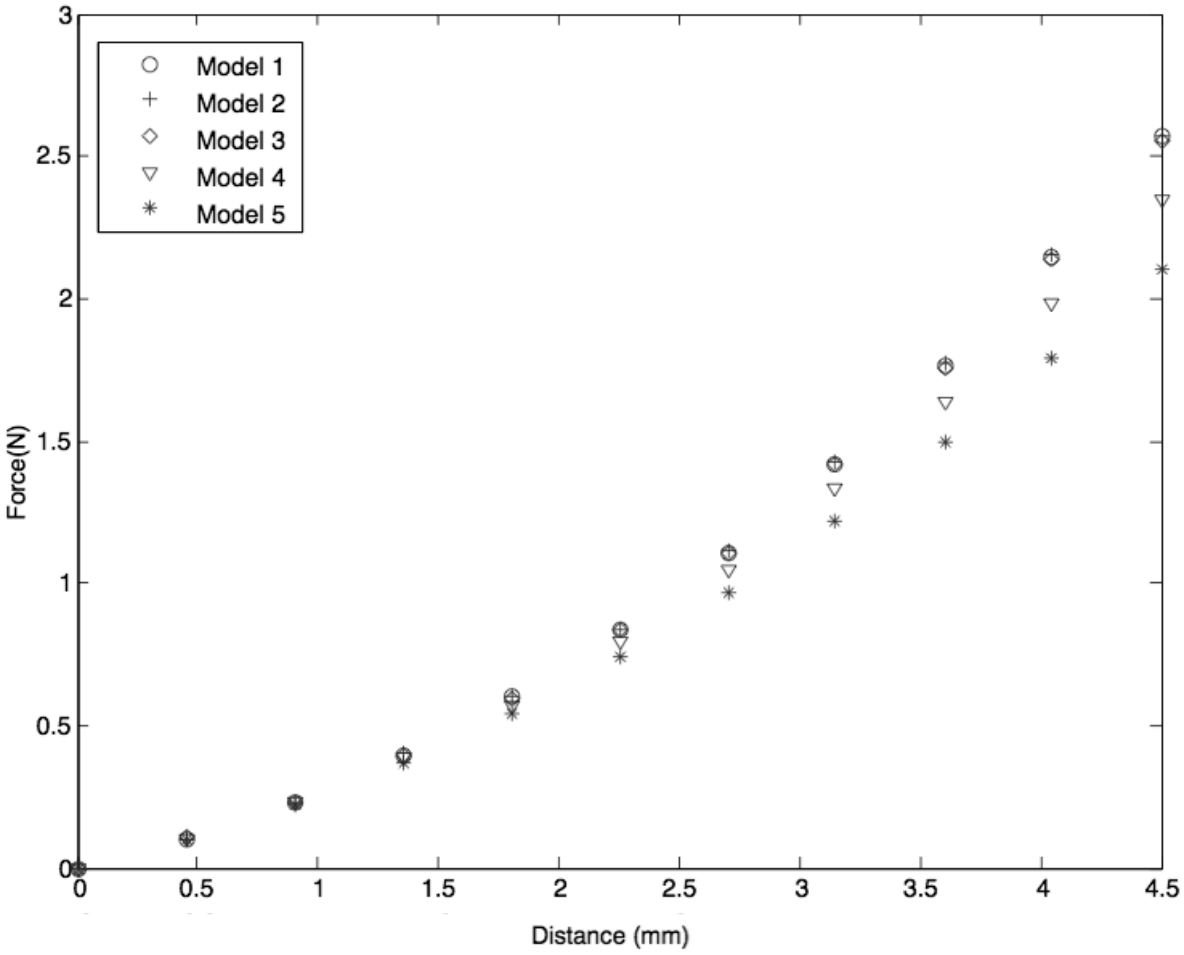

Figure 7.4: FEA simulation on three rectangular models. The length and width are identical but vary depending on the model: Model 1=600mm, Model 2=300mm, Model 3= 145mm, Model 4=70mm and Model 5=50mm.

7.6.Discussion

7.6.1 Relaxation Testing

The model assumed frictionless boundary condition for the bottom of the phantom, which seems to be reasonable because of the experimental boundary conditions. The relaxation data presented in Figure 7.2 is similar to the trends found in literature [48] for the hydrogel. Comparing the relaxation data to the literature for the porcine liver [39] and human liver [3] revealed values in the same range. It can also be seen in Figure 7.2 that the rate of relaxation can be adjusted with the variation of water content of the hydrogel making up the phantom.

The LLDPE bag surrounding the hydrogel seems to have a contribution in the viscoelastic properties. The data obtained from the phantom and the hydrogel both having water concentration of 92% (Figure 7.5) shows that the LLDPE layer will increase the force required in order to deform the phantom. It can also be seen that the LLDPE layer on the phantom affects the rate of relaxation.

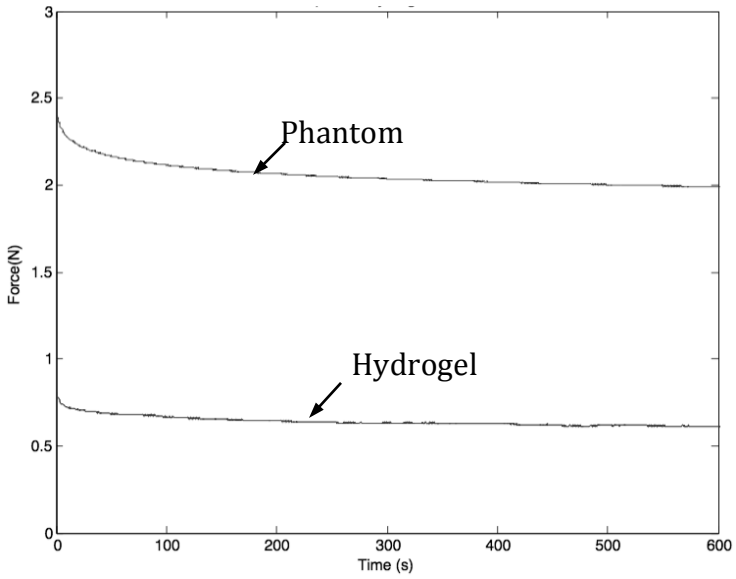

Figure 7.5: Relaxation data comparison between hydrogels having 92% water content with and without LLDPE

7.6.2 Quasi-Static Indentation Testing

Quasi-Static indentation testing of the phantom in Figure 7.3 shows that the force-displacement output has an inversely proportional relationship. This can be seen by comparing the phantom with water content of 92%, which is the highest, to the lowest being the phantom with 96% water content. A similar trend to the one exhibited is in literature [36] [49] for hydrogels.

The force-displacement output is dependent on the speed of indentation, which is observed experimentally and in the ABAQUS simulation, and is presented in Figure 7.6. The liver is also rate dependent when subjected to quasi-static loading [6]. However, it is quite difficult to accurately fit the experimental data's rate dependence, which could be due to the permeability. The rate dependent permeability for the liver is not included in

the model used by Schwartz et al. [39] but they also noted that it could provide better results to the model.

The two different geometry of models yielded virtual identical fit to quasi-static indentation as well as relaxation. This can yield the acceptance of the results even though the model geometry is not the same as the one seen in the phantom. This can be due to the size of the indenter being relatively small in comparison to phantom.

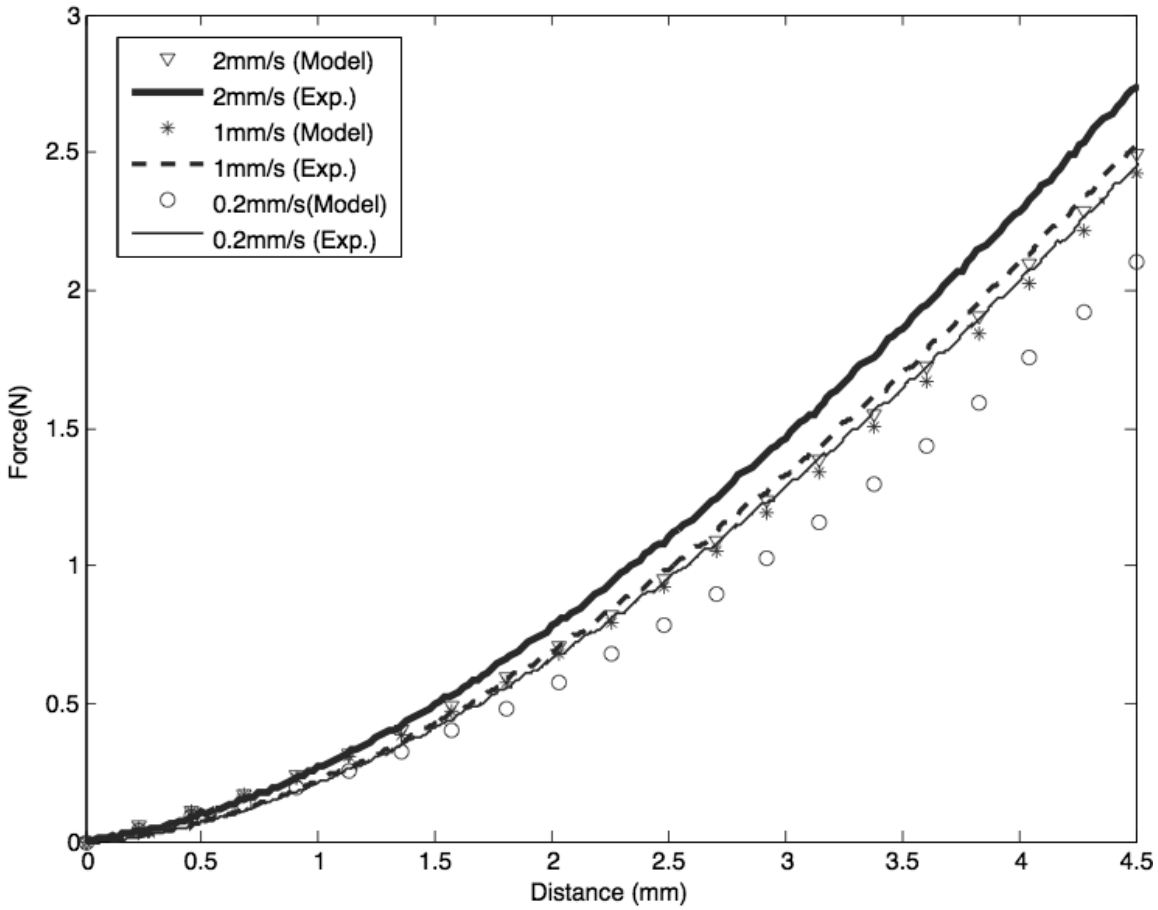

Figure 7.6: Quasi-static indentation of hydrogel phantoms with 92% water content at rates of 0.2,1 and 2mm/s fitted using FEA

7.6.3 Infinite Plane Assumption

From the results presented in Figure 7.4 it can be inferred that as the width and length of the model is increased the force-displacement output will converge to reach a maximum. The model used in the simulation is within that maximum. Therefore, the infinite plane assumption for the model can be accepted.

7.7.Summary

In this chapter we presented a hydrogel-based liver phantom that simulated the Glisson's capsule as a LLDPE layer and hydrogel for the bulk of the liver tissue. There was good agreement between the finite element model and the experimental data. While some error may have been introduced due to the permeability and Poisons ratio taken from literature as well as the LLDPE-fitting error, the properties of the phantoms are described.

The LLDPE layer as well as the water content in the hydrogel were found to affect the phantom's relaxation rate. In terms of quasi-static indentation, the water content in each of the hydrogel had the largest role in determining the force-displacement relationship.

The infinite plane assumption for the geometry is valid for the size of the phantom used. This work can be extended to act as phantoms for the liver and other organs in many different applications.

Chapter 8 : Conclusions and Future Work

In this work, an experimental setup was developed and built to conduct quasi-static and relaxation testing on different internal organ phantoms. Three different phantoms were developed, built and tested. Conclusions from testing each one the phantoms and future potential work are summarized below.

8.1.Fluid-Filled Phantom

A fluid-filled phantom was developed and characterized using quasi-static and relaxation testing. The relaxation spectrum was compared to literature and showed good agreement. The effects of the density and viscosity, volume and boundary conditions were studied. The work showed that density and the volume of fluid in the phantom had a proportional effect on the force-displacement output during unconfined testing contrary to viscosity, which showed no significant effect. In the confined testing conditions, the effects of density and volume of fluid is minimized and viscosity did not show any contribution. It was concluded that in confined testing the force-displacement output can be controlled using density of the fluid, and the volume in the phantom in comparison to when confined conditions are applied. Applications from this phantom can be used as a low-cost liver phantom since it exhibits non-linear viscoelastic properties present in the liver.

Future work would include developing a FEA model that further characterizes the phantom.

8.2.Perfused Liver Phantom

A unique perfused liver phantom was manufactured and a perfusion system, which mimics the general features of the hepatic flow, was designed. It was observed that, during testing of this phantom, perfusion did not have a quantifiable effect on the force required to deform the phantom. This was attributed to the volume fraction of fluid in the phantom because the microvessels of the liver were not modeled. Varying the inlet pressure in the perfusion system was the main influence to this specific phantom.

Future work should focus on developing other perfused phantoms with better physiological accuracy and representation of the microcirculation. Further testing can be done to determine different properties of hepatic circulation such as the effect of pulsatile flow on Reynolds number. A CFD could further validate this phantom.

8.3.Hydrogel-Based Liver Phantom

Design, construction and validation of hydrogel-based phantom were successfully accomplished. The phantoms were modeled in ABAQUS where it was possible to obtain insight on the material properties. The BPVE model was then validated for the hydrogel part of the phantom. The Neo-Hookean hyperelastic model was found to be a good fit for the LLDPE layer. This work can be extrapolated to not only the liver but also different organs since this phantom accounted for the biphasic nature.

In the future, experiments can be conducted using different LLDPE layer thickness and related to more accurate modeling of the Glisson's capsule including obtaining a rate-dependent model to fit the rate-varying data.

References

[1] McDougall, E. M., Corica, F. A., Boker, J. R., Sala, L. G., Stoliar, G., Borin, J. F., et al. (2006). Construct validity testing of a laporoscopic surgical simulator. *Journal of the American colele of surgeons 202.5* , 779-787.

[2] Hamad, G. G., & Curet, M. (2010). Minimally invasive surgery. *The american journal of surgery , 199* (2), 263-265.

[3] Nava, A., Mazza, E., Furrer, M., Villiger, P., & Reinhart, W. H. (2008). In vivo mechanical characterization of human liver. *Medical Image Analysis* (12), 203-216.

[4] Nakamura, K., Kikuya, M., Hara, A., Hirose, T., Obrara, T., Metoki, H., et al. (2010). Validation of the FM-800 ambulatory blood pressure monitor according to the association for advancement of medical instrumentation criteria and international protocol. *Clinical and experimental hypertension , 32* (8), 523-527.

[5] Ahn, B., & Kim, J. (2010). Measurement and characterization of soft tissue behavior with surface deformation and force response under large deformations. *Medical Image Analysis* , 138-148.

[6] Kerdok, A. E. (2006). *Characterizing the nonlinear mechanical response of liver to surgical simulation.* Diss., Harvard University, Cambridge, MA.

[7] Culjat, M. O., Goldenberg, D., Tewari, P., & Singh, R. S. (2010). A review of tissue substitutes for ultrasound imaging. *Ultrasound in medicine and biology , 6*, 861-873.

[8] Siegel, M. J., Schmidt, B., Bradley, D., Suess, C., & Hildebolt, C. (2004). Radiation dose and image quality in pediatric CT: Effect of technical factors and phantom size and shape1. *Radiology , 2*, 514-522.

.

[9] Kalanovic, D., Ottensmeyer, M. P., Gross, J., Buess, G., & Dawson, S. L. (2003, January). Independent testing of soft tissue visco-elasticity using indentation and rotary shear deformation. *Medicine meets virtual reality* , 137-143.

[10] Lautt, W. W. (2009). Chapter 2: Overview. In *Hepatic Circulation: Physiology and Pathology* (pp. 1-12). Morgan & Claypool Life Sciences.

[11] Bonfiglio, A., Leungchavaphongse, K., Repetto, R., & Siggers, J. H. (2010). Mathematical modeling of the circulation in the liver lobule. *Journal of biomechanical engineering , 132*, 1-10.

[12] Kratzer, W., Fritz, V., Mason, R. A., Haenle, M. M., Kaechele, V., & the Roemerstein Study Group. (2009). Factors affecting liver size a sonographic survery of 2080 subjects. *Journal of ultrasound in medicine , 22* (11), 1155-1161.

[13] Carlisle, K. M., Halliwell, M., Read, A. E., & Wells , P. N. (1992). Estimation of total hepatic blood flow by duplex ultrasound. *Gut , 33*, 92-97.

[14] Teutsch, H. F., Schuerfeld, D., & Groezinger, E. (1999). Three-dimensional reconstruction of parenchymal units in the liver of the rat. *Hepatology , 29* (2), 494-505.

[15] Teutsch, H. F. (2005). The modular microarchitecture of human liver. *Hepatology , 42* (2), 317-325.

[16] Debbaut, C., Vierendeels, J., Casteleyn, C., Cornillie, P., Van Loo, D., Simoens, P., et al. (2012). Perfusion characterisitics of the human hepatic microcirculation based on three-dimensional reconstructions and computational fluid dynamic analysis. *Journal of Biomechanics , 134*, 1-10.

[17] Ijaz, S., Yang, W., Winslet, M. C., & Seifalian, A. M. (2003). Impairment of hepatic microciculation in fatty liver. *Microcirculation , 10*, 447-456.

[18] (2013) Blue Phantom. [Online]. HYPERLINK "www.bluephantom.com" www.bluephantom.com

[19] Simulab. (2013) Simulab Corporation. [Online]. HYPERLINK "www.simulab.com" www.simulab.com

[20] Schout, B. M., Hendrikx, A. J., Scheele, F., Bemelmans, B. L., & Scherpbier, A. J. (2010). Validation and implementation of surgical simulators: a critical review of present, past and future. *Surgical Endoscopy , 24* (3), 536-546.

[21] Haluck, R. S., Marshall, R. L., Krummel, T. M., & Melkonian, M. G. (2001). Are surgery training programs ready for virtual reality? A survey of program directors in general surgery. *Journal of the american college of surgeons , 193* (6), 660-665.

[22] Cooper, J. B., & Taqueti, V. R. (2008). A brief history of the development of mannequin simulators for clinical education and training. *Postgraduate medical journal* , 563-570.

[23] Hammoud, M. M., Nuthalapaty, F. S., Goepfert, A. R., Casey, P. M., Emmons, S., Espey, E. L., et al. (2008). To the point: medical education review of the role of

simulators in surgical training. *American journal of obstetrics and gynecology , 199* (4).

[24] Satava, R. M. (1993). Virtual reality surgical simulator. *Surgical endoscopy , 7*, 203-205.

[25] Delingette, H. (1998). Towards realistic soft tissue modeling in medical simulation. *IEEE: Special issue on virtual and augmented reality in medicine , 86*.

[26] DeCarlo, D., Kaye, J., Metaxas, D., Clarke, J. R., Webber, B., & Badler, N. (1995). Integrating anatomy and physiology for behavior modeling. In R. M. Satava, K. Morgan, & H. B. Sieburg, *Interative technology and the new paradigm for health care.* Ios PressInc.

[27] Szekely, G., Brechbuhler, C., Dual, J., Enzler, R., Hug, J., Hutter, R., et al. (2000). Virtual reality-based simulation of endoscopic surgery. *Presence: Teleoperators & virtual environments , 9* (3), 310-333.

[28] J K Suh, F H Fu, and Inchan Youn, "Arthroscopic diagnostic prove to measure mechanical properties of articular cartilage," 6585666, july 1, 2003.

[29] Nava, A., Mazza, E., Kleinermann, F., Avis, N. J., & McClure, J. (2003). Determination of the mechanical properties of soft human tissues through aspiration experiments. *Medical image computing and computer-assisted*

[30] U Kuhnapfel, U., Cakmak, H. K., & MaaB, H. (2000). Endoscopic surgery training using virtual reality and deformable tissue simulation. *Computers & Graphics* , pp. 671-682.

[31] Szekely, G., Brechbuhler, C., Hutter, R., Rohmberg, A., & Schmid, P. (2000, March). Modelling of Soft Tissue Deformation for Laparoscopic Surgery Simulation. *Medical Image Analysis , 4* (1), pp. 57-66.

[32] Han, L., Noble, J., & Burcher, M. (2003). A novel ultrasound indentation system for measuring biomechanical properties of in vivo soft tissue. *Ultrasound in Med. & Biol. , 29* (6), 2003.

[33] Liu, H., Noonan, D. P., Althoefer, K., & Seneviratne, L. D. (2008). Rolling mechanical imaging: a novel approach for soft tissue modelling and indentification during minimally invasive surgery. *International conference on robotics and automation* (pp. 845-850). Pasadena, CA, USA: IEEE.

[34] Boonvisut, P., Jackson, R., & Cavusogly, M. C. (2012). Estimation of soft tissue mechanical parameters from robotic manipulation data. *International conference on robotics and automation* (pp. 4667-4674). Saint-Paul: IEEE.

[35] Zhang, T., Yan, Y., Wang, X., Xiong, Z., Lin, F., Wu, R., et al. (2007). Three-dimensional gelatin and gelatin/hyaluronan hydrogel structures for traumatic brain injuries. *Journal of bioactive and compatible polymers , 22* (19), 19-29.

[36] Kwon, J., & Subhash, G. (2012). Compressive strain rate sensitivity of ballistic gelatin. *Journal of biomechanics , 43* (3), 420-425.

[37] Kerdok, A. E., Ottensmeyer, M. P., & Howe, R. D. (2006). Effects of perfusion on the viscoelastic characteristics of the liver. *Journal of Biomechanics , 39* (12), 2221-2231.

[38] Schwartz, J.-M., Denninger, M., Rancourt, D., Moisan, C., & Denis, L. (2005). Modelling liver tissue properties using a non-linear visco-elastic model for surgery simulation. *Medical Image Analysis , 9*, 103-112.

[39] Raghunathan, S., Evans, D. W., & Sparks, J. L. (2010). Poroviscoelastic modeling of liver biomechanical response in unconfined compression. *Annals of Biomedical*

Engineering , 38 (5), 2010.

[40] Umale, S., Chatelin, S., Bourdet, N., Deck, C., Diana, M., Dhumane, P., et al. (2011). Experimental in vitro mechanical characterization of porcine Glisson's capsule and hepatic veins. *Journal of Biomechanics , 44*, 1678-1683.

[41] Ramnarine, K. V., Anderson, T., & Hoskins, P. R. (2001, February). Construction and geometric stability of physiological flow rate wall-less stenosis phantoms. *Ultrasound in Medicine & Biology , 27* (2), pp. 245-250.

[42] Kumar V Ramnarine, Tom Anderson, and Peter R Hoskins, "Construction and geometric stability of physiological flow rate wall-less stenosis phantoms," *Ultrasound in Medicine & Biology*, vol. 27, no. 2, pp. 245-250, February 2001.

[43] Gosline, A. H., Salcudean, S. E., & Yan, J. (2005). Haptic Simulation of Linear Elastic Media with Fluid Inclusions. *Haptics-E: Electronic Journal of Haptic Research , 3*, 1-11.

[44] De, S., & Srinivasan, M. A. (1999). Thin walled models for haptic and graphical rendering of soft tissues in surgical simulations. *Medine Meets Virtual Reality* , 94-99.

[45] Turgay, E., Salcudean, S., & Rohlig, R. (2006). Identifying the mechanical properties of tissue by ultrasound strain imaging. *Ultrasound in Med. & Biol. , 32* (2), 221-235.

[46] Jiang, S., Liu, S., & Feng, W. (2011). PVA Hydrogel properties for biomedical application. *Journal of the mechanical behavior of biomedical materials* , 1228-1233.

[47] Kerdok, A. E., Cotin, S. M., Ottensmeyer, M. P., Galea, A. M., Howe, R. D., & Dawson, S. L. (2003). Truth cube: establishing physical standards for soft tissue deformation. *Medical imagine analysis , 7*, 283-291.

[48] Kalyanam, S., Yapp, R. D., & Insana, M. F. (2009). Poro-viscoelastic behavior of gelatin hydrogel under compression-implications for bioelasticity imaging. *Journal of Biomechanical Engineering , 131* (8).

[49] Toohey, K., Kalyanam, S., & Insana, M. (2009). Cross-validation of experimental methodologies to characterize the behavior of hydrogels. *Society from Experimental Mechanics.* Albuquerque,New Mexico, USA.

[50] Lai, W. M., & Mow, V. C. (1980). Drag induced compression of articular cartilage during a permeation experiment. *Biorheology* , 111-123

[51] Armstrong, C. G., Lai, W. M., & Mow, V. C. (1984). An analysis of the unforined compression of articular cartilage. *Journal of Biomechanical Engineering , 106*, 165-173.

[52] Suh, J. K., & DiSilvestro, M. R. (1999). Biphasic poroviscoelastic behavior of hydrated biological soft tissue. *Journal of Applied Mechanics , 66*, 524-534.

[53] Hibbit, Karlsson & Sorenson. (2007). *Abaqus Manual.* Version (6.9).

[54] Suh, J. K., & Bai, S. (1998). Finite element formulation of biphasic poroviscoelastic model for articular cartilage. *Journal of Biomechanical Engineering , 120*, 195-201.

[55] Cheng, N.-S. (2008). Formula for viscosity of glycerol-water mixture. *Industrial and engineering chemistry research , 47*, 3285-3288.

[56] Durmus, A., Kasgoz, A., & Macosko, C. W. (2007). Linear low density polyethylene (LLDPE)/clay nano composites. Part I: Structural characterization and quantifying clay dispersion by melt rheology. *Polymer , 48* (15), 4492-4502.

[57] Huber, G. H., Steudel, N., Kleber, G., Behrmann, C., Lotterer, E., & Fleig, W. E. (2000). Hepatic arterial blood flow velocities: assessment by transcutaneous intravascular Doppler sonography. *Journal of Hepatology , 32*, 893-899.

[58] Gefen, A., & Margulies, S. S. (2004). Are in vivo and in situ brain tissues mechanically similar? *Journal of Biomechanics , 37* (9), 1339-1352.

[59] Fung, Y. (1993). *Biomechanics : mechanical properties of living tissues.* New York: Springer-Verlag